Dissertation

submitted to the

Combined Faculty of Natural Sciences and Mathematics

of the Ruperto Carola University of Heidelberg, Germany

For the degree of

Doctor of natural sciences

Presented by

M.Sc. Biotechnologist Matteo Guerra

Born in: San Giovanni Rotondo, Italy

Oral examination: 30th June, 2020

From the plasma membrane to tangled DNA webs:

a roadway to track, investigate and employ spatially localized neutrophil elastase and cathepsin G activities

Referees: Prof. Dr. Edward Lemke

Prof. Dr. Britta Brügger

Table of contents

Abbreviations

16HBE14o-	**human bronchial epithelial cell line**
ASL	**airway surface liquid**
A1AT	**alpha-1-antitrypsin**
BAL	**bronchoalveolar lavage**
BALF	**bronchoalveolar lavage fluid**
BV	**Brilliant violet**
βENaC-Tg	**βENaC-overexpressing**
CD	**cluster of differentiation**
CG	**cathepsin G**
CF	**cystic fibrosis**
CFTR	**cystic fibrosis transmembrane conductance regulator**
COPD	**chronic obstructive pulmonary disease**
Coum343	**Coumarin 343**
CXCL	**Chemokine ligand**
D/A	**donor/acceptor**
ECM	**extracellular matrix**
ENaC	**epithelial sodium channel**
FACS	**fluorescence activated cell sorting**
FEV1	**Forced Expiratory Volume in 1 second**
FITC	**Fluorescein isothiocyanate**
FMLP	**N-Formylmethionyl-leucyl-phenylalanine**
Fmoc	**fluorenylmethoxycarbonyl**
FRET	**Förster resonance energy transfer**
HeLa	**cell line derived from Henrietta Lacks**
HEK	**cell line derived from human embryonic kidney**
HL-60	**neutrophil-like cell line**
HPLC	**high-pressure liquid chromatography**
H&E	**hematoxylin and eosin**
IFN	**Interferon**

IL	**Interleukin**
kDa	**kilo Dalton**
LPS	**lipopolysaccharide**
LUT	**look up table**
MMP	**matrix-metalloproteinase**
Mtt	**4-Methyltrityl protecting group**
NADPH	**reduced form of nicotinamide adenine dinucleotide phosphate**
NE	**neutrophil elastase**
NE-/-	**neutrophil elastase deficient**
NETs	**neutrophil extracellular traps**
PCL	**periciliary liquid**
PE	**Phycoerythrin**
PEG	**polyethylenglycol**
PerCP	**Peridinin-chlorophyll-protein complex**
PMA	**Phorbol 12-myristse 13-acetate**
PR3	**proteinase 3**
ROS	**reactive oxygen species**
SD	**standard deviation**
SEM	**standard error of the mean**
SLPI	**secretory leukocyte protease inhibitor**
TAMRA	**carboxytetramethylrhodamine**
Tg	**Transgenic**
TIMP1	**tissue inhibitor of matrix metalloproteinase**
TLR	**toll-like receptor**
WT	**wild type**

List of figures

List of tables

Abstract

Airways muco-obstruction and irreversible neutrophil-driven inflammation cause bronchiectasis in lung diseases such as cystic fibrosis (CF) and chronic obstructive pulmonary diseases (COPD).

To enter the airway lumen, neutrophils secrete their proteases, namely cathepsin G (CG), neutrophil elastase (NE), proteinase 3 (PR3) and neutrophil serine protease 4 (NSP4). The released neutrophil serine proteases (NSPs) contribute directly and indirectly to the innate immunity. Released NSPs' action is usually counteracted by endogenous antiproteases. However, the delicate balance between these two components is broken in chronic inflammation. Strikingly, NSPs greedily associate to the surface of the secreting neutrophil, to the myriad of extracellular vesicles filling the airway fluid and to the tangled DNA webs made of neutrophil extracellular traps (NETs). When fastened to such structures, NSPs seem to be less accessible to antiproteases and their persisting activity damages the connective tissue. As a result, more proinflammatory stimuli are released and the outcome is a vicious cycle leading to non-resolving airway neutrophilia.

In order to expand our palette of fluorescent tools and to propose an alternative drug target and inflammatory biomarker, we developed of a new series of Förster resonance energy transfer (FRET)-based reporters, which revealed high cathepsin G activity in CF and COPD airways. Also, we were inspired by the demand of novel advanced diagnostic technologies to examine sputum samples in a hospital environment. Therefore, we established a new assay based on the combination of spatially localized FRET probes and flow cytometry. This combination was shown to be a valuable diagnostic technique applicable in a basic and translational biomedical context. The simplicity and throughput of the new method opened the doors to two novel biomedically relevant projects.

First, to identify new inflammatory markers, we investigated the discriminants and common traits of inflammation in CF and COPD airways. We carried out a comprehensive characterization of sputum samples via analysis of protease activities, cytokines and antiprotease levels. We found that COPD airways appear to be characterized by less severe inflammation featuring elevated but not uttermost marker levels, compared to CF airways. As a key marker, high membrane-bound protease activity was the most significant indicator for COPD, suggesting this trait as a highly relevant early-inflammation biomarker.

Second, we wondered if in addition to the neutrophil surface, CF- and COPD-derived exosomes carry active NE and how to measure such activity at a single nanoparticle level.

Therefore, we adapted our cytometric assay to monitor protease activity on human sputum particles as small as 100 nm in diameter. We showed that CF exosomes acquired NE at their surface in the inflamed airways and exported it to surrounding cells.

Finally, we synthesized small-molecule probes designed to attach to DNA with the help of a DNA minor groove binder (Hoechst). The respective reporters were able to detect and quantify NE and CG activity on NETs, making them valuable tools to study the eclectic effect these enzymes have when embedded in DNA webs. Our reporters revealed that DNA-bound NE retained its catalytical activity. When applied to 5 µm mouse lung slices, the probe allowed to both distinguish single cell nuclei and to quantify cell-specific NE activity within the section.

In conclusion, the activity of enzymes like CG and NE can now be studied with unprecedented spatial resolution. Furthermore, this work brings a flow cytometric assay into biomedical research which, in combination with an expanding palette of FRET-based tools, bears the potential to allow for rapid and detailed diagnosis and treatment evaluation for lung disease patients, ideally at the early stage of the disease.

Zusammenfassung

Schleimobstruktion und irreversible neutrophile Entzündung verursachen eine ausgedehnte Bronchiektasie bei Lungenerkrankungen wie Mukoviszidose (CF) und Chronisch Obstruktiven Lungenerkrankungen (COPD).

Um in das Atemwegslumen zu gelangen, sezernieren Neutrophile ihre Proteasen, nämlich Cathepsin G (CG), Neutrophile elastase (NE), Proteinase 3 (PR3) und Neutrophil Serin Protease 4 (NSP4). Die freigesetzten neutrophilen Serinproteasen (NSPs) tragen direkt und indirekt zur angeborenen Immunität bei. Der Wirkung von freigesetzten NSPs wird normalerweise durch endogene Antiproteasen entgegengewirkt. Das empfindliche Gleichgewicht zwischen diesen beiden Komponenten fehlt jedoch bei chronischen Entzündungen völlig. Überraschenderweise, verbinden sich NSPs gierig mit der Oberfläche des sekretierenden Neutrophilen, mit der Vielzahl extrazellulärer Vesikel, die die Atemwegsflüssigkeit füllen, und mit den verwickelten Netzen aus neutrophil extracellular traps (NETs). Wenn NSPs an solchen Strukturen befestigt sind, scheinen sie für Antiproteasen weniger zugänglich zu sein, und ihre anhaltende Aktivität führt zu einer Schädigung des Bindegewebes. Infolgedessen werden mehr proinflammatorische Stimuli freigesetzt und das Ergebnis ist ein Teufelskreis, der zu einer nicht auflösenden Neutrophilie der Atemwege führt.

Um unsere Palette an fluoreszierenden Reportern zu erweitern und ein alternatives Wirkstoffziel und einen entzündlichen Biomarker vorzuschlagen, haben wir eine neue Serie von Reportern auf der Basis des Förster resonance energy transfer (FRET) entwickelt, die eine hohe Cathepsin-G-Aktivität in CF- und COPD-Atemwegen zeigten. Wir waren auch bewegt von der Nachfrage nach neuartigen fortschrittlichen Diagnosetechnologien zur Untersuchung von Sputumproben. Daher haben wir einen neuen Assay etabliert, der auf der Kombination einer lokalisierten FRET-Sonde basiert, die für die Flow Cytometry verwendet wird. Es wurde gezeigt, dass diese Kombination eine wertvolle diagnostische Technik ist, die in grundlegenden und translationalen biomedizinischen Kontexten anwendbar ist. Die Einfachheit und der Throughput der neuen Methode öffneten die Türen zu zwei neuartigen biomedizinisch relevanten Projekten.

Um neue Entzündungsmarker zu identifizieren, untersuchten wir zunächst die Diskriminanten und häufigen Merkmale von Entzündungen in CF- und COPD-Atemwegen. Wir führten eine umfassende Charakterisierung von Sputumproben durch Analyse der Proteaseaktivitäten, Zytokine und Antiprotease-Schutz durch. Wir fanden heraus, dass COPD-Atemwege im Vergleich zu CF-Atemwegen durch eine Situation weniger schwerer Entzündungen

gekennzeichnet zu sein scheinen, die erhöhte, aber nicht äußerste Markerwerte aufweisen. Als key Marker war eine hohe membrangebundene Proteaseaktivität der signifikanteste Indikator für den Krankheitstyp, was darauf hindeutet, dass dieses Merkmal ein hoch relevanter Biomarker für frühe Entzündungen ist.

Zweitens fragten wir uns, ob CF- und COPD-Exosomen zusätzlich zur Neutrophilenoberfläche aktives NE tragen und wie diese Aktivität auf einer einzelnen Nanopartikelebene gemessen werden kann. Daher haben wir einen zytometrischen Assay entwickelt, um die Proteaseaktivität auf menschlichen Sputumpartikeln mit einem Durchmesser von nur 100 nm zu überwachen. Wir haben gezeigt, dass CF-Exosomen NE an ihrer Oberfläche in den entzündeten Atemwegen aufnehmen und in die umgebenden Zellen exportieren.

Schließlich synthetisierten wir small molecule probes, die mit Hilfe einer Hoechst-Einheit (DNA-Minor-Groove-Binder) an DNA binden sollen. Die jeweiligen Reporter konnten die NE- und CG-Aktivität auf NETs nachweisen und quantifizieren, was sie zu wertvollen Werkzeugen machte, um den eklektischen Effekt dieser Enzyme zu untersuchen, wenn sie in DNA-Netze eingebettet sind. Im Gegensatz zu früheren Befunden zeigten unsere Reporter, dass DNA-gebundenes NE, jedoch nicht CG, seine katalytische Aktivität beibehält. Bei Anwendung auf ganze Maus-Lungenschnitte konnte die Sonde sowohl einzelne Zellkerne unterscheiden als auch die zellspezifische NE-Aktivität quantifizieren.

Zusammenfassend kann die Aktivität von Enzymen wie CG und NE nun mit beispielloser räumlicher Auflösung untersucht werden. Darüber hinaus bringt diese Arbeit einen flow cytometry Assay in die biomedizinische Forschung ein, der in Kombination mit einer wachsenden Palette von FRET-basierten Werkzeugen das Potenzial bietet, eine schnelle und detaillierte Diagnose und Bewertung der Behandlung von Patienten mit Lungenerkrankungen zu ermöglichen.

1. Introduction

1.1 Lungs as protective barrier

The respiratory tract is one of the most recent yet exquisitely complex systems evolved to allow gas exchange in most terrestrial animals[1].

Inevitably, lungs turn out to be also the first site of contact for most pathogens and noxious agents[2]. The lung's innate and adaptive immunity interplay via continuous information exchange (i.e. cytokine), providing a solid defense platform to such external cues[1]. Inside the airways, a mucus gel layer, 0.5 to 5 µm thick, covers the cilia and the epithelium forming a mesh of about 500 nm^2 pore size. Inhaled agents which escape the mucin trap come in contact with a mosaic of secretory, basal and multiciliated cells (coating the proximal airways) and pneumocytes (coating the alveoli) composing the lung epithelium[3–5]. Such cells are capable of orchestrating an effective immune response via secreting antibacterial compounds (lactoferrins, defensins and ROS), antiproteases (elafin and SLPI) and surfactants (SP-A and SP-D), via tightening the transepithelial resistance through junctions and remodeling the cytoskeleton[6,7]. Also, in response to bacterial (TLRs and NODs) or sterile (IL-1) inflammation[8] the epithelium releases a plethora of cytokines: IL-8 is the major neutrophil chemoattractant into the airways while IL-33 initiates a Type 2 inflammatory response[7]. Importantly, most of these mechanisms are inducible, therefore can be therapeutically manipulated[7].

The lung epithelium is not only the platform where inflammation develops and progresses but it is also the most affected component for mutations in the CFTR gene (the cause of cystic fibrosis) and it is the primary site of molecular and histological changes in both cystic fibrosis (CF) and chronic obstructive pulmonary disease (COPD) lung diseases (**Figure 1**)[9–11].

1.2 CF and COPD airways

Lung homeostasis relies on the interplay of physical barriers, epithelium, microbiome and adaptive and innate immune cells[4]. Cystic fibrosis (CF) lung disease exemplarily demonstrates how an irreversible shift from such equilibrium culminates in morbidity and mortality[12]. This genetic autosomal recessive disease is due to mutations in the *CFTR* gene encoding for a channel mainly localized at the apical surface of ciliated cells and pulmonary ionocytes[13,14]. Over 1700 mutations have been reported to occur in the *CFTR* gene. Despite ~15% of them

do not result in any clinical manifestation, class I, II and III type of mutations cause the channel to be absent from the cell surface or its regulation to be defective. Class IV, V and VI type of mutations leave the CFTR channel with some residual function, hence the patients show a milder disease phenotype[15].

The mutated CFTR protein is responsible for impaired chloride secretion, for sodium hyperabsorption and defective bicarbonate secretion into the airways[9,15,16] (**Figure 1**). The resulting pathological environment features i) mucus dehydration and stasis ii) altered pH which affects the function of antibacterial molecules, iii) promotion of anaerobic bacterial growth (such as the opportunistic pathogen *P. aeruginosa*), which altogether initiate and fuel airway inflammation (**Figure 1**). However, it was recently proposed that hypoxic necrosis of epithelial cells due to mucus thickening could be sufficient to trigger inflammation even in a sterile environment [17,18].

COPD is a general term referring to all conditions featuring irreversible and deteriorating long term poor airflow into the airways. COPD is the third leading and unopposed cause of death world-wide: in contrast to deaths due to cardiac diseases which decreased steadily in the last decades, the number of COPD cases has doubled[19].

The main cause of COPD is tobacco smoke, but a complex network of genetic (such as alpha-1-antitrypsin deficiency) and environmental cues contributes importantly to its onset and progression[10]. Even though COPD and CF diseases have distinct etiogenesis, they both converge to strikingly similar molecular phenotypes and disease manifestations. Indeed, proinflammatory and noxious agents contained in tobacco smoke and polluted breathing air induce CFTR misfunction directly, via inhibiting the channel activity, or indirectly, by inducing mucus thickening, dehydration and epithelium death (**Figure 1**). These result mainly in neutrophil infiltration, whose prominent mediators, the neutrophil serine proteases, cleave and activate the epithelial sodium channel (ENaC) and inhibit CFTR, thereby generating close similarity to CF's molecular landscape[20] (**Figure 1**).

1.3 Neutrophils shape the CF and COPD inflammatory microenvironment

Neutrophils are indispensable soldiers recruited to fight invading pathogens. They differentiate in the bone marrow from myeloid progenitors[21]. During the course of their maturation, neutrophils sequentially produce four different types of granules: primary, secondary, tertiary and secretory ones. These compartments serve as reservoirs of proinflammatory and

bactericidal substances (NADPH oxidase, myeloperoxidase, NSPs, lactoferrin) which are released upon specific signals via a process known as neutrophil degranulation[22]. Chronically inflamed airways experience continuous neutrophilic infiltration. Also known as polymorphonuclear cells (PMNs), neutrophils sense IL-8 and are polarized by signal-relay leukotriene B4 (LTB4) gradients to migrate to the site of inflammation[23].

Once having reached their destination (i.e. the inflamed lungs), neutrophils release their granular content, phagocytose and kill bacteria intracellularly. They also establish a continuous crosstalk with the surrounding epithelium, immune cells and the microbiome[24] (**Figure 1**). As a result, neutrophils actively contribute to the transformation of diseased airways into a poorly characterized microenvironment full of static mucus, a plethora of mediators of inflammation, bacteria, proinflammatory cytokines, filled up with extracellular DNA and vesicles (**Figure 1**) [25].

In such a context, a paradox unfolds: despite the large increase in neutrophil density, control of bacterial growth and virulence is far less efficient than expected. This contradiction may originate from altered local pH, defects in neutrophil secondary and tertiary granules release and “immunological exhaustion”, paving the way to the main pathogens colonizing CF airways (*P. aeruginosa* and *S. aureus*) and COPD ones (*H. influenzae*), as well as fungi such as *A. fumigatus* [26,27].

This apparent inability of neutrophils to dampen infection suggests that they might not be mere effectors of bacterial clearance, but could play additional distinct roles, raising questions about the unexplored concept of neutrophil plasticity.

The translocation of neutrophils to the inflamed airways has been linked to their general activation via degranulation (overexpression of CD63), loss of phagocytosis activity (sharp decrease in CD16 expression) and metabolic reprogramming (mTOR and NALP3 signaling mediated)[28–30]. However, it is unknown whether such activation is followed by a ramification in distinct subpopulations that would exert tailored functionalities and may underline diverse disease phenotypes or outcomes.

So far, the identification of putative subpopulations relied on analysis of individual marker genes, while a comprehensive picture of the covariance of multiple markers characterizing neutrophils in the bloodstream and upon translocation in the airways is missing[31,32]. Portraying neutrophil plasticity could have great value as a prognostic and diagnostic marker.

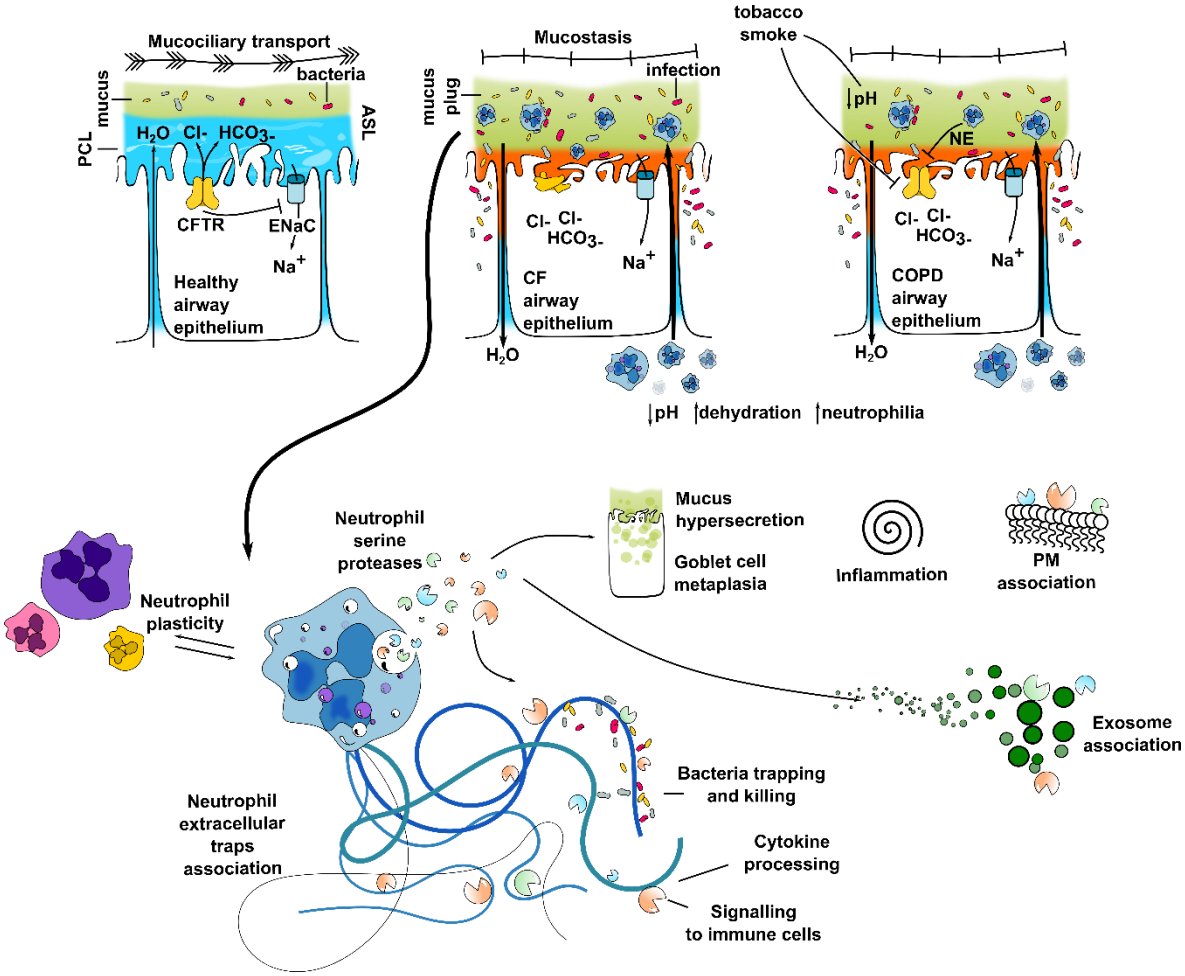

Figure 1 *From healthy, CF and COPD airways to disease molecular biomarkers. Genetic (i.e. CFTR defects) and/or environmental factors (i.e. tobacco smoke) cause non-resolving inflammation in the airways promoting mucostasis, continuous bacterial infections and substantial neutrophil infiltration. In turn, neutrophils propagate inflammation even further via secreting several mediators such as proteases. These enzymes, in addition to ECM remodeling, associate to the cell surface, to exosomes and to extracellular DNA where they function in a context dependent and poorly understood fashion. PCL = periciliary layer; ASL = air surface liquid, ENaC = epithelial sodium channel.*

1.4 Protease classes and substrate specificity

Proteases catalyze the hydrolysis of peptide bonds. The human genome encodes for 569 different proteases, which can be grouped in at least seven different classes according to the key residues involved in the catalytic action[33,34]. Most proteases belong to either the serine, cysteine, aspartyl or metalloproteinase class (**Figure 2 a**). Threonine, glutamic and asparagine ones are found less frequently, yet the proteasome catalytic subunits possess a threonine-type endopeptidase activity[35]. Proteases recognize their target substrate via an array of complementary interactions between the protease specificity pockets (S_n) and the corresponding substrate residues (P_n) (**Figure 2 b**). Generally, the shape and chemical space of the S1 pocket and the substrate residue N-terminal to the cleavage site (P1) mainly tune the specificity of serine proteases. For example, cathepsin G, which shows a chymotrypsin-like substrate specificity, accommodates large, hydrophobic aminoacids in its ample S1 pocket

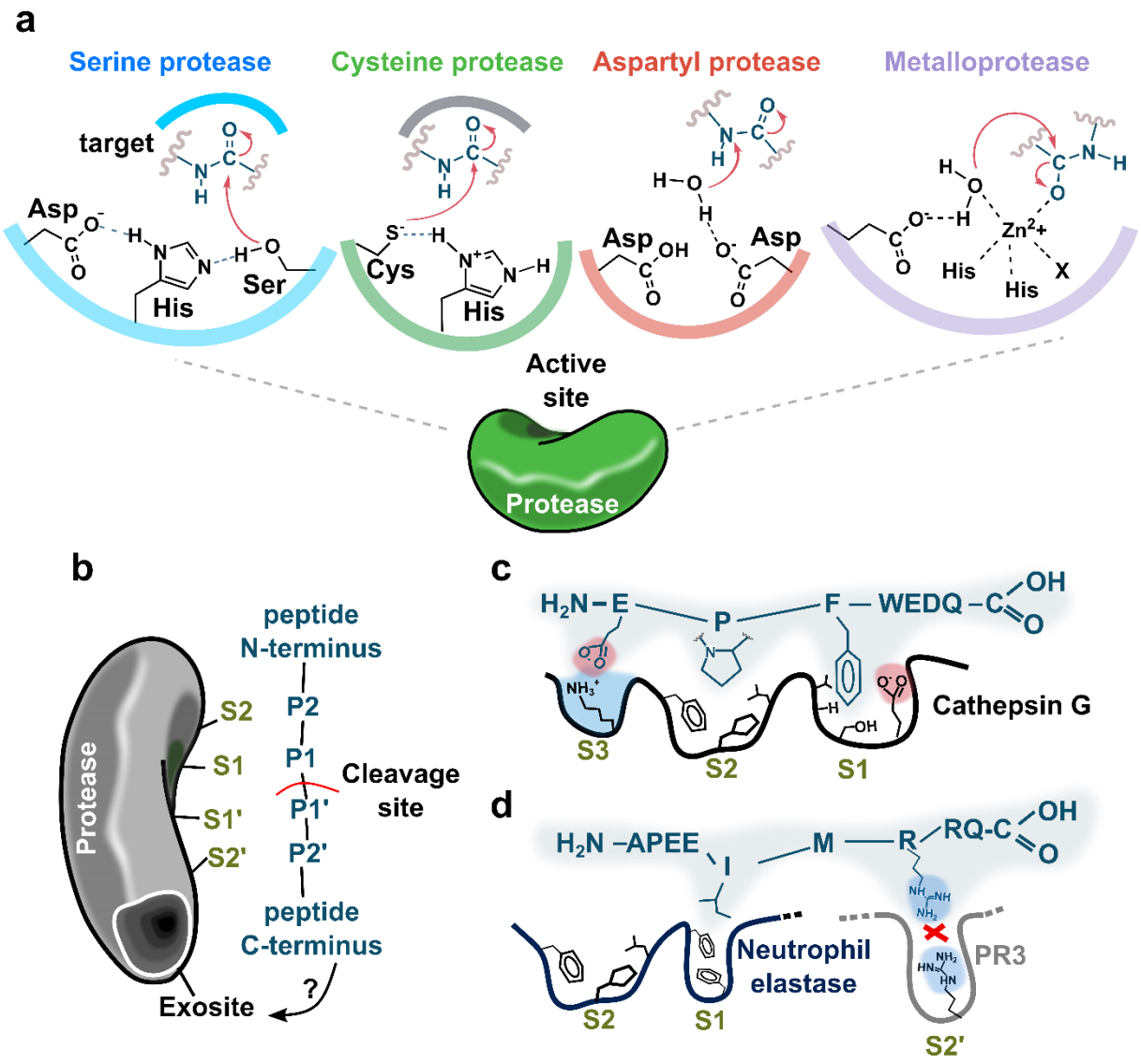

Figure 2 *Protease classes, mechanisms of action and substrate specificities. a) Schematic of the active site of serine, cysteine, aspartyl and metallo proteases. Serine and cysteine proteases catalyze the hydrolysis of the peptide bond via nucleophilic attack of the eponymous group. While in the serine and cysteine proteases the activation of the catalytic residue is mediated by a proton-withdrawing group, in aspartyl proteases and metalloproteases a water molecule becomes activated and functions as a nucleophile. b) According to the Schechter and Berger nomenclature, S pockets on the enzyme bind P residues at the N terminus of the scissile bond, whereas S' pockets bind P' residues after the cleavage site, towards the C terminus of the peptide. The presence of potential exosites which may contribute to protease specificity beyond the S' pockets is highlighted. c) Schematic of the S1, S2 and S3 pockets of cathepsin G which accommodate the synthetic substrate EPFWEDQ (N- to C- terminal) derived from the physiological cathepsin G substrate PAR-1. d) Schematic of the S2 and S1 pockets of neutrophil elastase and the S2' pocket of proteinase 3 bound to the synthetic substrate APEEIMRRQ (N- to C- terminal) derived from the physiological neutrophil elastase substrate PAI-1. The differences in the chemical environment of each pocket are exploited to develop specific substrates which can then be turned into protease reporters.*

(**Figure 2 c**). Inversely, neutrophil elastase and proteinase 3 (showing trypsin-like specificity) S1 pockets are narrow and packed with two phenylalanine and two valine residues (**Figure 2 d**). Therefore, only substrates featuring small hydrophobic residues at P1 will be recognized by NE and PR3 (**Figure 2 d**). In addition, the S2' pocket on proteinase 3 is positively charged, while it is flat and hydrophobic in neutrophil elastase[33]. These differences have been characterized, studied and exploited to generate more and more specific protease substrates and inhibitors. It should be highlighted that often proteases present exosites, defined as surface pockets different from the active site which contribute significantly to the protease specificity (**Figure 2 b**). Since exosites are poorly characterized and understood, their existence renders the design of protease specific substrates and inhibitors a more challenging task[33].

1.5 Neutrophil serine proteases (NSPs) pathobiology

NSPs are versatile tools in the neutrophil repertoire. Neutrophil elastase (NE), cathepsin G (CG), proteinase 3 (PR3) and neutrophil serine proteinase 4 (NSP4) are members of the chymotrypsin family of serine proteases[36]. NSPs proteolytic action relies on a so-called catalytic triad: an evolutionary conserved motif comprising a serine, an histidine and an aspartate residue[22](**Figure 2 a**).

NSPs are synthetized as pre-proforms which undergo four post-translational modifications to become fully active and targeted to neutrophil primary granules. Such post-translational modifications are carried out by two proteases: dipeptidyl peptidase I (DPPI) and cathepsin C. The evidence that cathepsin C activity is required for the correct activation and localization of

the four NSPs makes it an attractive yet unexplored anti-inflammatory drug target[37]. Primary or azurophilic granules bear a highly destructive arsenal of NSPs and myeloperoxidase. Therefore, they are used as last resort weapons. Indeed, neutrophils need to be sequentially challenged with priming (TNFα) and activating (FMLP or LPS) stimuli to secrete their primary granule content[38,39]. Furthermore, it has been recently proposed that different types of primary granules exist, each hosting a single NSP. However, the underlying molecular mechanism and functional consequences of such discriminatory packaging system remain obscure[40].

NSPs are deeply involved in starting and propagating inflammation. They act as potent bactericidal compounds inside the phagolysosome: neutrophil elastase has a primary noxious effect on Gram-negative bacteria, while cathepsin G is responsible for Gram-positive (e.g. *S. aureus*) infection clearance. In addition, they act as potent mediators of inflammation in the extracellular environment, by cleaving and activating cytokines and surface receptors [22,41].

Moreover, NSPs evolved different substrate specificities which result in the activation of distinct parallel proinflammatory pathways, creating a network of complex protease relationships far from being understood[33,41]. A key factor in the regulation of protease networks is the action of the endogenous antiprotease shield. During the course of lasting airway inflammation development, for instance in CF, the continuous secretion of proteases overcomes the stoichiometric ratio of proteases/antiproteases, setting the stage for chronicity[42].

So far, monitoring of the protease/antiprotease balance as a clinical parameter focused on measuring NE concentration and activity in soluble fractions of patient airways[43]. However, NSPs also bind to the plasma membrane via a combination of electrostatic and hydrophobic interactions[38]. Such association has a strong impact on the way NSPs and neutrophils propagate inflammation: at the cell surface NSPs become inaccessible to antiproteases and this masking effect increases with the size of the inhibitor[39]. From the clinical standpoint, it therefore becomes crucial to monitor membrane-bound protease activity to catch the earliest stage of inflammation, when the protease/antiprotease balance is still unbroken[44].

Finally, mutations in genes encoding for NSPs or for proteins responsible for their correct maturation (i.e. dipeptidyl peptidase I, DPPI) cause several hereditary diseases, such as Papillon–Lefèvre syndrome, acute promyelocytic leukaemia and Wegener's granulomatosis[22]. Therefore, advancing the knowledge of NSPs biology will become fundamental in the fight against these conditions.

1.5.1 Neutrophil elastase (NE)

Among NSPs, neutrophil elastase has been the most studied so far. At the pathophysiological level, increased and uncontrolled NE secretion in response to inflammation causes goblet cells metaplasia, mucus hypersecretion, CFTR inactivation and extracellular matrix remodeling into the ariways[26]. In addition, neutrophil elastase turned out to be an extremely valuable biomarker and predictor for CF lung disease severity and outcome. In fact, CF infants whose bronchoalveolar lavage (BAL) show elevated NE activity are more likely to develop bronchiectasis[43]. These studies laid the foundations for the detailed explorations of neutrophil elastase in CF.

First, the NEmo series of FRET probes was developed to allow real time quantification of NE activity in a spatially localized fashion[45]. Importantly, NEmo-2 is a FRET reporter which is equipped with a palmitic acid anchor that renders the visualization and quantification of NE at the neutrophil surface possible. Next, the β-ENaC overexpressing cystic fibrosis-like mouse model[46] was crossed with a mouse lacking for the NE-encoding gene (*ELA2*). The β-ENaC model overexpresses the ENaC sodium channel (**Figure 1**) and phenocopies ion transport defects observed in human CF lungs. As a result, airway surface liquid (ASL) depletion, reduced mucus transport, mucus obstruction and neutrophil-driven inflammation are common features of β-ENaC-Tg mice[46]. The phenotypic characterization of β-ENaC-Tg/NE$^{-/-}$ mice led to the discovery that NE absence reduced emphysema development, mucus plugs and neutrophilic infiltration into the airways[47]. Applied to this model, NEmo FRET probes showed undetectable NE activity in the soluble fractions of mouse lungs, but elevated activity on the neutrophil surface. These results indicated that despite free NE activity was shielded by BAL fluid antiproteases, membrane-bound NE was active, masked from inhibitors and therefore contributing to ECM remodeling and tissue damage[47]. Last, a human study involving adult CF patients demonstrated that membrane-bound NE activity negatively correlated with pulmonary function[44].

Despite the significant advancement of knowledge fueled by these studies, targeting NE via small molecule inhibitors never resulted in marketed therapeutics[48].

Similarly to CF, COPD airways feature elevated NE activity and a COPD-like mouse model lacking NE is protected from emphysema development[49]. However, NE activity on the cell surface was never investigated in the context of COPD airways.

1.5.2 Cathepsin G (CG)

Cathepsin G is the most phylogenetically distant among neutrophil serine proteases[36,40]. Like other NSPs, it participates in inflammation: it processes cytokines like CXCL5, which in turn recruit neutrophils. In concert with NE, it activates TNFα and IL-1β and cleaves protease-activated receptors (PARs) on the epithelium which in turn activate phospholipase C and NF-κB[22,50].

Unlike other NSPs, CG can activate integrins when it localizes to the neutrophil surface, thereby promoting cytoskeleton rearrangement[51]. Furthermore, CG binds to the membrane receptor formyl peptide receptor (FPR). This association leads to calcium ion influx, mitogen-activated protein kinase activation and protein kinase C translocation, promoting cathepsin G-induced chemotactic activity in neutrophils[50,51]. Extracellularly, CG specifically modulates inflammation, given its unique role in activating two members of the IL-1 family, IL-36α and IL-36β[41].

The variety of unique and shared functionalities of CG is nested into the intricate and poorly understood protease social network. The existence of such complex relationships might explain why targeting NE alone proved insufficient and highlights the need for tools to untangle the protease network[42,52]. Finally, we lack any information on the possible correlation of CG activity with CF and COPD disease progression. Indeed, its utility as a clinical biomarker could not be explored so far, caused by the lack of appropriate tools and animal models.

1.5.3 Proteinase 3 (PR3)

Neutrophils secrete also proteinase 3. Its bactericidal activity consists mainly of indirect effects such as processing of human cathelicidin (hCAP18) to its active LL-37 form. Due to its different substrate specificity, PR3 but not NE cleaves and activates IL-18[33]. Also, PR3 uniquely processes IL-36γ and inactivates IL-33[53]. In addition, PR3 is a strong inducer of apoptosis in endothelial cells. Even though the mechanism of PR3 translocation into the endothelium and its molecular targets have not been clearly defined, cell clearance by apoptosis plays an important role in inflammation resolution[22,33].

Interestingly, PR3 plasma membrane association seems to be genetically determined: only a particular subset of neutrophils which express the membrane receptor CD177 will carry PR3 at their surface[54]. In fact, the interaction between CD177 and PR3 has been recently described[55]. Importantly, membrane-bound PR3 is then recognized by the anti-neutrophil

cytoplasmic autoantibodies (c-ANCA) which activate neutrophils in the bloodstream causing necrotizing vasculitis which results in the fatal autoimmune disease known as Wegener's granulomatosis (WG). A strong correlation between CD177/PR3 expression and WG disease severity has been found. On the other hand, a possible link between PR3 expression, secretion and membrane association and CF and COPD disease severity has not been explored yet.

1.6 Macrophage proteases contribute to chronic airway inflammation

Neutrophils dominate the cellular composition of inflamed CF airways. However, the role of other innate immune cells and their secreted products should not be underestimated in such context. In fact, despite the βENaC-Tg/NE$^{-/-}$ model clearly demonstrated NE involvement in the *in vivo* pathogenesis of CF-like lung disease, the protease activity was found to account for only about 50% of the observed structural lung damage. To search for additional players contributing to the alveolar damage, a whole-genome expression profiling study was carried out by Trojanek JB et al. This work showed that macrophage metalloproteinase 12 (MMP-12) contributed relevantly to tissue disruption in mice[56,57]. Also, the *MMP12* gene turned out to be strongly up-regulated in inflamed mice airways and its expression correlated with emphysema development. In addition, a link between polymorphism in *MMP12* (rs2276109) and the severity of lung disease was identified[57]. Importantly, a series of FRET probes which fueled and contributed to the aforementioned studies were generated. Similarly to NEmo-2, the MMP reporter LaRee-1 reporter localizes to macrophage surfaces and reports on MMP-12 activity. Strikingly, the lipidated LaRee-1 donor moiety is internalized after enzymatic cleavage generating a "memory" effect inside cells bearing active MMP-12 at their surface[58].

Cathepsin S (CatS) is a cysteine protease which is secreted in large amounts by tumor associated macrophages. Therefore, its activity has been largely exploited as tumor marker and to develop new contrast agents and imaging technologies for accurate tumor surgical resection[59,60]. Cathepsin S gene has been found to be overexpressed in adult CF patient airways as well[61]. Recently, βENaC-Tg mice were crossed with CatS deficient ones. The resulting βENaC-Tg/CatS $^{-/-}$ model showed reduced lung damage and mucus obstruction compared to the βENaC-Tg mouse. In addition, direct or indirect inhibition of CatS reduced airway inflammation and mucin production, indicating the strict involvement of cathepsin S in the pathogenesis of CF-like lung disease[61].

MMP-9 or gelatinase B is a matrix metalloprotease expressed by many cell types (epithelium, macrophages and neutrophils) whose activity has been found to be elevated in CF airways and serum. Also, a strong correlation (rho = -0.78) between CF adult patients lung functionality and MMP-9 was demonstrated[62] .

While fluorescent reporters to monitor MMP-12 and CatS activity were generated[59,60,63], the development of MMP-9 probes featuring excellent specificity and allowing for satisfactory spatiotemporal resolution has so far been hampered by several factors, including the protease's close similarity to other proteases such as MMP-2 and its broad substrate recognition ability[64].

1.7 Extracellular DNA and neutrophil extracellular traps in inflammation

Perhaps the most fascinating way neutrophils modulate inflammation and kill bacteria is the active release of their nuclear DNA into the extracellular space via a process known as neutrophil extracellular traps (NET) formation[65].

In 2004, Brinkmann and colleagues[65] noticed that, upon stimulation with phorbol myristate acetate (PMA) or LPS, neutrophils reacted by flattening their surface, forming membrane protrusions and secreting thin and fragile filaments in the extracellular space. Such membraneless fibers were composed of chromatin shaped in smooth stretches (15 nm in diameter) alternated to round domains (25 nm). Interestingly, the secreted DNA could aggregate and form threads hundreds of nanometers in length, in turn tangled into intricate webs whose function seemed to consist prevalently in hooking and containing bacteria[65]. The entire molecular pathway leading to NETs production has not been clearly understood yet[66]. However, the process relies on a strong ROS cytosolic production, generated by NADPH oxidase following RAF1 and MAP2 kinases activation. Importantly, neutrophil elastase (NE) is deeply involved in the cellular death pathway causing NETs[66,67]: when neutrophils are challenged with NETs stimulants, primary granules translocate into the nucleus and NE cleaves histones causing DNA decompaction together with the epigenetic modifier of histonic tails PAD4. In parallel, NE cytosolic fraction propagates the cascade of events via proteolysis of F-actin, hence impairment of cell structural maintenance, culminating in plasma membrane rupture and DNA secretion [67–69].

Since its recent discovery, the presence of neutrophil extracellular DNA has been linked to many inflammatory processes and not exclusively to bacteria trapping and killing. For example,

the main driver of pathogenesis in atherosclerosis is an uncontrolled secretion of IL-1β by macrophages. To become fully active, these cells require to be challenged sequentially by a priming and an activating stimulus. In atherosclerosis, the macrophage priming is mediated by cholesterol crystals, yet the activation mechanisms remained elusive. Neutrophil extracellular traps were found to be the missing link between the two stages: macrophages can phagocyte the released nucleic acid and become licensed to release proinflammatory cytokines as IL-1β, which in turn elicit an Th-17 driven inflammatory response[70].

In addition, NETs may play an important role in "dormant" cancer cell awakening. So far, a correlation between inflammation and cancer relapse has been observed but was never explained mechanistically[71]. To shed light on the molecular switches responsible for the reactivation of metastatic cells, Albrengues and colleagues[72] injected mice intravenously with breast cancer stem cells (murine D2.0R and human MCF-7 cell lines). Then, animals were challenged repeatedly with LPS to simulate a sustained airway inflammation. Such treatment led to the formation of aggressive lung metastases and to massive neutrophil infiltration. Importantly, NETosis inhibition or treatment with DNases prevented cancer formation, revealing that NETs were responsible for the re-entry of dormant cancer cells into the cell cycle[72].

Moreover, Extracellular DNA presence and accumulation turned out to be critical even for gallstones formation, which remains one of the most prevalent causes for hospitalization in the world[73]. The molecular mechanisms leading to gallstone formation were poorly understood until last year, when a team of researchers led by Martin Herrmann solved the puzzle and showed that extracellular DNA is a large component of gallstones and that NETs self-assemble into larger and larger structures promoting gallstones growth and crystallization[73].

Importantly, due to the enormous number of infiltrating neutrophils, CF and COPD airway mucus plugs are filled with DNA originated from "NETing", necroting and apoptotic cells[5,25]. In fact, the most widely adopted palliative treatment to alleviate CF lung disease symptoms consists in the inhalation of the DNase Dornase alpha (PULMOZYME®)[74]. However, nothing is known about the clinical and biological relevance of such DNA structures into the airways and their diagnostic potential remains to be understood.

Strikingly, DNA-bound neutrophil elastase activity was found to be directly responsible for many of the pathological conditions associated to NETs[72]. In fact, a proteome-wide screen of NETs components revealed that NE and CG are tightly associated to extracellular DNA[75,76]. Therefore, NETs might act as protease scaffolds: Albrengues and colleagues[72] showed that when bound to DNA, neutrophil elastase processes laminin-111 in the extracellular matrix.

Such remodeling exposes the cleaved product of laminin which is then recognized by an integrin β1 receptor culminating in the aforementioned cancer cell awakening[72].

Although it is clear that many of the NETs immunological features are mediated by the association of proteases to DNA, no spatio-temporal information on the protease activity in this physiological context has been achievable due to the lack of suitable tools. As a consequence, possible links among extracellular DNA content, its protease activity, the associated molecular signatures and disease severity could not be investigated so far. Also, such tools would reveal novel insights into molecular mechanisms underlying NETs formation.

1.8 Exosomes are active players in remodeling inflamed airways

Novel pathogenic entities in the COPD airways have been recently discovered: the “activated” neutrophil exosomes which carry at their surface active and antiprotease inaccessible NE and provoke emphysema in COPD patients[77].

Exosomes are lipid enclosed small particles (50-250 nm in diameter) secreted by almost any cell type in response to different stimuli. They form through the endolysosomal pathway and, once secreted, participate to cell-to-cell communication by carrying macromolecular messages (protein, miRNAs and mRNAs)[78]. Depending on the delivered molecules, exosomes mediate different cellular processes: they allow immune cells for “long-distance” communication, they dampen immune responses and promote cellular adhesion and motility in tumors[79]. Exosomes are also being exploited as “molecular cargoes” transporters for biotechnological and biomedical applications, given their broad biocompatibility and modularity[80].

At the molecular level, exosomes can be distinguished from other extracellular vesicles by the presence at their surface of tetraspanin receptors (CD9, CD81 and especially CD63), serving as “exosomal markers”[81].

In the context of chronic airway inflammation, CF neutrophil exosomes are capable of stimulating airway smooth muscle proliferation[82] which might in turn cause fibrosis. Further, exosomes derived from CF patient airways are 700-fold more concentrated compared to healthy controls[83]. This might be explained by the lower pH typical of inflamed airways, known to favor exosome trafficking among cells[84].

Given the challenges of handling and characterizing such minuscule entities, especially at the single nanoparticle level, NSPs activity on exosomes is hardly decipherable to date. Moreover,

in contrast to COPD, protease activity on CF exosomes has not been investigated so far, leaving the door open for their involvement in CF bronchiectasis.

1.9 A palette of tools to visualize enzymes and diseases

In the last decade, the combined effort of biologists, chemists and physicians resulted in the development of a variety of molecules, assays and imaging tools capable of lighting up protease activity in different settings, from cellular models up to entire living organisms. Many reached the clinics and are transforming surgeons' daily routine by enhancing the pre- and post- operative planning and diagnostics. *In-vivo* surgical guidance and "on fly" decision-making support will also become a reality in the near future[60].

Generally, disease- and context- dependent enzymes (esterases, hydrolases and proteases) are leveraged to visualize tumors, sites of inflammation and to quantify metabolic processes. A plethora of techniques serve this purpose, from fluorimetric read-outs, to advanced fluorescence microscopy and *in vivo* imaging via CT scans, PET and MRI[85–87]. Historically, the first types of protease reporters to be widely employed were the chromogenic ρ-nitroanilide based substrates[88] (**Figure 3 a**). By tuning the recognition motif of these molecules, which is flanked by the chromogenic part, more and more specific probes were synthetized. An increasing number of enzymes, ranging from cathepsins to caspases and bacterial proteins, can now be specifically studied thanks to the availability of tailored tools[60]. Such progresses were fueled by methods allowing a detailed characterization of the proteases' substrate preference at single S_n site resolution[52].

Importantly, Förster resonance energy transfer (FRET)-based probes found widespread applications as optical contrast agents and biomarker reporters due to their ability to measure the activity of an enzymatic target, their ratiometric read-out and their high signal-to-noise ratio[60]. To function, such molecules need a moiety which is recognized by the target enzyme and rely on FRET, a photophysical process where a donor fluorophore passes energy in non-radiative form to an acceptor molecule. To occur efficiently, FRET demands i) an overlap between the donor emission and acceptor absorption spectra, ii) the close proximity (< 10 nm) of the two molecules, iii) and the proper orientation of their dipoles. The processing operated by the target enzyme on the probe, usually the cleavage of the recognition part, results in the acceptor to diffuse away from the donor: the division of the donor and acceptor emission intensities over time generates a ratiometric read-out of the protein activity. FRET-based probes are usually classified in activity-based (ABPs) or substrate-based[89]. ABPs are often

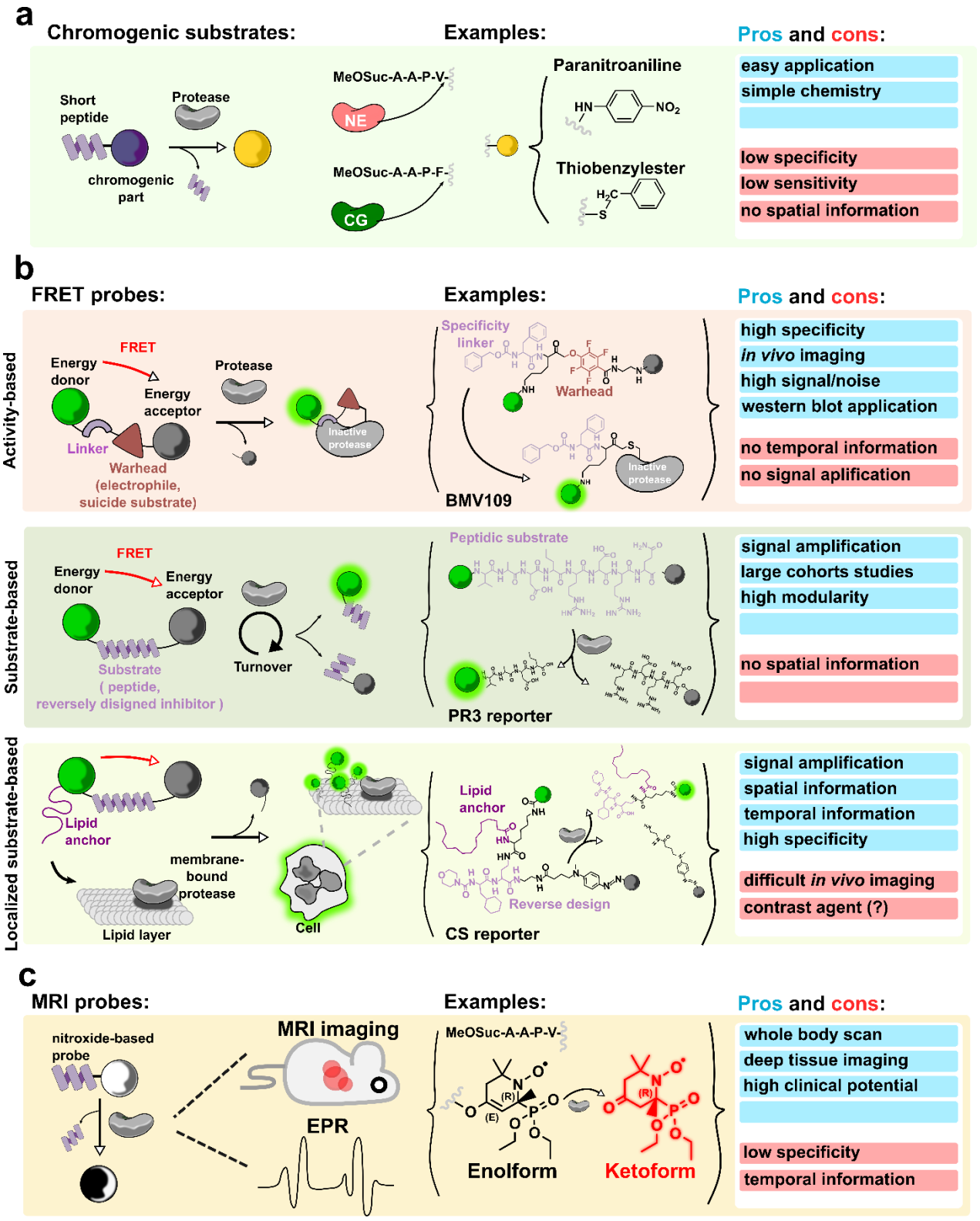

Figure 3 *General design, chemical structures and features of protease imaging tools. a) Chromogenic substrates are composed of a short peptide and a chromogenic part. The protease cleaves the bond between the two and the reaction can be monitored by measuring the absorbance shift (usually at ~ 400 nm). b) FRET probes can be divided in activity-based and substrate-based. The addition of chemical anchors confers substrate-based probes a precise spatial localization. c) MRI probes are characterized by a short substrate coupled to a ß-phosphorylated nitroxide moiety. The spectroscopic properties of the probe change upon enzymatic cleavage becoming detectable* in vitro *via Electronic Paramagnetic Resonance (EPR) and* in vivo *by MRI.*

composed of a small molecule suicide inhibitor (warhead) which covalently binds to the enzyme of interest yielding high specificity, signal retention and localization to the site of enzymatic activity (**Figure 3 b**)[60,89]. Often, the acceptor part of ABPs consists of a non-fluorescent dye, namely a quencher. The advantage of this strategy is the possibility to employ far-red fluorophores as energy donors which in turn allow for *in vivo* imaging, at the cost of losing the self-normalizing ratiometric readout. Probes belonging to the ABP class of molecules are exemplarily represented by the toolbox of cysteine cathepsin probes generated by Bogyo and colleagues over the years[90,91] (**Figure 3 b**). Such ABPs made *in vivo* imaging of cancer growth possible and revealed that cathepsins are strong promoters of tumorigenesis, opening the doors for their exploration as promising therapeutic targets[92,93].

On the other hand, the recognition motif of substrate-based FRET probes is a cleavable fragment (i.e. short peptide) whose products do not covalently bind the enzyme, ensuring for signal amplification via the continuous processing of intact reporter molecules[60] (**Figure 3 b**). Until recently, biomedical applications of substrate-based FRET probes were hampered by their intrinsic lack of spatial resolution due to diffusion and dilution of the reporter signal. To overcome such limitations, the insertion of molecular tags like lipid anchors or poly-L-lysine backbones for membrane and lysosomes targeting, respectively, permitted for a localized read-out[45,58,60] (**Figure 3 b**). Such strategy allowed for the development of LaRee-1 and NEmo-2, two plasma membrane-localized substrate-based FRET probes that fueled a deeper understanding of MMP-12 and NE proteases in cystic fibrosis, respectively[45,47,57,58]. Also the probe 3 developed by Hu et al.[59] bears a lipid anchor for cell surface localization. However, this probe is based on the "reverse design" principle: an optimized and specific inhibitor for cathepsin S was turned into a high turnover substrate by placing an amide bond close to the protease active center[59] (**Figure 3 b**).

Recently, probes bearing MRI detectable and positron emission tomography (PET) tracers (such as ^{11}C and ^{18}F) became excellent tools to image disease-specific and enzyme-mediated processes[94,95] (**Figure 3 c**). In the future, a specific and perfectly localized molecule bearing a PET tracer and a FRET pair would be employable for both the pre-operative planning and during surgery becoming an essential tool in the hands of pathologists and surgeons[60].

1.10 Searching for therapeutics and biomarkers in CF and COPD

In 2019, Food and Drug Administration (FDA) approved the use of Trikafta™ for the treatment of nearly 90% of the cystic fibrosis population. The revolutionary drug relies on the combination of two CFTR correctors (Elexacaftor and Tezacaftor) which stabilize the channel in its properly folded state and one potentiator (Ivacaftor) that shifts the channel equilibrium towards its open conformation. FEV1% predicted is a clinical parameter widely used to assess lung functionality. When administered to patients with at least one allele carrying the F508del mutation, Trikafta™ improved their lung functionality by an average of 14.3%, setting an unprecedented standard in CF treatment[96,97].

Unfortunately, such groundbreaking treatment is unlikely to stop antibiotic-resistant microbial infections to happen, to restore functionality of irreversibly damaged airways and to dampen chronic inflammation[15]. As a matter of fact, the 2019 *The Lancet Respiratory Medicine Commission* report section 2.2 highlights how developments in the early detection of inflammation, organ damage, and infection remain key challenges for the upcoming years[15]. Moreover, with the diffusion of new treatments, endpoints as FEV1% predicted value and frequency of exacerbation number are becoming less sensitive and poorly predictive of the disease status[9].

On the other hand, COPD remains an irreversible condition, with no cure available on the market. In addition, very few valuable biomarkers for mortality and lung function decline have been identified, despite the tremendous economic, social and health burden this pathology represents. These indicators include the 6 min walk distance (6MWD), white cell count (WCC), and blood levels of fibrinogen, C reactive protein (CRP), IL-6 and IL-8[98,99] . Unfortunately, they are generally considered to be “weak” markers, some do not even originate in the lung, and all of them fail to detect the disease in its earliest stages, which remains the hardest challenge for a successful COPD prognosis and treatment[100,101]. However, the decline in lung function observed in COPD patients, that was previously thought to be sudden, may start even decades before the first clinical signs appear. This data points to the premature presence of actors, such as proteases, capable of modeling a proinflammatory niche as early as in the asymptomatic COPD airway[100].

Proteases hold great promises not only as drug targets but also as biomarkers of inflammation, disease predictors and indicators of treatments efficacy. Therefore, the physiopathological networks they are embedded in still needs to be untangled with powerful chemical biology approaches. As importantly, advanced diagnostic technologies to examine sputum samples are required for the rapid characterization of new bio-indicators, the evaluation of anti-

inflammatory treatments and the description of cellular subsets in a personalized manner and on a large cohort basis.

1.11 Why does it matter? Proteases and inflammation in COVID-19 lung disease

In December 2019, a novel human virus named SARS-COV-2 was identified in the city of Wuhan and has since spread globally. As of April 24th, there are more than 2.7 million people affected by COVID-19 lung disease, and a mortality rate of approximately 6.99% has been calculated (https://www.worldometers.info/coronavirus/#countries).

SARS-COV-2 is a RNA virus whose genome main products are two polyproteins: pp1a and pp1ab[102]. The main coronavirus protease (M^{pro}) is responsible for the processing of the polyproteins into functional polypeptides. M^{pro} belongs to the chymotrypsin family of proteases and shows a unique cleavage specificity featuring a substrate recognition motif (S2 to S1') L-Q- / (S, A, G) which is not found in any other human protease. This key feature makes it the most attractive drug target among the 26 viral proteins, for M^{pro} inhibitors would interrupt viral replication and are unlikely to be toxic in humans[102,103].

Very importantly, such unique specificity can also be leveraged to turn M^{pro} inhibitors (which have been already developed) into activity- or substrate- based probes for the rapid and easy detection and diagnosis of SARS-COV-2 infection at the point-of-care via the analysis of nose swabs or sputum samples. Also, such compounds could be turned into MRI contrast agents and be employable for the univocal discrimination of SAR-COV-2 induced pneumonia from other interstitial pneumonia of bacterial origin.

The molecular elements of SARS-COV-2 responsible for its pathogenic mechanism are still mainly obscure[104,105]. It is though clear that pneumonia is the main cause of morbidity and mortality in severe COVID-19 patients. SARS-COV-2 seems to induce a tremendous immune response in the host, phenomenon known as cytokine release syndrome (CRS) or "cytokine storm". Among the plethora of inflammatory mediators pouring out the airways and the bloodstream, the main player seems to be IL-6, a proinflammatory cytokine secreted by activated leukocytes[104,106] . Blocking IL-6 or its receptor with anti-inflammatory compounds or antibodies may be an effective therapeutic strategy[105]. Repurposed IL-6 receptor antibodies like tocilizumab (Actemra, Roche) whose use is already FDA-approved for rheumatologic

disease are being currently tested worldwide for their effect to dampen the immune response in severe COVID-19 patients[107].

An important neutrophil and macrophage infiltration into the COVID-19 inflamed airways is well documented and the blood neutrophil-to-lymphocyte ratio seems to be a good disease severity predictor[105]. Interestingly, neutrophil elastase is a major player in pneumonia and promotes tissue damage which causes TNFα and IL6 over production and secretion. Therefore, it is reasonable to speculate that the NE/IL6 axis might contribute in setting the stage for the severe COVID-19 phenotype. In addition, the role neutrophils play and the potential of NSPs and macrophage proteases as inflammatory markers and their contribution to the profound lung disruption in COVID-19 patients remain completely uncharted territories.

Although the development of the aforementioned diagnostic tools and the study of viral proteases in COVID-19 lung disease is out of the scope of this thesis, the concepts we apply for probe design and to decipher inflammation may be translatable into the fight against the recently emerged disease.

2. Research aim and project overview

Overall, the goal of this project was to unravel the complexity of the neutrophil protease network in chronic airway inflammation at an unprecedented molecular resolution.

To obtain a more comprehensive picture of protease pathobiology, we expanded the panel of available FRET reporters to include cathepsin G, a poorly characterized NSP. To this goal, a novel series of probes to study cathepsin G at the cell surface and in human fluids needed to be synthetized and characterized in depth. These reporters aimed at studying cathepsin G pathomechanism in airway inflammation and validating it as drug target.

In parallel, we addressed our efforts to overcome present difficulties routinely encountered in the study of proteases in human sputum. To fill this gap, we aimed to design a new high throughput and broadly applicable assay based on flow cytometry. The set-up of such assay required i) the design and validation of a highly informative antibody panel to gate and study neutrophil phenotypes of interest and ii) the implementation of FRET reporters to correlate information on protease activity with neutrophil subsets and patient clinical parameters.

We next aimed at exploring the discriminants and common traits of inflammation in CF and COPD airways. To this end, the newly developed technologies were to be exploited to broadly characterize sputum samples via analysis of localized protease activities, cytokines, antiprotease levels and subsets of cellular populations. In addition, we hypothesized that a state of chronic airway inflammation could modify the neutrophil behavior in the blood stream. As a first step towards a better understanding of immune cell reprogramming at the systemic level, we aimed at evaluating the response of CF and healthy blood neutrophils to external cues such as priming and activating agents.

Finally, studying NSPs activity at neglected localizations is critically required to complete the picture of protease pathobiology and should to be considered when drugs are designed and anti-inflammatory treatments are evaluated. Therefore, an important demand was to investigate exosomes- and extracellular DNA-bound proteases. Quantifying NE activity in its exosome-bound form was achieved in bulk by immuno-capturing to magnetic beads or at the single nanoparticle level via a purification free cytometric assay. The transfer of exosome-bound NE on the surrounding epithelium was monitored but the effect in terms of tissue damage and triggering of inflammatory response remains to be evaluated.

The successful visualization of extracellular DNA-bound NE and CG activity required small molecule FRET probes to localize to the nucleic acids. This was achieved by tagging the

reporters with a DNA minor groove binder. The new probe set revealed new exciting biology of DNA-bound proteases and opened the door to translational projects correlating DNA content, protease activity and disease severity.

The paucity of anti-inflammatory strategies remains the most daunting challenge in chronic airway diseases. This project provides the instruments enabling a more comprehensive study of protease driven inflammation and provides new avenues for testing drug candidates in model organisms and human subjects. The potential applications expand beyond lung diseases.

3. Results

3.1 Part I

3.1.1 Biochemical characterization of a new set of cathepsin G FRET probes

To detect and quantify the activity of the serine protease cathepsin G in chronic airway inflammation, we designed and synthetized two reporters: mSAM and sSAM (**Figure 4 a**, see appendix for analytical data). Both reporters were synthetized via solid phase peptide

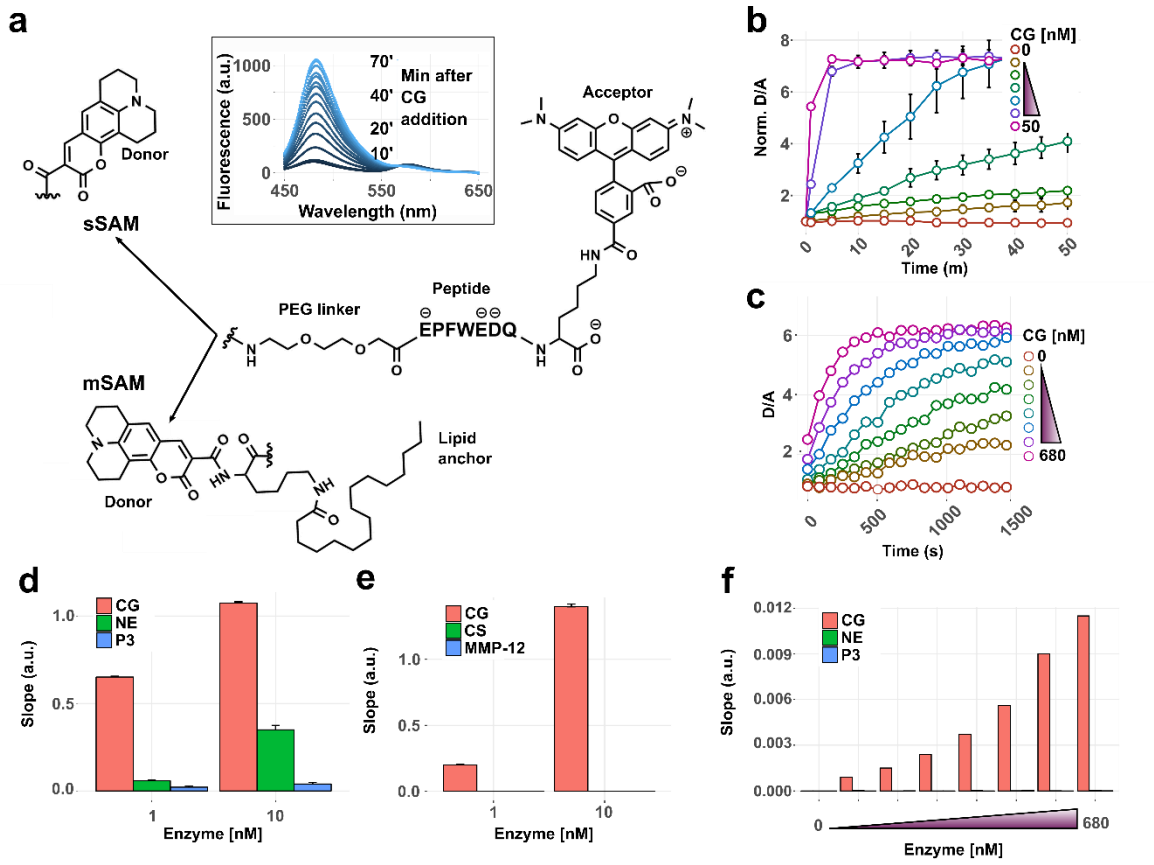

Figure 4 *Structure and cleavage characterization of spatially localized cathepsin G FRET reporters. a) Structures of sSAM and mSAM reporters. Top: representative line plot showing mSAM fluorescence signal increase recorded for 70 min after cathepsin G [1 nM] addition. b) Time dependent mSAM donor/acceptor ratio increase after addition of six different CG concentrations [50, 10, 1, 0.1, 0.05 and 0.01 nM]. c) Time dependent sSAM donor/acceptor ratio increase after addition of seven different CG concentrations [680, 340, 170, 85, 42.5, 21.25 and 10.75 nM]. d, e) Bar charts representing the log_{10} of linear regression slopes calculated from donor/acceptor ratio increase of mSAM incubated with either 1 and 10 [nM] of cathepsin G (CG), neutrophil elastase (NE), proteinase 3 (P3), cathepsin S (CS) or matrix-metallopreinase-12 (MMP-12). Mean ± sem of technical triplicates are shown. f) Bar charts showing sSAM cleavage rates calculated as in c) and d) of sSAM incubated with seven concentrations [680, 340, 170, 85, 42.5, 21.25 and 10.75 nM] of cathepsin G (CG), neutrophil elastase (NE) and proteinase 3 (P3). Figure adapted from Guerra M. et al., DOI: 10.1021/acscentsci.8b00933*

synthesis (SPPS). The strategy we employed was to carry out SPPS on a Wang resin coupled to a lysine whose side chain was protected with a 4-methyltrityl (Mtt) group. Differently from the widely used fluorenylmethyloxycarbonyl (Fmoc), which is a base labile protective group for amines, the Mtt groups is removed in slightly acidic solutions. Therefore, this design allowed for the full peptide (Fmoc-PEG-EPFWEDQ**K**, N- to C- terminal) to be grown on the resin. Eventually, the two fluorophores were installed via two consecutive orthogonal deprotection and coupling steps: the C-terminal lysine (**K**) was Mtt deprotected first and the TAMRA dye coupled, then the Fmoc deprotection of the N-terminus allowed for coumarin343 to be inserted (sSAM) or for a palmitoyl lysine to be coupled followed by coumarin 343 (mSAM). Therefore, both probes composed of a central peptide core, EPFWEDQ (N- to C- terminal) surrounded by coumarin343 (the energy donor) and 5-(6)-TAMRA (the energy acceptor) dyes. The aminoacid sequence was derived from the natural CG substrate PAR-1, was developed and optimized by Attucci et al.[108] , and proved to be highly specific over NE and PR3 (**Figure 4 d** and **f**). A short PEG linker separated the donor from the peptide: previous experience showed that a short dioxaoctane spacer placed in-between the dyes and the central peptide favored better enzyme-substrate recognition and improved general reporter solubility and membrane impermeability[45,63]. mSAM was also equipped with a lipid anchor (palmitic acid) that conferred the reporter the ability to associate to the cell surface, hence a precise spatial localization. Previously, such membrane anchoring strategy had turned out to be successful and granted membrane localization and signal stability for LaRee-1 and NEmo-2 probes, lipidated reporters which successfully monitored MMP-12 and NE activity, respectively[45,63]. Optimal substrate-based FRET probes should be recognized and cleaved at a specific amide bond (between the P1 and the P1' sites). Such univocal cleavage permits to achieve a satisfactory ratiometric readout and to avoid signal artifacts. Therefore, the presence of secondary cleavage sites needed to be assessed. We showed via HPLC-MS that the mSAM peptide was recognized and cleaved by cathepsin G exclusively between Trp and Phe (see appendix for cleavage site demonstration). When the probe was incubated with NE or PR3, no observable by-products could be detected.

Overall, sSAM reported on cathepsin G activity in human fluids (sputum, bronchoalveolar lavage, blood) while mSAM was useful to visualize the membrane-bound protease activity. mSAM's optimal excitation wavelength was found to be 430 nm (**Figure 4 a**, top panel) whereas sSAM was excited with a 405 nm laser. Coum343 and TAMRA λ max emission turned out to be around 480 nm and 580 nm respectively. In the presence of cathepsin G, the probes showed a time dependent increase of the donor fluorescence emission and a decrease in the

acceptor emission. This resulted in a ratiometric measurement of the reporter cleavage directly reflecting cathepsin G activity (**Figure 4 a**, top panel).

Both the reporters showed satisfactory *in vitro* sensitivity: mSAM discriminated CG activity in the picomolar range (**Figure 4 b**) while sSAM clearly distinguished CG activity as low as 10 nM (**Figure 4 c**).

To evaluate the reporters' *in vitro* specificity mSAM was incubated with the other two main neutrophil serine proteases (neutrophil elastase and proteinase 3), a major lysosomal cathepsin involved in progression of CF lung disease (cathepsin S) and a member of matrix metalloproteinases secreted by activated macrophages (MMP-12), respectively (**Figure 4 d** and **e**). None of the proteases significantly cleaved the reporter *in vitro*. sSAM was challenged with neutrophil elastase and proteinase 3, showing satisfactory specificity towards cathepsin G (**Figure 4 f**).

3.1.2 Evaluation of mSAM specificity, sensitivity and localization via confocal microscopy

mSAM is the lipidated FRET probe geared towards monitoring cathepsin G activity in a spatially localized fashion, namely at the neutrophil surface. In order to be a valuable tool for biomarker discovery and validation, mSAM should i) associate with the plasma membrane, ii) reside at the cell surface for the entire duration of the assay and iii) prove high sensitivity, an essential prerequisite for detecting early-inflammation.

First, we confirmed mSAM specificity via confocal microscopy of neutrophil-like cells (HL-60) incubated with either NE, P3 or CG. Only when cathepsin G was present, we detected a ~3-fold increase in the donor/acceptor ratio compared to the mock treated cells (**Figure 5 a**). Then, we confirmed that mSAM was capable of detecting CG concentrations as low as 2 nM at the surface of HL-60 cells (**Figure 5 b**). To visualize and confirm the localization of mSAM, HL-60 cells were co-incubated with a commercial plasma membrane stain and the FRET reporter. Then, the Pearson correlation coefficient (0.58 ± 0.1) and the area overlap (0.87 ± 0.05) between the two channels were calculated showing satisfactory colocalization and minimal internalization of the reporter after 20 min from reporter addition (**Figure 5 c**). mSAM showed comparable performance also on HEK293 cells (**Figure 5 d**) that we used as a model to demonstrate that, after addition of CG the ratio between the donor and acceptor emission intensities increased over time (**Figure 5 d**). Also, we wondered if mSAM could show a "memory effect" [63] due to the internalization of the hydrophobic donor moiety separated by the

negatively charged acceptor part after enzymatic cleavage. Neither on HL-60 nor on HEK293 cells (**Figure 5 d**) an increase of donor fluorescence in the cell cytosol after cleavage was observed. To confirm this, we synthetized the mSAM donor fragment and incubated it on HEK293 cells. No internalization of the fragment was observed even after one hour of imaging, indicating absence of “memory effect” and that the donor part was sufficient to grant cell surface retention (**Figure 5 e**). This observation may be explained by the presence of a negatively charged aminoacid (Glu) in mSAM's donor fragment which prevented its internalization (**Figure 5 e**), while LaRee1’s fragment was composed of exclusively hydrophobic residues (one proline and one leucine). Finally, mSAM proved a stable plasma membrane localization also on human bronchial epithelial cells (16HBE14o-) for up to one hour (data not shown).

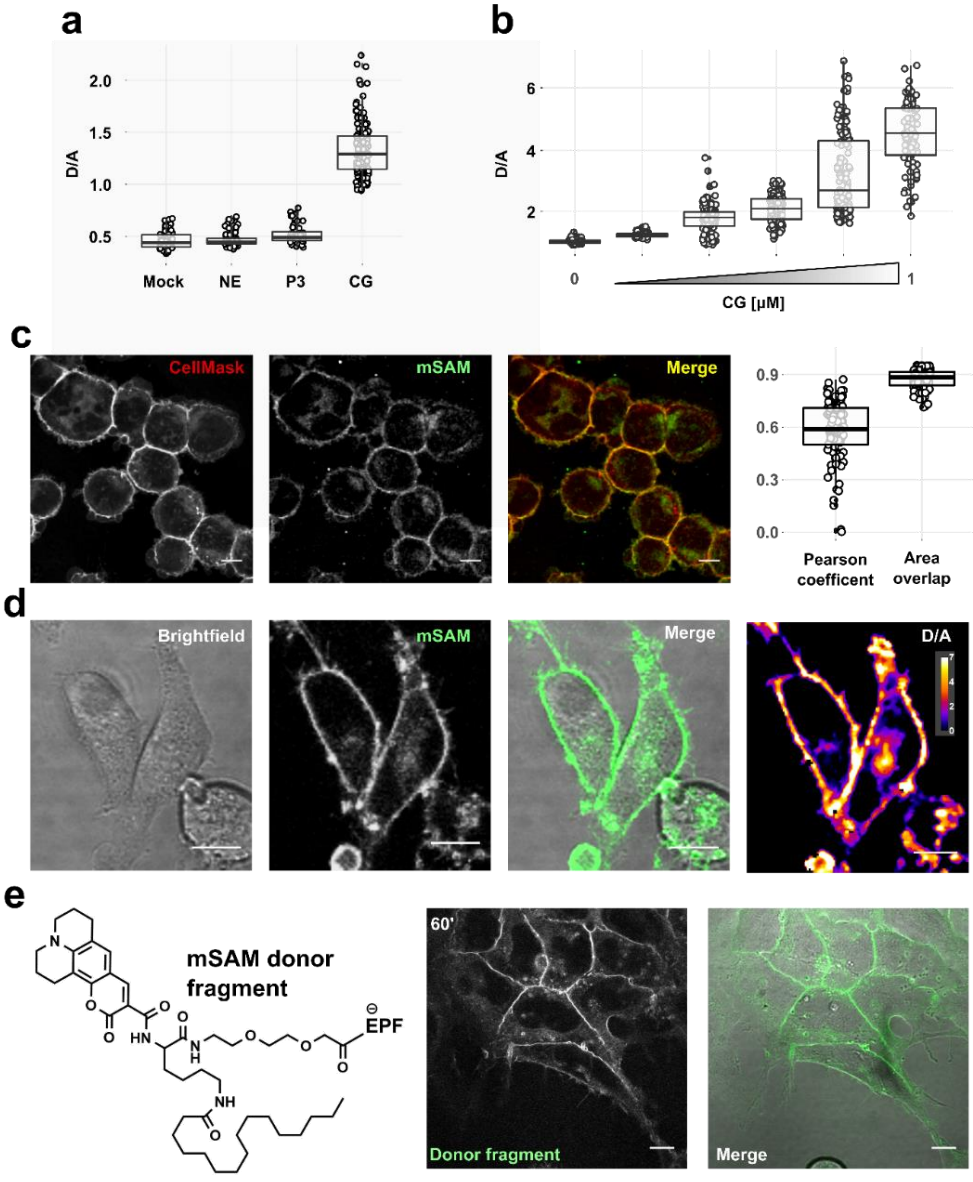

Figure 5 *Performance of mSAM in cellular models. a) Confocal microscopy quantification of donor/acceptor ratio increase at the surface of HL-60 cells incubated with mSAM [2 µM] after addition of either buffer (mock), neutrophil elastase (NE), proteinase 3 (P3) or cathepsin G (CG). N = 50-100 cells per group. b) Confocal microscopy quantification of donor/acceptor ratio increase at the surface of HL-60 cells incubated with mSAM [2 µM] after addition of five different cathepsin G concentrations [1, 0.2, 0.02, 0.002, 0.0002 µM]. N = 50-100 cells per group. c) Left panel: representative confocal microscopy images of HL-60 cells incubated with the commercial plasma membrane stain CellMask, mSAM and the merge of the two channels. Right panel: boxplots representing the Pearson correlation coefficient and area overlap between CellMask and mSAM channels. N = 101 cells, 2 replicates. d) Confocal microscopy images of HEK293 cells incubated with mSAM 30 min after addition of cathepsin G [1nM]. The right panel shows quantification of the enzyme dependent donor/acceptor (D/A) ratio increase. e) Chemical structure (left panel) and mSAM donor fragment cellular localization on HEK293 cells after 60 min incubation. Scale bars: 10 µm. Figure adapted from Guerra M. et al., DOI: 10.1021/acscentsci.8b00933*

3.1.3 Cathepsin G activity as a marker of chronic airway inflammation

We wondered if cathepsin G activity is increased in diseased human airways and therefore can be used as an inflammatory biomarker. Therefore, we employed mSAM and sSAM on healthy and CF sputum samples and COPD bronchial lavage (BL) fluids to quantify and spatially define CG activity in human airways.

The measurement of membrane-bound CG activity on sputum neutrophils from 10 healthy donors and 14 CF patients showed an average 3.03 increase in activity in the disease group (**Figure 6 a** and **b**). As far as soluble fractions are concerned, a similar situation was observed: CF sputum supernatants and COPD BL showed a 3.53 and 2.15-fold increase in CG activity compared to healthy sputum supernatants, respectively (**Figure 6 c**).

Given the complex nature of human sputum and bronchial lavages, we performed a series of experiments to confirm we were assessing univocally CG activity. Firstly, we incubated patient sputum with the endogenous antiprotease alpha-1-antichymotripsin (ACT) resulting in a marginal, non-significant increase in donor/acceptor ratio at the neutrophil surface (**Figure 6 d and f**). A similar result was observed when the small molecule cathepsin G inhibitor I (CGI) was added to sputum cells (**Figure 6 g**). In contrast, no decrease in FRET change was observed when the NE inhibitor Sivelestat was present, indicating that neutrophil elastase, despite being abundant in inflamed airways, was not responsible for any cleavage of mSAM (**Figure 6 g**). Similarly, the incubation of patient sputum supernatants with the small molecule cathepsin G inhibitor I led to complete inhibition of signal increase (**Figure 6 e**).

In addition to neutrophils and macrophages, the airway milieu can be populated by mast cells and basophils, especially in allergic conditions. Chymase is a chymotrypsin-like enzyme

secreted by mast cells, and, despite it does not associate to the cell surface, it shares extensive substrate recognition motif similarities with cathepsin G[37,109]. Therefore, chymase presence and activity in CF and COPD airways needed to be assessed carefully. Unfortunately, we observed that neither ACT nor CGI were capable of binding and inhibiting human mast cell chymase with similar potency as for CG (data not shown), making a simple inhibition assay insufficient for such purpose.

Attucci et al.[110], showed that chymase has a higher cleavage rate than cathepsin G on the substrate we employed (EPFQEDW). Accordingly, chymase cleaved sSAM more rapidly than any other protease tested in **Figure 4** (**Figure 6 h**). However, cathepsin G was still able to hydrolyze the reporter from 2.5 to 8 times faster when the two enzymes were incubated at the same molar concentration (**Figure 6 h**). Although unexpected, we hypothesize that this change stems from the introduction of bulky fluorophores and the PEG linker which may influence enzyme affinities. In addition, we quantified chymase activity by means of the Chymase Activity Assay Kit (CS1140, Merck. Darmstadt, Germany) which is cleaved by chymase and not CG (**Figure 6 i**). This substrate was then used for 10 CF sputum samples and 6 COPD lavages (**Figure 6 j**). No activity was detected in any of the COPD samples, and CF specimens showed an average of 24.7 nM active chymase (**Figure 6 j**, left panel). In parallel, the same CF samples were incubated with sSAM, revealing 488 nM active cathepsin G (**Figure 6 j**, right panel). These high signals cannot be explained by the low concentration of active chymase we measured (**Figure 6 j**, left panel).

We also quantified the overall chymase concentration in 16 CF and 8 COPD samples via ELISA (Human Mast Cell Chymase ELISA Kit, EKC34542, Biomatik). We detected an average of 7.1 nM and 0.1 nM chymase, respectively (**Figure 6 k**). At 7 nM concentration, chymase can only generate less than 1.4% of the cathepsin G signal in **Figure 6 j**, right panel.

The insignificant amount of chymase detected was in line with the histological cellular count of CF sputum and COPD BL. In CF, we quantified that neutrophils accounted for 90-99% of the overall cellular population, with the second most common population being represented by macrophages and occasionally epithelial cells. The concentration of mast cells did no go further than 0-0.5 %. A similar scenario was observed in COPD where neutrophil abundance was 50-90% of the total, followed, in different proportions, by macrophages and lymphocytes. If mast cell were present, we could not detect any.

Our general results and conclusions were supported by Fahy J. et al.[111] . In this study the authors could also not detect any tryptase (protease expressed and secreted together with chymase by mast cells) in 11 out of 12 of CF sputum specimens they analyzed, and they

reported the same range of cellular populations we observed. In conclusion, we excluded that our results were affected by mast cell chymase activity in the tested samples. However, we recommend that chymase quantity should be always checked especially in conditions characterized by mast cells infiltration.

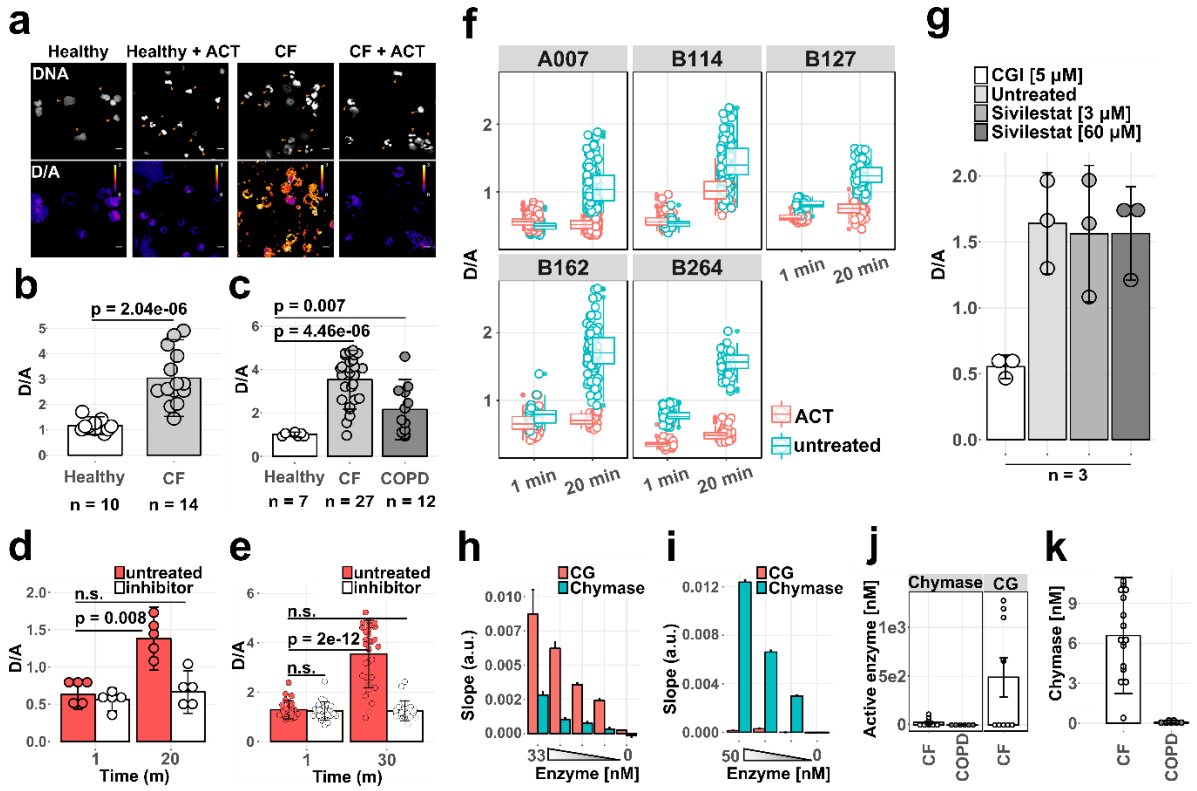

Figure 6 *mSAM and sSAM proved elevated cathepsin G activity on CF neutrophils and in CF sputum supernatant and COPD BL fluid. a) Confocal microscopy images of healthy and CF sputum neutrophils. Upper panel shows neutrophils segmented nuclei (orange arrowheads), the lower panel shows D/A ratio on neutrophils incubated or not with alpha-1-antichymotrypsin (ACT) 10 min before mSAM addition. b) Bar charts showing the quantification of CG activity on sputum neutrophils derived from 10 healthy donors and 14 CF patients. c) Bar charts showing the quantification of soluble CG activity derived from 7 healthy donor and 27 CF patient sputum supernatants and 12 COPD BL fluids. d) D/A ratio quantification of CG activity on neutrophils from 5 patients after 1 and 20 min incubation with mSAM and ACT [3 µM]. e) D/A ratio quantification of soluble CG activity in sputum supernatants in presence of the small molecule cathepsin G inhibitor I [25 µM]. f) Single cell confocal microscopy quantification of patient samples showed in d). g) Quantification of D/A increase on CF neutrophil 20 min after addition cathepsin G inhibitor I [5 µM] and sivelestat [3 and 60 µM]. h) Linear regression slopes derived from D/A ratio increase of sSAM incubated with 4 concentrations of human mast cell chymase and cathepsin G. i) Linear regression slopes derived from fluorescence increase of Suc-AAPF-PNA substrate incubated with CG or chymase. j) Quantification of chymase (left) and cathepsin G activity (right) in 10 CF and 6 COPD sputum samples via chymase activity assay kit (left panel) and mSAM (right panel). k) Quantification of total chymase amount via ELISA assay in 16 CF sputum samples and 7 COPD BL. Scale bars: 10 µm. For all the microscopy experiments 50-100 cells were imaged and analyzed. Each sample was prepared and imaged in duplicate. Bar charts show mean ± sd. Wilcoxon rank sum test was employed for statistics. Figure adapted from Guerra M. et al., DOI: 10.1021/acscentsci.8b00933*

3.1.4 Introducing small molecule FRET probes and flow cytometry into the clinics

FRET based protease quantification in human sputum by confocal microscopy is remarkably expensive and time consuming, low throughput and difficult to be widely adopted. To overcome all these difficulties, we implemented the use of mSAM into the flow cytometry technology.

The first step required the design of an antibody panel (**Table 1**) to discriminate among the major cellular populations present in human sputum: neutrophils, macrophages and epithelial

	Laser	Filter	Dye	Antibody	Localization
1	Blue	610/20	Pe-Dazzle 594	CD66b	membrane
2		780/60	Pe-Cy7	CD14	membrane
3	Red	670/14	Alexa Fluor 647	CD169	membrane
4		730/45	Alexa Fluor 700	CD16	membrane
5		780/60	APC-Cy7	CD45	membrane

Table 1 *Antibody panel employed for the for the set-up of sputum small molecule FRET flow cytometry and showed in in* ***Figure 7****.*

cells. The marker 7AAD was implemented to detect live cells. Overall, this panel allowed to selectively gate live neutrophils as 7AAD-, CD45+, CD66b+, CD16+, CD14-, $CD169^-$ cells both in healthy and CF samples (**Figure 7 a** and **b**).

To avoid any spillover of antibodies into the reporter channels, we kept the violet laser line free of surface markers and used the 450/50 nm detector as donor channel and the 585/42 nm detector as acceptor one for the FRET reporter. The division of the MFI measured in these two channels over time provided a ratiometric readout of protease activity on gated neutrophils by flow cytometry.

We isolated sputum cells as for microscopy, stained them with the antibody panel and subsequently with the reporter, immediately before flow cytometry.

A cathepsin G-dependent increase in the donor/acceptor ratio on selectively gated live patient neutrophils was observed over time (**Figure 7 c**). The active enzyme at the cell surface induced a shift of the donor over the acceptor channel providing a read out of reporter cleavage. Such shift was not observed on CF cells incubated with ACT and on healthy subject neutrophils, proving the specificity of the reporter and confirming the results observed by microscopy (**Figure 7 c, d** and **e**). As a proof of concept validation of the new method, we performed in parallel flow cytometry and confocal microscopy on 11 human samples (5 CF and 6 healthy)

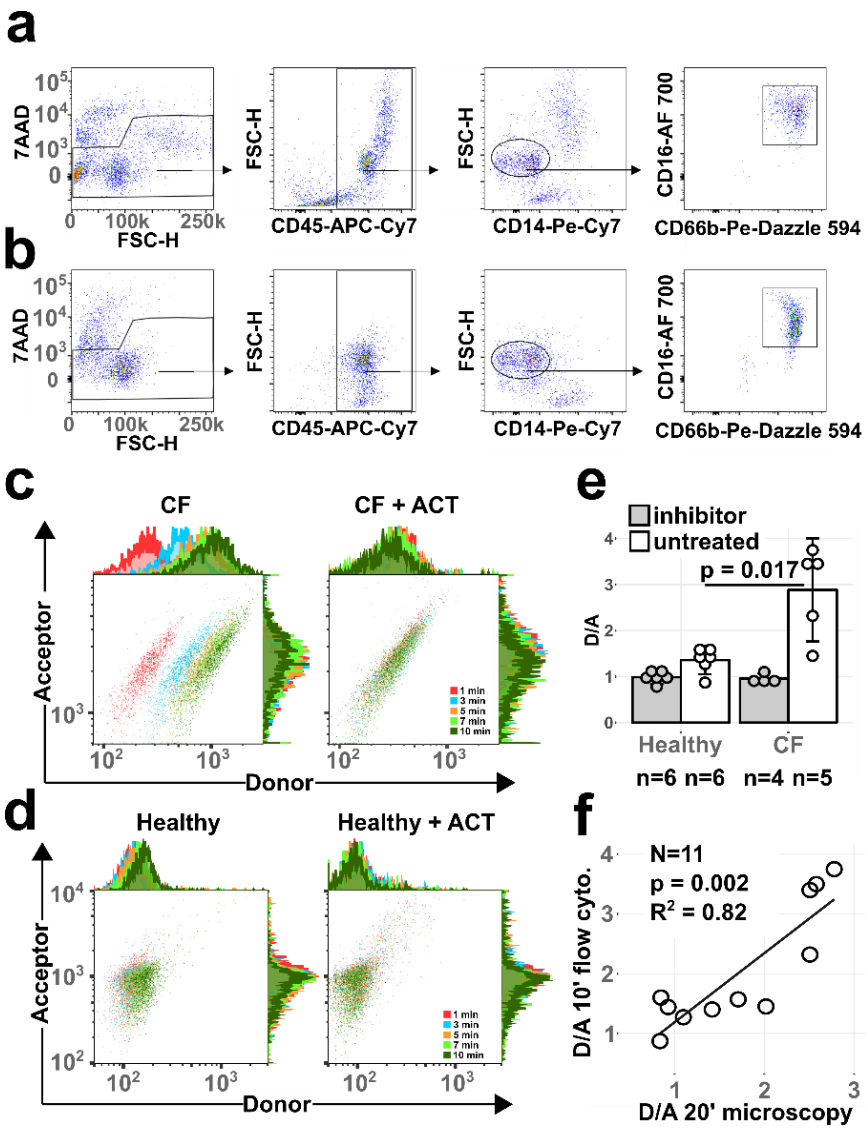

Figure 7 *Implementing small molecule FRET reporters into flow cytometry. a, b) Dot plots showing the strategy employed to gate healthy donors (a) and CF (b) live sputum neutrophils. c, d) Representative dot plots showing donor/acceptor ratio change at the surface of gated neutrophils by flow cytometry at five different time points after mSAM addition. e) Bar charts showing the quantification of the mean donor/acceptor ratio measured on sputum neutrophils derived from 6 healthy donors and 5 CF samples after 10 minutes and treated with ACT inhibitor. f) Correlation between paired flow cytometry and microscopy measurements on the 11 human samples showed in e). n= 50-70 for microscopy, n ≥ 1000 for flow cytometry. Data are represented as mean ± sd. Each human sample was measured in duplicate. Wilcoxon rank sum and Spearman rank correlation tests were employed for statistics. Figure adapted from Guerra M. et al., DOI: 10.1021/acscentsci.8b00933*

obtaining a significant correlation (rho =0.82; p = 0.002) between the two assays (**Figure 7 f**). Our ultimate goal was to prove small molecule FRET flow cytometry to be fully translatable into clinical diagnostics. Therefore, we developed an easily scalable, standardized and fully optimized protocol that can be shared among different research and medical sites. First, we identified the largest dynamic range reachable by small molecule FRET flow cytometry by

varying cell number, reporter concentration and starting donor/acceptor ratio by changing PMT voltage ratio (indicated as PMT for simplicity). These experiments were repeated for mSAM and NEmo-2. We identified that mSAM performs best when 250000 cells are incubated with 2µM of probe and the initial donor/acceptor ratio is set to 1:5 by changing the PMT voltages

	Laser	Filter	Dye	Antibody	Localization
1	Blue	610/20	Pe-Dazzle 594	CD66b	membrane
2		780/60	Pe-Cy7	CD14	membrane
3	Red	670/14	Alexa Fluor 647	CD63	membrane
4		730/45	Alexa Fluor 700	CD16	membrane
5		780/60	APC-Cy7	CD45	membrane

Table 2 *A "universal" antibody panel employed for the experiments showed in* ***Figure 9****.*

accordingly (**Figure 8**). Optimal conditions for NEmo-2 turned out to be: 2 µM reporter, 500000 cells and a 1:5 ratio (data not shown). Both probes reached the highest signal after 10 min of incubation. Additionally, bleed through of the donor into the acceptor channel was measured by incubating cells with the donor fragment whose chemical structure is shown in **Figure 3 e** (**Figure 8 d**).

In parallel, we redesigned the antibody panel to make it "universal", so that it could fully discriminate among cellular populations derived from blood, sputum and BL samples (**Table 2**). The second panel also includes CD63, a marker for neutrophil activation and exocytosis[112]. The combination of surface markers for gating and phenotyping shows how the assay can be used to correlate protease activity with a cellular phenotype of interest.

Since neutrophil elastase is recognized as the enzyme responsible for the connective tissue disruption in CF and COPD airways and an excellent predictor of bronchiectasis in CF infants[43] we focused on combining the use of flow cytometry with the lipidated FRET reporter NEmo-2, geared toward measuring membrane-bound NE (**Figure 9 a, b and c**). Compared to conventional microscopy (**Figure 9 d**), we demonstrated the higher robustness of the technology which also guaranteed for a larger dynamic range in the FRET change (**Figure 9 d**).

In clinical routine, when patients are evaluated for their lung functionality, their forced expiratory volume in one second (FEV1 %) is measured. Importantly, the FEV1 % predicted in CF patients correlated negatively with cell-bound NE activity measured by FRET flow cytometry

(**Figure 9 e**). When NE activity was measured for the same patients by microscopy the correlation resulted in a lower and less-significant trend (data not shown).

Overall, these results highlighted how small-molecule FRET flow cytometry scored better by analyzing fewer human samples via selectively gating on live-cells, specifically neutrophils, in a high-throughput manner and excluding the signal coming from any background or debris.

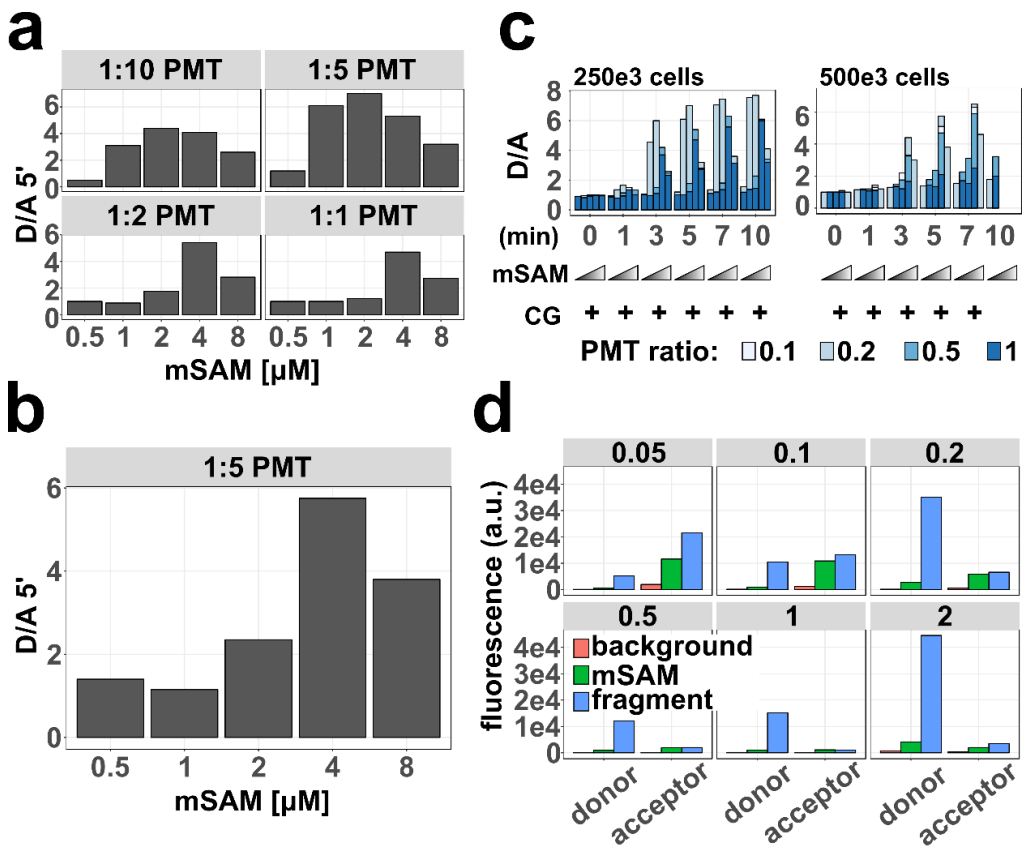

Figure 8 *Optimizing parameters for small molecule FRET flow cytometry. a) Bar charts showing changes in D/A values at different PMT voltages measured on HL-60 cells after 5 min incubation with CG [15 nM] and mSAM. b) D/A values measured at different mSAM concentrations c) General overview of D/A ratio values measured by tuning the number of stained cells, mSAM concentration and PMT ratio. d) MFI values measured for the donor and acceptor channel when cells where incubated with either mSAM or the donor fragment.*

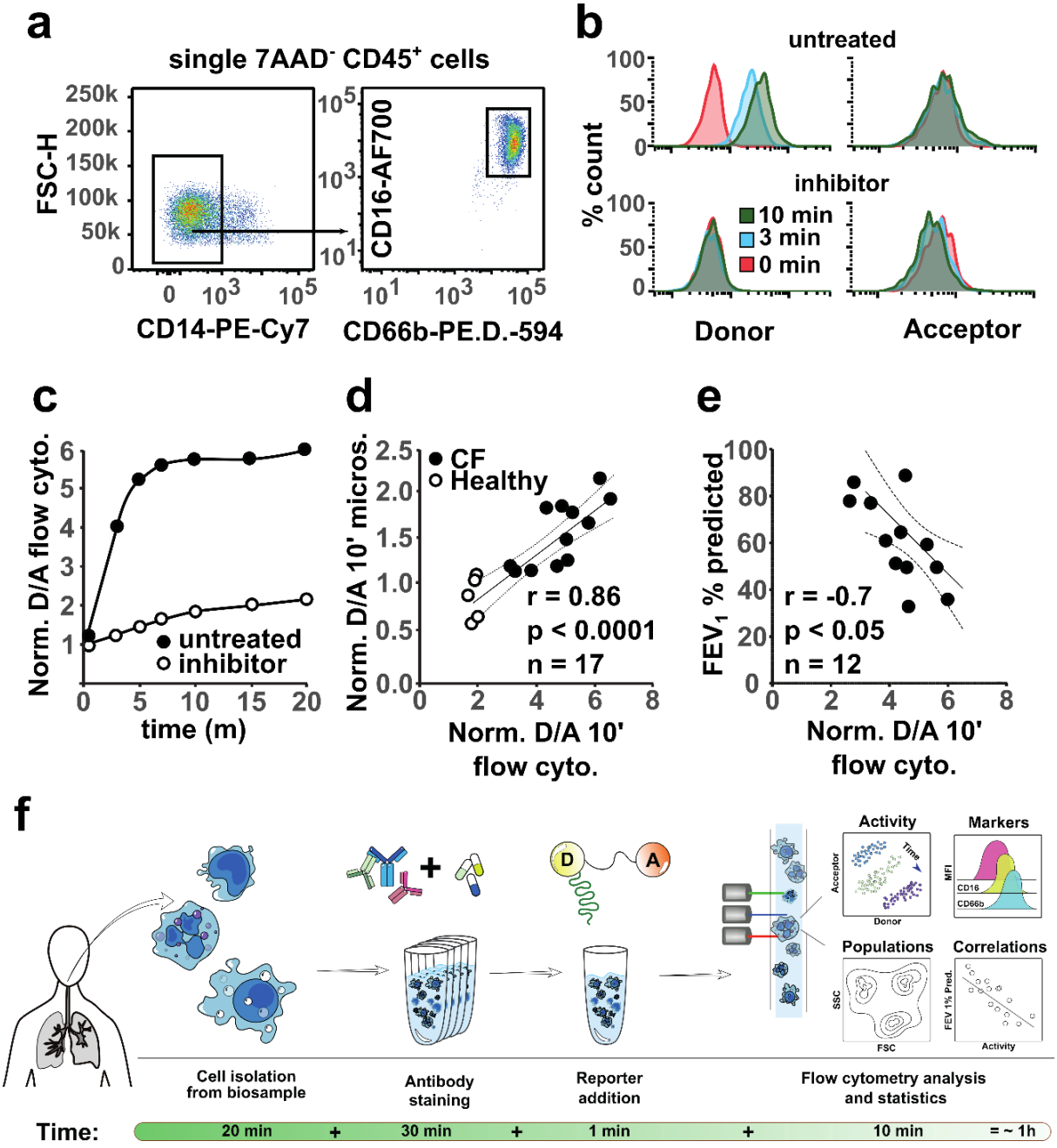

Figure 9 *Setting up a diagnostic assay to evaluate disease severity and anti-inflammatory treatments. a) Representative sputum neutrophil gating strategy. b) Mean fluorescence intensity of donor and acceptor channels measured for cells incubated with NEmo-2 in the presence or absence of the NE inhibitor Sivelestat. c) Donor/acceptor ratio increase on CF neutrophils treated or not with Sivelestat, normalized to the first time point measured for Sivelestat treated cells. d) Flow cytometry and confocal microscopy measurements correlation. e) Correlation between flow cytometry donor/acceptor ratio and FEV1% predicted measurements. Correlations were calculated via Spearman rank order method. f) Schematic of the workflow of small molecule FRET flow cytometry. Cells are isolated from the biosample, then stained with a proper antibody panel. Before measurement, the reporter is added and surface bound activity is detected over time and results are collected within one hour since the beginning of the procedure. Figure adapted from Hagner M.*, Frey D.*, Guerra M.* et al., DOI: 10.1183/13993003.02355-2019*

3.1.5 Expansion of readouts of small molecule FRET flow cytometry

Fueled by the increasing availability of probes, we envision that small molecule FRET flow cytometry will become a useful tool for the study of protease role in various diseases and on diverse cell types and human samples. For example, we measured MMP-12 activity on macrophages derived from BAL of one CF child by means of the lipidated FRET reporter LaRee1. The gating strategy and the signal increase we observed are shown in **Figure 10 a** and **b**.

The method was also easily adapted to study blood neutrophils, which will be described in the result part *"Assessing neutrophil behavior in the blood stream"***.**

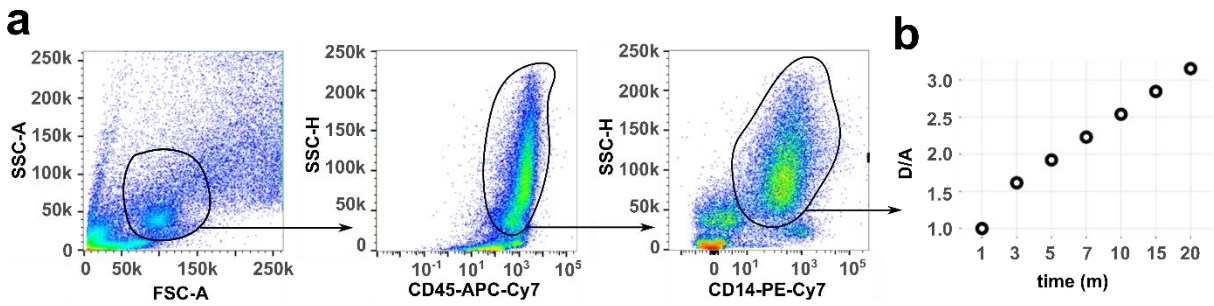

Figure 10 *Measurement of MMP-12 activity on CF children BAL macrophages via LaRee1 probe. a) Gating strategy employed to selectively monitor BAL macrophages. b) Time dependent increase in donor/acceptor ratio at the surface of macrophages after addition of LaRee1.*

3.2 Part II.

3.2.1 Differential patterns of NE activity in CF and COPD airways

The ultimate goal of this project was to characterize similarities and differences of CF and COPD airways in terms of mediators of inflammation as well as specific neutrophil phenotypes.

First, we quantified NE activity in sputum supernatant and on neutrophils of CF, COPD and healthy subjects (**Figure 11 a** and **b**). When compared to healthy controls, NE activity was significantly higher in disease. However, we found specific differences: CF supernatant contained more than two times active NE than COPD supernatant (**Figure 11 a**). In contrast, similar levels of membrane NE activity were observed on CF and COPD neutrophils (**Figure 11 b**). Interestingly, no changes in mucus weight and total protein content were measured which might have accounted for the diversity in NE activities among disease groups.

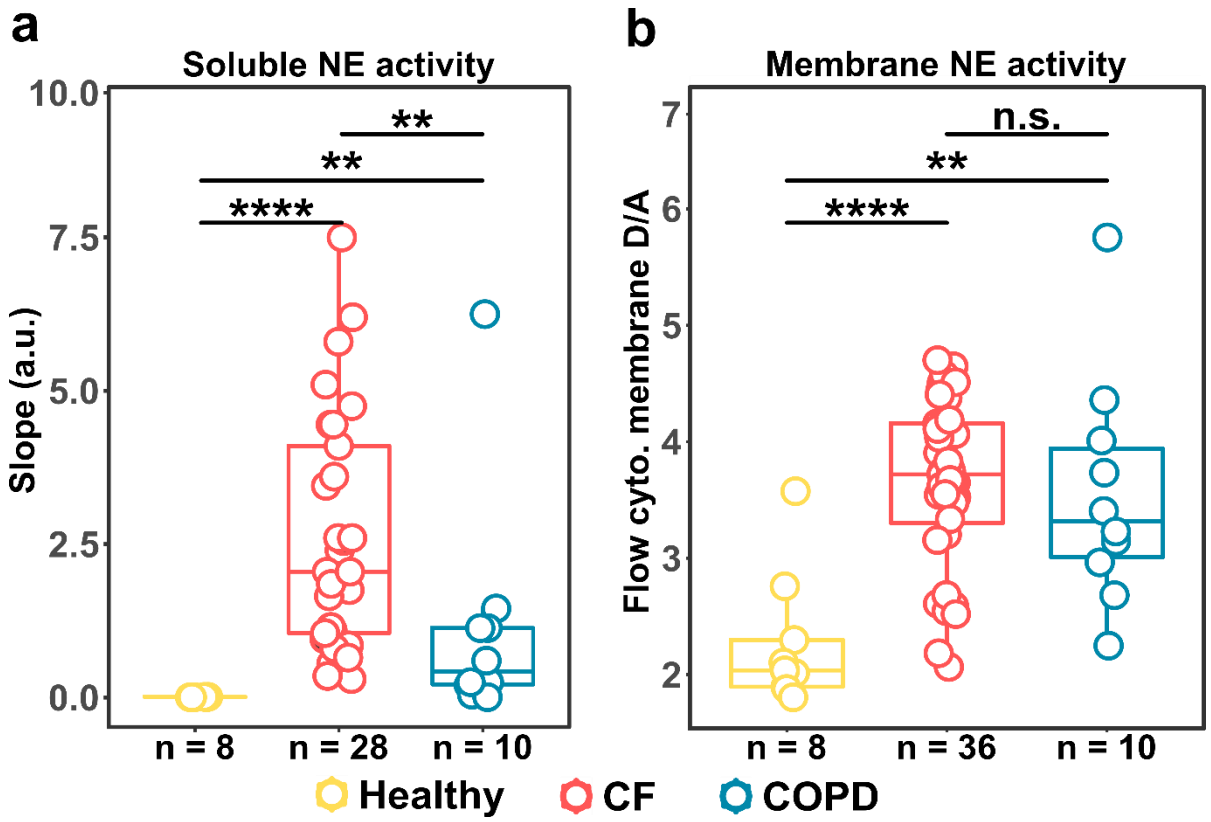

Figure 11 *Quantification of NE activity in disease and healthy airways. a) Fluorimetric quantification of soluble NE activity. The slope is calculated by linear regression of the donor/acceptor increase over time after incubation of the reporter NEmo-1 with sputum supernatants. CF group: mean = 2.4, sd = 1.9. COPD group = 1.1, sd = 1.9. b) Quantification of membrane-bound NE activity on neutrophils by FRET flow cytometry. Data are shown as donor/acceptor values after 10 min incubation with NEmo-2. CF group: mean = 3.6, sd = 0.7. COPD group = 3.6, sd = 1. Wilcoxon rank sum test was employed for statistics. **: p<0.01, ****: p<0.0001.*

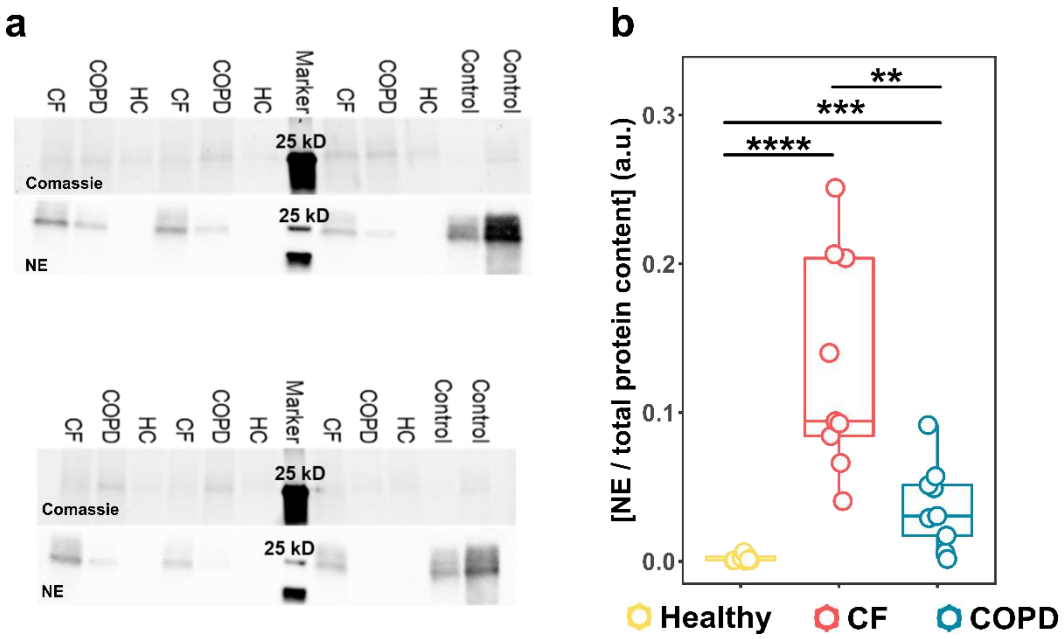

Figure 12 *NE total amount quantification in human sputum. a) Representative Comassie gel and Western blot membrane stained with an anti-NE antibody. Control: purified NE loaded at 2 different concentrations, 1 and 2.5 µg respectively. b) Quantification of normalized NE content derived from Western blot analysis. Wilcoxon rank sum test was employed for statistics. p<0.01, ***: p<0.001, ****: p<0.0001. N = 9 samples per group.*

The differences in soluble NE activity might not necessarily reflect a diverse total concentration of NE. Therefore, we performed Western blot analysis of 9 sputum supernatants for each group (CF, COPD and healthy) (**Figure 12 a**). When performing Western blot analysis on human sputum, it is good practice to normalize the antibody signal to the total protein content due to the unavailability of proper endogenous markers (i.e. GAPDH). We made sure that the exact same amount of protein was loaded on each lane by BCA quantification of sputum supernatant. Western blots reflected FRET measurements and showed that NE accounted for the 0.13 ± 0.07 % of the CF sputum total protein content, versus the 0.03 ± 0.03 % and the 0.002 ± 0.0019 % measured in COPD and healthy supernatant, respectively (**Figure 12 b**). In addition, the comparison of relative percentages of neutrophils, macrophages, eosinophils and lymphocytes in CF and COPD sputum revealed significant differences in neutrophil count (higher in CF) and eosinophils (higher in COPD) (**Figure 13**). These data indicate that factors present in CF airways may attract more neutrophils to the site and perhaps induce them to secrete more NE-containing primary granules.

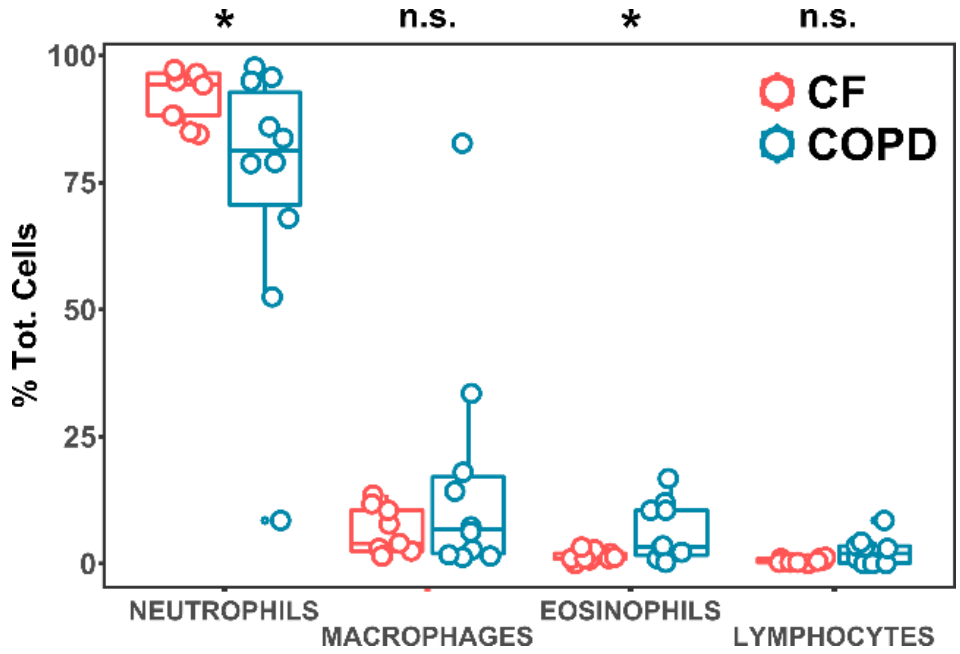

Figure 13 *Cytospin counts of four cell types in CF and COPD sputum samples. Wilcoxon rank sum test was employed for statistics. *: p<0.05. N = 8-10 patients per group.*

3.2.2 Cytokines and antiproteases are differentially expressed in CF and COPD airways

Alpha-1-antitrypsin (A1AT) is the antiprotease which defends tissues from inflammatory enzymes, especially neutrophil elastase. TIMP-1 is the main inhibitor of matrix metalloproteinases (MMPs)[113]. Neither A1AT or TIMP-1 levels resulted to be different between CF and COPD sputum (**Figure 14 a** and **b**). SLPI is an antiprotease and a target for active NE[113]. The concentration of the cleaved SLPI positively correlates with disease severity[114]. SLPI was the only protein whose levels were found higher in COPD (**Figure 14 c**), arguably in line with the lower amount of soluble NE in these samples. To rule out that different modes of neutrophil degranulation and consequent protease levels are connected to the presence (or absence) of unique inflammatory niches, we quantified the concentration of 7 pro- and anti-inflammatory cytokines in CF, COPD and healthy sputum. Among these, IL-8, a potent proinflammatory cytokine, showed intermediate levels of expression in COPD (**Figure 14 d**), while IL-10, a protective cytokine, was present in COPD at comparable levels to the healthy counterpart (**Figure 14 e**).

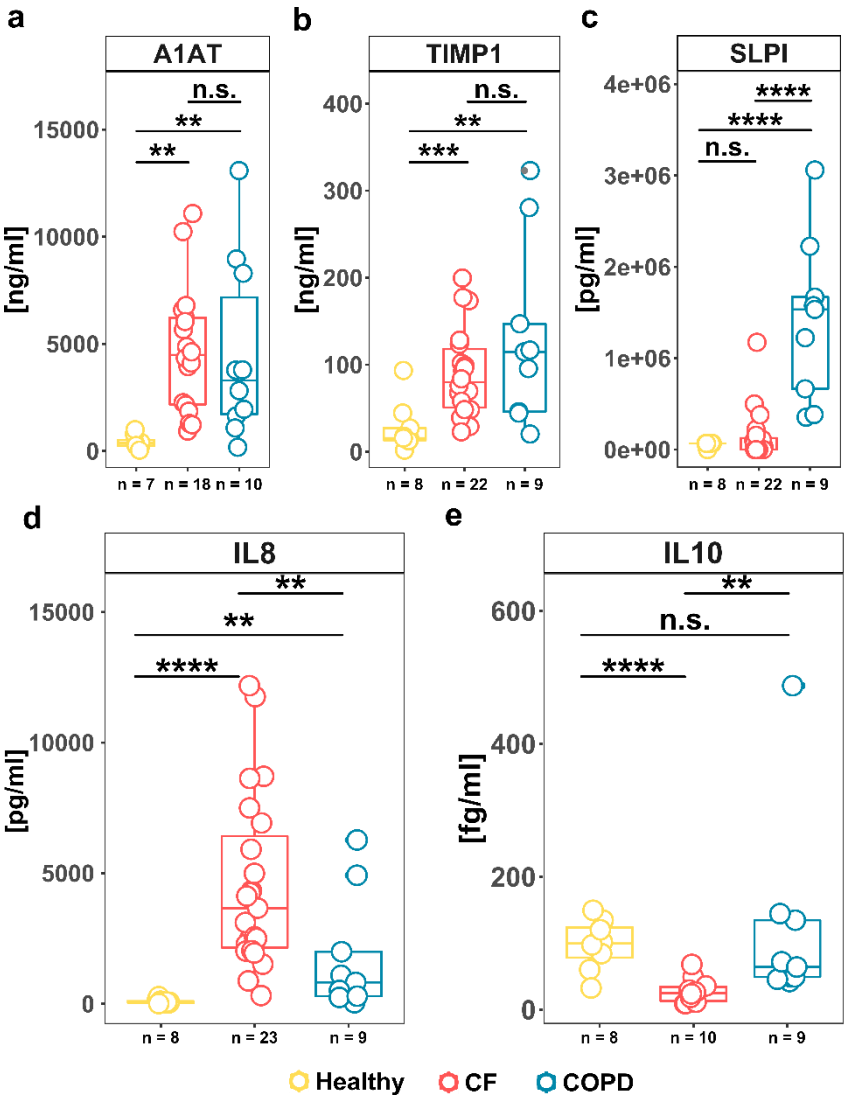

Figure 14 *Inflammatory factors in CF and COPD sputum samples.*

(a-c) Quantification of antiprotease content in sputum supernatants via ELISA assay.

(d, e) Representative quantification of pro- and anti- inflammatory cytokines in sputum supernatants via cytometric bead array (CBA) assay.

*The number of samples measured for each experiment is reported at the bottom of every graph. All statistics were calculated by Wilcoxon rank sum test (U test). **: p<0.01, ***: p<0.001, ****: p<0.0001.*

3.2.3 Computational analysis reveals distinct inflammatory landscapes

Principal Component Analysis (PCA) on the 13 variables (NE activities, antiprotease and cytokine levels) measured for 26 subjects demonstrated how the three groups (healthy, CF and COPD) were well separated by their expression levels of IL-8, IL-1β, TGF-β1, TNFα and soluble NE activity, with the latter being the best represented variable on the principal component one (**Figure 15 a**). On this axis, COPD are placed in-between CF and healthy for the intermediate concentration of pro-inflammatory factors. In addition, COPD data are separated along the second principal component by IL-6, IL-10, SLPI and IFN-γ.

Despite the milder inflammatory phenotype described in COPD, membrane-bound NE activity was the only proinflammatory factor whose expression level was shared between the COPD and CF group (**Figure 15 a**, 1st quadrant clockwise).

A heatmap on the same factors revealed how CF samples cluster by their very low levels of anti-inflammatory variables (top panel, left side branch, **Figure 15 b**) and very high pro-inflammatory ones (top panel, right side branch, **Figure 15 b**). A specular image was observed in the healthy group (middle panel, **Figure 15 b**) where anti-inflammatory agents and

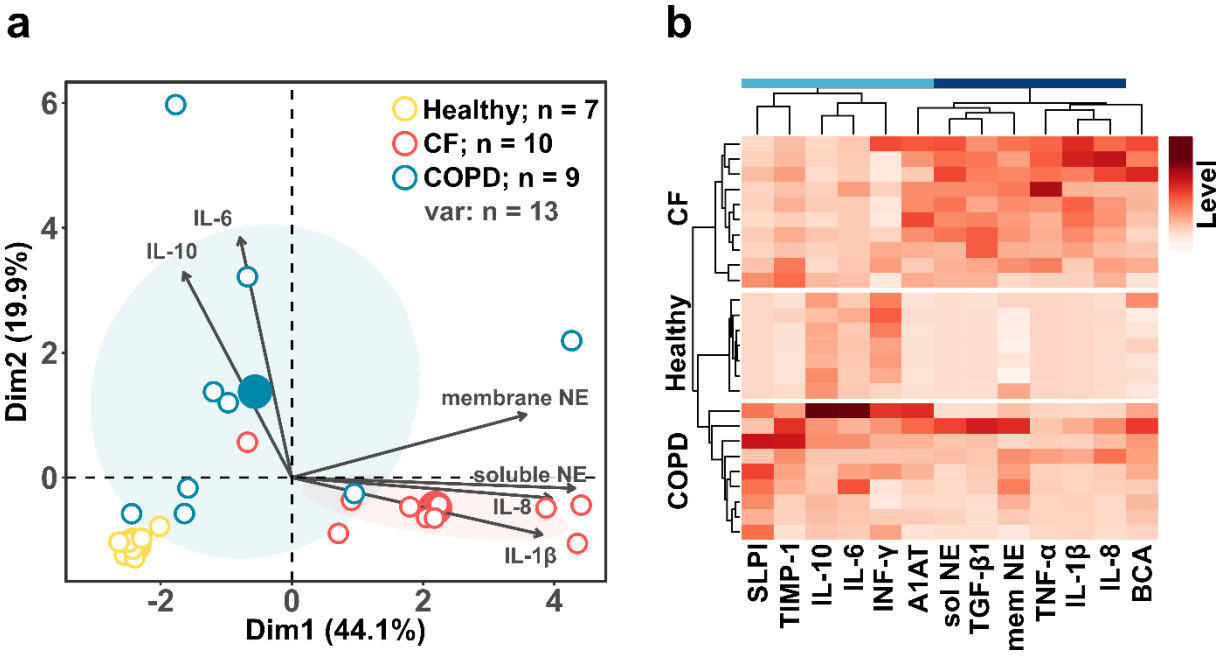

Figure 15 *PCA and heatmap of inflammatory factors in healthy, CF and COPD airways. a) PCA biplot including ellipses for the three types of disease. The dots represent the observations and they are colored by disease type. The larger dots represent the centre of the ellipse. Arrows represent the variables. The length of the variables indicates the quality of the variables to the factor map. Soluble NE is the variable which described the best the separation of healthy, CF and COPD along the Dim1 axis, while IL-6 on the Dim2 axis. Var = variables. (b) Heathmap of the 13 factors measured in sputum samples. Variables were clustered according to hierarchical clustering, patient annotation (CF, COPD and healthy) was defined manually.*

antiproteases were elevated. COPD proved to be a variegate group, with elevated inter- and intra-group variability (lower panel, **Figure 15 b**). Nonetheless, the only inflammatory factor which was uniformly elevated for most of the COPD samples turned out to be membrane-bound NE (**Figure 15 b**, "mem NE" column). The same variable was also the most down-regulated in the healthy group.

Singularly, the COPD scenario featured at the same time low soluble NE activity and high signal on neutrophil membranes. This concurrence has been also measured in the β-ENaC mouse model [47] and indirectly in CF children [112], both characterized by moderate inflammation.

In light of our data, elevated membrane NE seems a more evident and promising biomarker for early inflammation than before.

3.2.4 Characterization of CF and healthy sputum neutrophil phenotypes

To challenge our hypothesis that the three different inflammatory environments are linked to neutrophil plasticity, we designed a 12-color antibody panel (**Table 3**) meant to cover some of the possible phenotypes cells may acquire when exposed to different stimuli. Due to samples availability we initially focused on the characterizing differences between healthy and CF samples. After antibody titration, IgG controls and compensation set-up were carried out, 19 CF and 5 healthy sputa were stained and measured by flow cytometry. The resulting dataset was then analyzed by FlowSOM, an unsupervised machine learning algorithm which clusters multidimensional data [115] (**Figure 16 a**). Healthy neutrophils did not show variability of marker expression and were all centered around a phenotype which can be described as: $CD63^{low}$, $Arg1^{high}$, NE^{high}, $ICAM1^{high}$, $CD66b^{high}$, $CD45^{high}$, $CD16^{high}$ and $TLR4^{high}$ (left panel, **Figure 16 b** and **c**). In contrast, this population disappeared almost completely in CF neutrophils. In fact, the nodes which were populated by CF neutrophils showed generally a strong signal for CD63 (**Figure 16 c**, CD63 panel), but they were also separated by the differential expression of

	Laser	Filter	Dye	Antibody	Phenotype	Localization
1	Blue	530/30	FITC	CD63	NE secretion	membrane
2		575/26	PE	Arginase 1	Immuno suppression	intracellular
3		610/20	PE-dazzle-594	ICAM1(CD54)	Reverse traslocation	membrane
4		695/40	PerCPcy 5.5	CD66b	Secondary granules secretion	membrane
5		780/60	PE-Cy7	CD14	Macrophage marker	membrane
6	Violet	450/50	BV421	CXCR1 (CD181)	Traslocation/IL8 receptor	membrane
7		525/50	BV500	CD45	Leukocyte marker	membrane
8		605/12	BV605	CXCR4 (CD184)	Aging	membrane
9		710/50	BV711	TLR4 (CD284)	Pathogen sensing	membrane
10	Red	670/14	AF647	ELA	NE	intracellular
11		730/45	AF700	CD16	Phagocytosis ability	membrane
12		780/60	APC-Cy7	live/dead		membrane

Table 3 *Antibody panel used to generate data shown in* ***Figure 16****.*

TLR4, CD45 and especially CD16 (**Figure 16 c**). This latter marker is responsible for the antibody-antigen complex recognition, it is known as a target of NE and its expression is usually used to define the phagocytic ability of neutrophils.

This analysis provides the first general (but superficial) picture of the neutrophil heterogeneity in human airways. We are now improving the analysis by setting up a 22-color panel by spectral flow cytometry (Aurora Cytek) to describe in more detail precise phenotypes. Also COPD samples should be included in the study to describe yet another disease condition. The final goal is to identify potential cellular subsets which correlate with disease phenotypes and describe their relationship to the diverse factors present in the airway milieu.

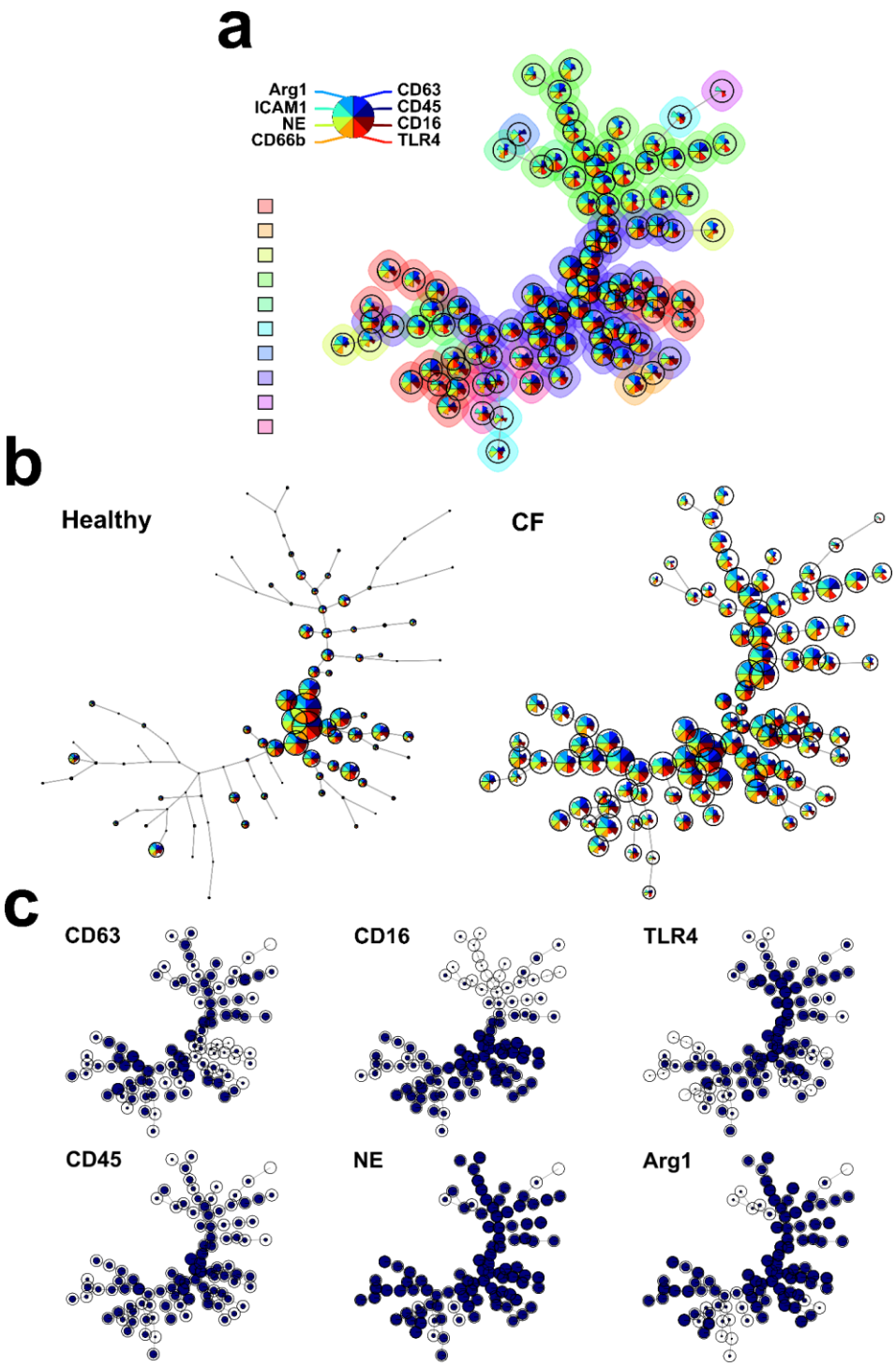

Figure 16 *FlowSOM analysis of sputum human neutrophils. a) PlotStars of the FlowSOM analysis carried out on roughly 2.5 mio cells in total. The background color indicates which metacluster each node is assigned to. The length of the marker triangle into each node indicates the level of expression for that marker. For each sputum sample (19 CF, 5 healthy) 20000 to 300000 cells were recorded. b) PlotStars showing the percentage of cells populating each node, divided by the number of healthy and CF derived cells. The size of each node is proportional to the number of cells present in the node itself. c) Plot of six out of the eight markers utilized for the clustering algorithm. The size of the circle inside each node indicates the expression of such marker for the cells included in that node. The plots are made by including both CF and healthy cells.*

3.2.5 Assessing neutrophil behavior in the blood stream

To depict a broader picture of inflammation at a systemic level, we assessed whether neutrophils behavior is reprogrammed when in the bloodstream. To become fully active and secrete their primary granule content, neutrophils evolved a protective mechanism which requires a "priming" stimulus followed by an activating trigger. We wondered if CF blood neutrophils respond differently when challenged with inflammatory cues. First, we showed that blood of CF patients contained roughly four times more neutrophils per milliliter then healthy donors (**Figure 17**), underlying an increased mobilization of neutrophils out of the bone marrow, a phenomenon known as "left shift"[21]. We then used NE secretion and activity in the supernatants and at the cell membrane as a biomarker of full-blown neutrophil activation. At resting state, we observed a moderate yet constitutive secretion of NE by purified neutrophils which was higher for healthy cells (left panel, **Figure 18 a**). Then, we incubated blood neutrophils with the priming agent TNFα, with a combination of TNFα and the stimulating peptide FMLP, to resemble the physiological neutrophilic activation, or with a combination of FMLP and Cytochalasin B, to induce the most potent activation possible. As expected, the priming agent alone was not sufficient to induce further granule release. In contrast, the other two stimulatory combinations induced CF neutrophils to secrete significantly higher amount of soluble NE (**Figure 18 a**, right panel). The stimulated cells were then analyzed by flow cytometry and their membrane-bound NE activity was measured. This analysis revealed higher surface NE activity on CF neutrophils stimulated with Cytochalasin B and FMLP (**Figure 18 b**, right panel).

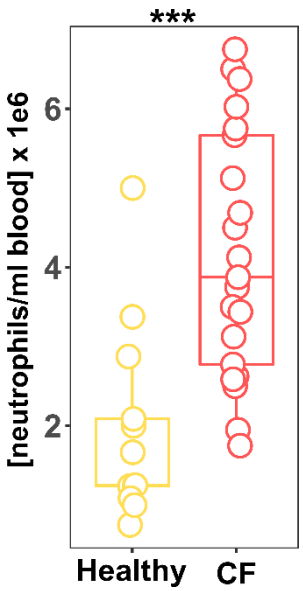

Figure 17 *Increased number of neutrophils in CF blood. Neutrophils from 20 CF and 9 healthy blood samples were purified from 8 mL of whole blood and counted. Statistics are calculated via Wilcoxon rank sum test (U test). ***: p<0.001*

We hypothesized that a systemic inflammation could shape neutrophil maturation into bone marrow and equip them with a higher NE content. Therefore, we counted the number of NE containing granules inside blood neutrophils isolated from 12 CF and 10 healthy samples (**Figure 19 a** and **b**). As a result, we observed that CF blood neutrophils contained in average of 12.8 ± 12.2 granules per cell against the 9.08 ± 8.5 in healthy ones (**Figure 19 b**). CF neutrophil granules turned out to have a slightly larger volume (24.4 ± 15.9 pixel^2) than healthy ones (17.0 ± 11.4 pixel^2) (**Figure 19 c**).

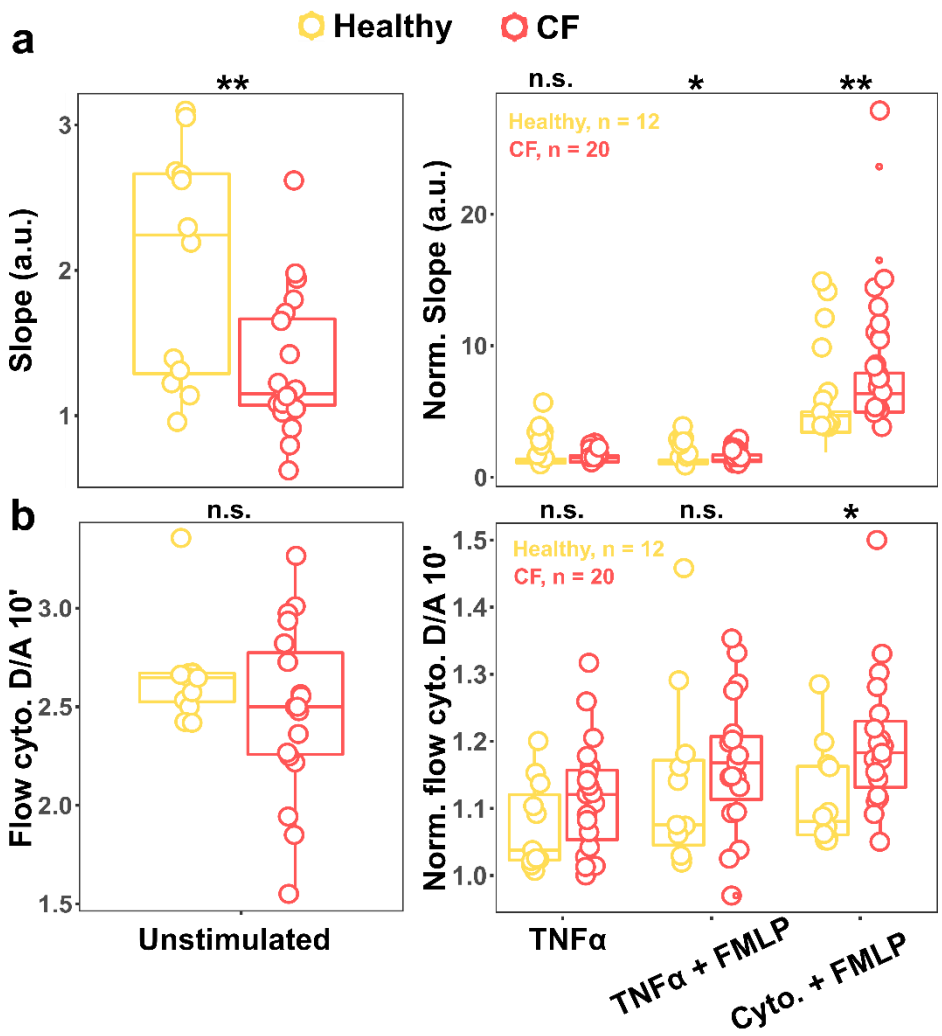

Figure 18 *Blood neutrophils response to stimuli. Soluble (a) and membrane-bound NE activity (b) measured in the supernatants and at the cell surface after treatment of blood neutrophils. Data on the right panels are shown per patient, normalized to its respective unstimulated value (shown on the left). Statistics are calculated via Wilcoxon rank sum test (U test) *: p<0.05, **: p<0.01.*

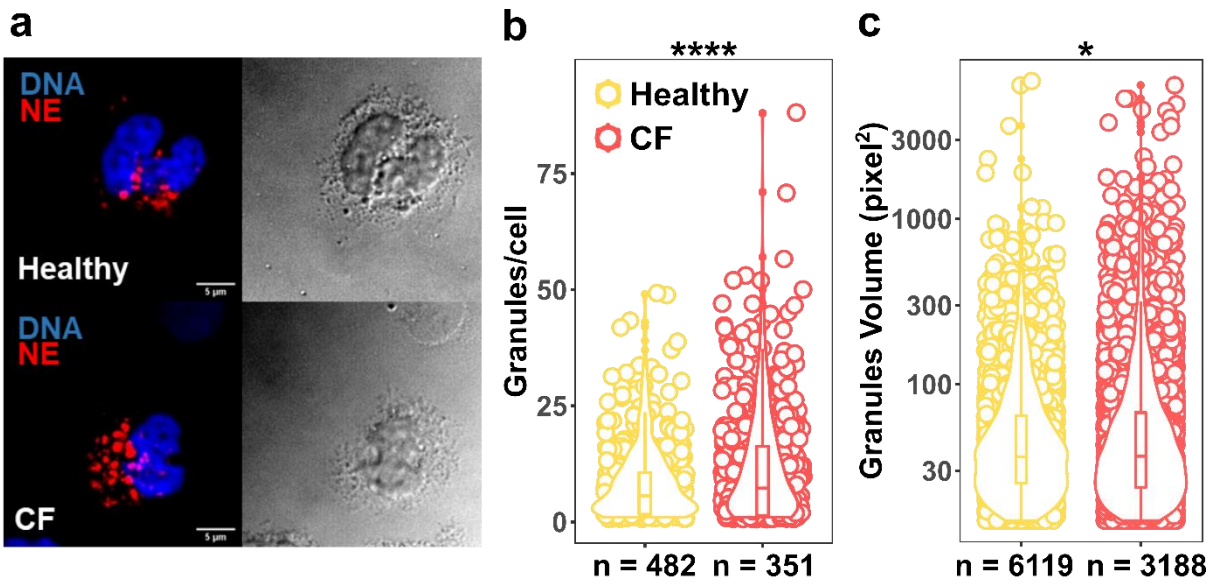

Figure 19 *CF neutrophils contain more and larger primary granules than healthy cells. a) Representative maximal projection of confocal microscopy stacks of blood neutrophils stained with a NE antibody and DAPI as nuclear marker. b) Quantification of granules contained in each neutrophil. Each data point indicates the number of granules contained per cell. c) Quantification of granule volume (indicated as pixel^2). Each point represents a granule. Statistics are calculated via Wilcoxon rank sum test (U test) *: p<0.05, ****: p<0.0001*

3.3 Part III

3.3.1 Setting up a bulk assay to detect exosome associated NE

In a major advance in 2019, exosomes and extracellular vesicles were described as pathogenic entities mainly responsible for emphysema onset and progression in COPD via the unopposed NE activity associated to their surface[77].

To provide the extracellular vesicle research field with a rapid and versatile tool, we extended the NEmo-2' spectrum of applicability and made it suitable to quantify NE activity on exosomes.

We started from the purification of extracellular vesicles from CF and healthy sputum via the Total Exosome Isolation (TEI) Reagent (Invitrogen™) (**Figure 20 a**). The presence of correctly sized particles (50-250 nm) and shape (cup-shaped after drying) was confirmed by transmission electron microscopy (TEM) (**Figure 20 b**). In addition to being a neutrophil activation status indicator, CD63 is a transmembrane tetraspanin protein routinely used as exosomal marker[116]. Western blot analysis demonstrated that CF exosomes carried NE at their surface in considerably higher amount compared to healthy ones, also when NE amount was normalized to CD63 (**Figure 20 b**).

To ensure a complete and specific purification of exosomes from human sputum, we coupled the precipitation mediated by the TEI with an immune capture of particles to CD63-derivatized magnetic beads (**Figure 20 c**). Then, beads loaded with exosomes were carefully washed up to five times to remove any debris and remnants of free NE. The successful removal of the unbound fraction was confirmed by the absence of NE activity in the wash supernatants (data not shown).

Treatment of nanosized particles with a nonionic detergent represents a crucial control[117]. The detergent preferentially dissolves lipid enclosed particles and not immune complexes or non-specific aggregates. Therefore, Triton X-100 treatment of immunocaptured particles should solubilize exosomes and transfer NE activity from the bead to the supernatant fraction. After carefully washing the bead-exosome complexes and treating them with the detergent, we observed an almost complete loss in NE activity in the bead fraction and reappearance of such signal in the supernatant fraction (**Figure 20 c**).

Finally, we excluded the possibility that elastase was non-specifically thethered to beads by incubating the magnetic beads with different NE concentrations. In fact, no activity was detected on beads after they were treated identically to the exosome-beads complex.

Next, we explored whether exosomes acquired NE at their surface in the airways or if such association happened already in the bloodstream. This assay showed that neither CF nor healthy blood exosomes carried active NE at their surface, while CF sputum exosomes possessed an “activated” phenotype (**Figure 20 d**).

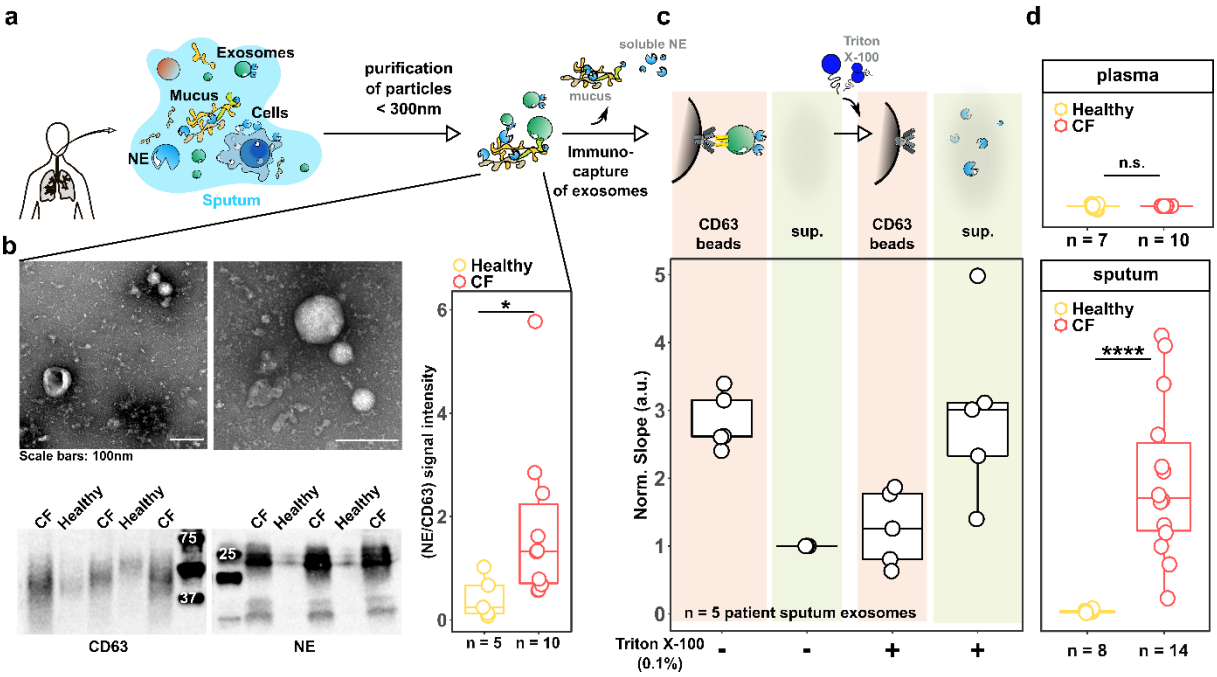

Figure 20 *Measuring NE activity on immunocaptured CD63⁺ sputum exosomes. a) Schematic depiction of the exosome purification strategy. b) Top: Representative transmission electron microscopy images of exosomes isolated from human sputum via Thermo Fisher Isolation Kit. Bottom and right: representative Western blot for CD63 and neutrophil elastase (bottom) and the quantification of their ratio (right) for 10 CF and 5 healthy exosome isolates. c) Slopes indicating free NE activity obtained from the incubation of immunocaptured exosomes and their supernatant after four washing steps and samples treated with Triton X-100 (0.1%) for 15 min. N = 5 exosome samples isolated from 5 different CF patients. d) Slopes indicating free NE activity obtained from the linear regression of donor/acceptor increase over time of plasma (top) and sputum (bottom) exosomes incubated with NEmo-2.*

3.3.2 A single nanoparticle assay based on flow cytometry

We worked on developing a cytometric assay that would permit for a rapid, “purification free” and single-nanoparticle based evaluation of vescicles number, antigen repertoire and NE activity in human samples. First, our flow cytometer needed to be calibrated to identify and gate particles in the range of 100-500 nm (**Figure 21 a**). Commercial polystiren or glass beads

differ from exosomes in terms of refractive index, and their use as standard reference is not advised[118].

Therefore, we turned to niosomes, lipid-enclosed particles developed by Lozano-Andrès et al.[118], designed to resemble exosomes features and physical properties. By means of such FITC-beads, we could set proper threshold and voltage settings to properly discriminate 100, 200 and 500 nm particles (**Figure 21 a**).

Once the machine was calibrated, we proceeded wiht the isolation of sputum exosomes via TEI which were stained with CD63-FITC or CD63-AF647 and their respective IgG controls. In both positive stainings, a clear population of events reflecting the expected particle size were

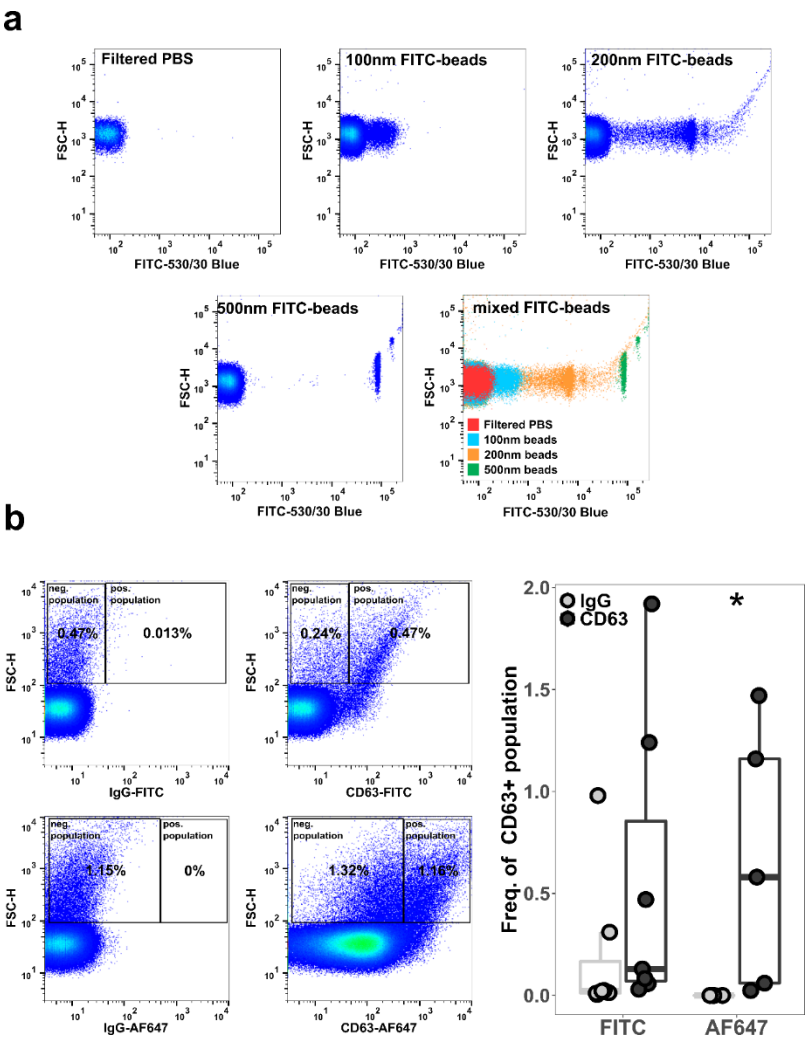

Figure 21 *Tuning a flow cytometer to "see" nanoparticles. a) Representative FSC-H vs. FITC-530/30Blue plots of differently sized (100,200 and 500 nm) niosomes. b) Dotplots of sputum exosomes stained with either CD63-FITC or CD63-AF647(center panel) and respective IgG controls (left panel). Boxplots in the right panel indicate the frequency of the positive populations shown in the dotplots. N = 5-7 sputum exosomes per group. Statistics were performed using Wilcoxon rank sum test (U test), *: p<0.05.*

identified (**Figure 21 b,** central panel). In both cases, no or very few stained events were detected when samples were incubated with the IgG control (**Figure 21 b**, left panel).

Once again, treatment of sputum exosomes with triton X-100 resulted in a 10.5 fold decrease in the number of CD63+ events, confirming that the identified cloud consists of lipid-enclosed nanoparlticles (**Figure 22 a**).

Finally, by analysing CF sputum exosomes incubated with the FRET reporter NEmo-2 via flow cytometry a ratiometric measurement of NE activity on airways-derived nanopartcles was achieved (**Figure 22 b**).

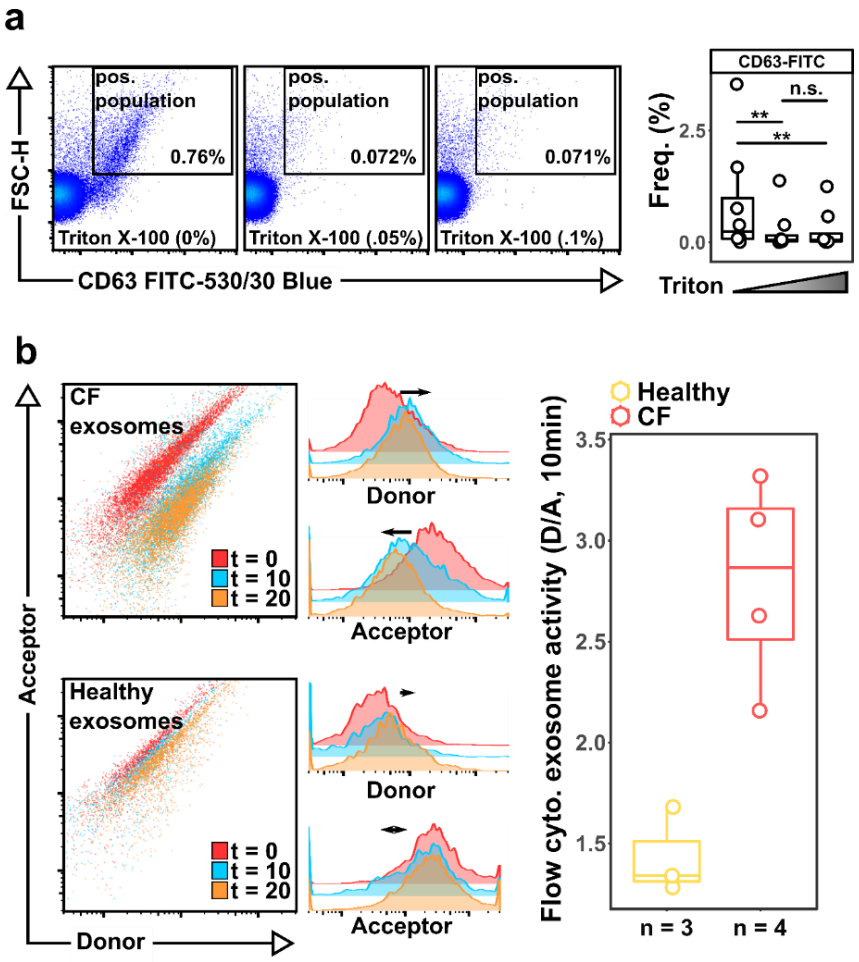

Figure 22 *Exosome FRET flow cytometry. a) Representative FSC-H vs. 530/30 Blue (FITC) plots (left side) and population quantification (right side) of exosomes (gated positive population) treated with two different concentration of Triton X-100 (0.05 and 0.1%) for 15 min. N = 7 human sputa (4 CF and 3 healthy). b) (left panel) Time dependent donor/acceptor increase on CF (top) and healthy (lower) exosomes gated as CD63 positive nanoparticles. (Central panel) Histograms showing the time dependent change of the signal of the reporter NEmo-2 on exosomes. (Right panel) Quantification of the measured donor/acceptor increase after 10 min incubation with nemo-2 on 3 healthy and 4 CF exosomes. Statistics were performed using Wilcoxon rank sum test (U test).*

3.3.3 Exosomes export active proteolytic enzyme to the surface of epithelial cells

Exosomes might act as carriers of active NE to the surface of surrounding cells. Upon such transfer, NE might cleave protease activated receptors (PARs) and start inflammatory cascades on target cells[119]. To test this hypothesis, we purified exosomes from human sputum as CD63, CD9 and CD81 positive particles. We next supplemented identical amounts (3 µg / mL) of CF and healthy exosomes to human bronchial epithelial cells (16HBE14o-) stained with NEmo-2 and recorded the increase of donor/acceptor ratio at the plasma membrane by confocal microscopy (**Figure 23 a**). CF exosomes transferred significantly higher amounts of active NE to the cell surface of human bronchial cells compared to healthy exosomes (**Figure 23 b**). Confirming that the transfer was exosome-mediated, Triton X-100 treatment abolished the signal increase. Moreover, incubation of CF exosomes with A1AT and Sivelestat proved that the effect was NE-specific (**Figure 23 b**).

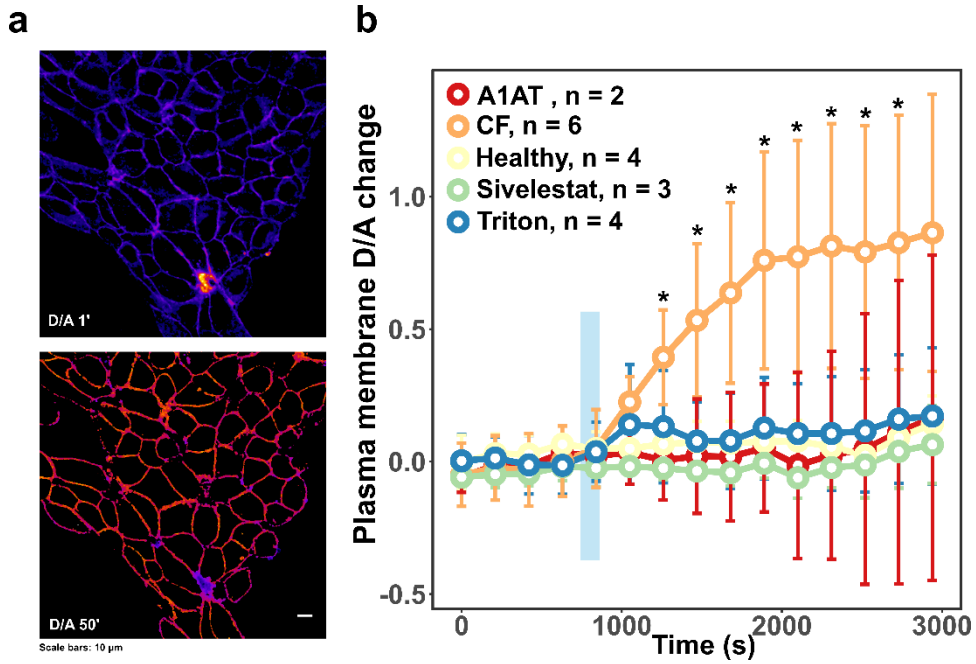

Figure 23 *Membrane-bound NE activity on human bronchial epithelial cells. a) Representative confocal microscopy images showing the donor/acceptor ratio at plasma membrane of HBE cells after 1 min (top image) and 50 min (bottom panel) incubation with 0.3 µg/mL CF exosomes purified from patient sputum. b) Mock subtracted quantification of donor/acceptor ratio change on the surface of cells incubated with healthy or CF exosome isolates. For four CF samples, exosomes where treated with Triton X-100 (0.1%) for 15 min at RT, and then incubated on HBE cells. Additional 3 and 2 CF samples were treated with the NE inhibitors Sivelestat and A1AT for 15 min at RT, respectively. Roughly 400 cells were measured. Statistics performed using Wilcoxon rank sum test (U test), *: p<0.05.*

3.3.4 General strategies for localizing FRET probes to DNA

Many inflammatory processes such as atherosclerosis and gout are mediated by proteases bound to extracellular DNA[70]. However, the study of such enzymes in their DNA-bound form has been challenging due to the lack of proper tools to visualize their activity.

We hypothesized that by redesigning the structure of localized FRET reporters, we could address our probes to extracellular nucleic acids, and therefore provide a useful reporter capable of shedding light on DNA-bound proteases pathobiology (**Figure 24**). The successful targeting to DNA can be achieved via coupling DNA-binding agents, short domains like zinc-fingers or oligonucleotides to the probe of interest. The resulting compound would therefore tether to nucleic acids. First, we chose to add an acridine moiety to our probes. Acridines are known intercalating compounds and their availability as 9-acridinecarboxylic acid makes them directly suitable for SPPS. However, acridine-containing FRET probes did not possess satisfactory DNA localization and therefore such design was rapidly set aside. Second, we were inspired by SiR-Hoechst, a widely used DNA stain agent that finds broad application for live cell nanoscopy applications[120]. SiR-Hoechst binds DNA with a K_d of ~8 µM and is composed of a far-red silicon-rhodamine dye (SiR) directly coupled to the bisbenzimide core of the Hoechst dye. The employment of such DNA minor groove binder allowed us to successfully monitor NE and CG activity on extracellular DNA and neutrophil extracellular traps (NETs).

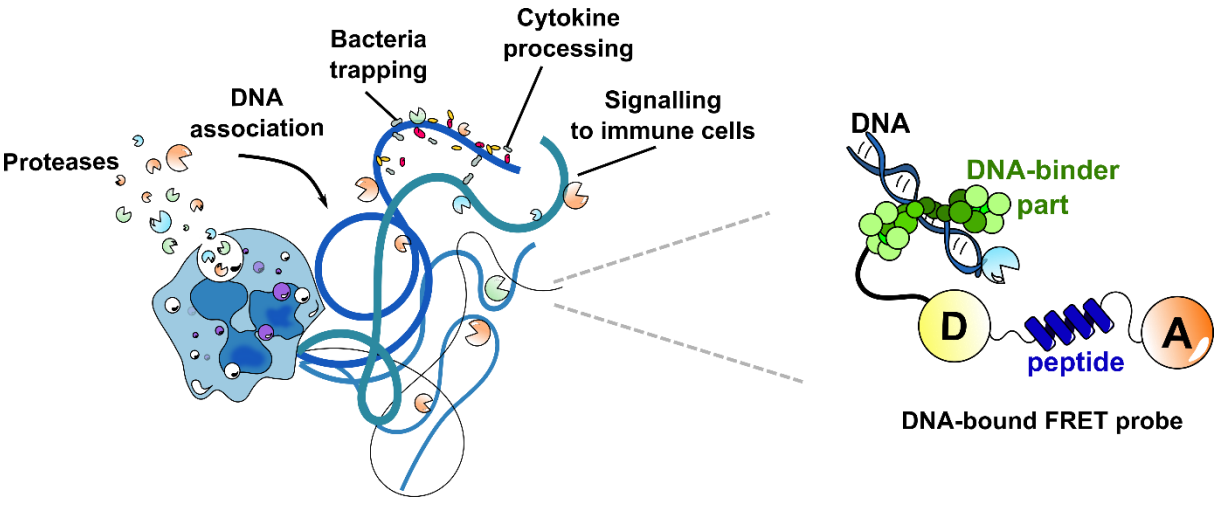

Figure 24 *Overall representation of NETs and DNA-bound probes. Neutrophil serine proteases NE and CG bind to extracellular DNA due to electrostatic interactions and participates to innate immunity. By targeting FRET reporters to the nucleic acid we visualize and quantify DNA-bound extracellular protease activity.*

3.3.5 H-NE and H-CG: bisbenzimide-containing FRET probes synthesis and characterization

Our strategy to target small-molecule probes to DNA was to anchor the minor groove binder Hoechst 33258 to the FRET probe. We imagined such anchoring to be mediated via a copper-catalyzed azide-alkyne Huisgen cycloaddition since click chemistry possesses great orthogonality over the other reactions performed during the SPPS routine. First, the free base of the commercial fluorophore Hoechst 33258 (compound **2**) was obtained. Then, compound **3** (Hoechst-azide) was derived from the alkylation of compound **2** by a bromide-PEG-azide (**Figure 25 a**) (see appendix for complete chemical characterization, NMR and high resolution mass spectrometry). Hoechst-azide was then clicked on the propargylglicine connecting the PEG spacer and the energy donor via copper-catalyzed click chemistry reaction to generate the probes H-CG and H-NE respectively (**Figure 25 b** and **Figure 26 a**). In addition to the H-NE and H-CG probes (compound **4**), also the precursor alkyne containing probes were cleaved off the resin to generate the control probes A-NE and A-CG (**Figure 26 a**).

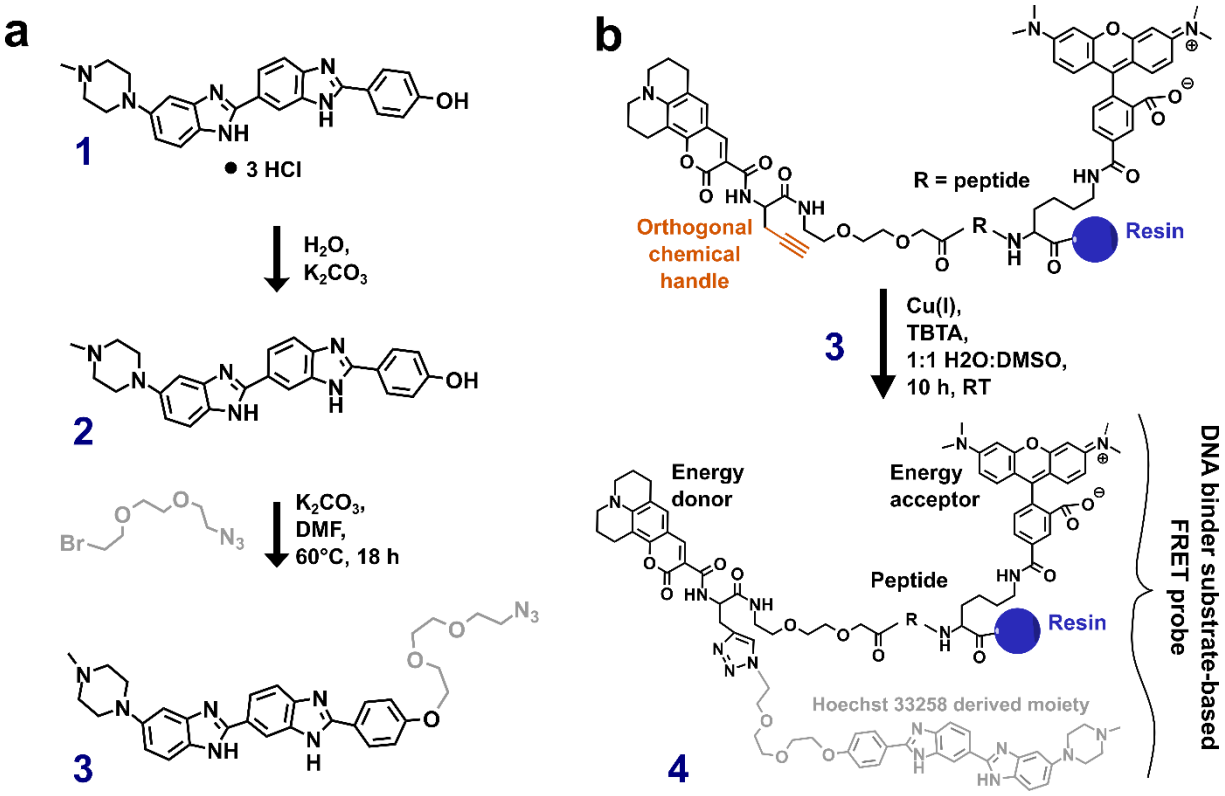

Figure 25 *Scheme of synthetic route for DNA-binding reporters. a) Commercial Hoechst 33258 hydrochloride was precipitated in a K_2CO_3 solution. Bromide-PEG-Azide was then added to the compound **2** and the compound **3** (Hoechst-azide) was obtained. b) Copper-catalyzed click reaction was performed on resin-bound peptides terminating with a propargylglicine to obtain the desired final product. The non-clicked peptides were used to generate the control probes A-NE and A-CG (**Figure 26 a**).*

To evaluate the performance of H-NE and H-CG we determined their emission spectra in aqueous solution and observed a rather low acceptor sensitized emission, indicating that the acceptor is serving mainly as a quencher (**Figure 26 a**, top panel). When the enzyme was added, a strong increase in the donor emission was recorded, indicating loss of FRET and cleavage of the reporters (**Figure 26 a**, top panel).

H-CG reporter is meant to monitor CG activity since it bears the same peptide we employed for mSAM, while H-NE reports on NE (the peptide is a neutrophil elastase substrate developed and characterized by Korkmaz et al.[87], also shown in **Figure 2 d**). When tested against NE, CG, P3, chymase, MMP-12 and cathepsin S, H-NE showed high specificity towards its target protease (**Figure 26 b**). Also H-CG showed optimal performance in terms of specificity towards NE and PR3 (**Figure 26 c**).

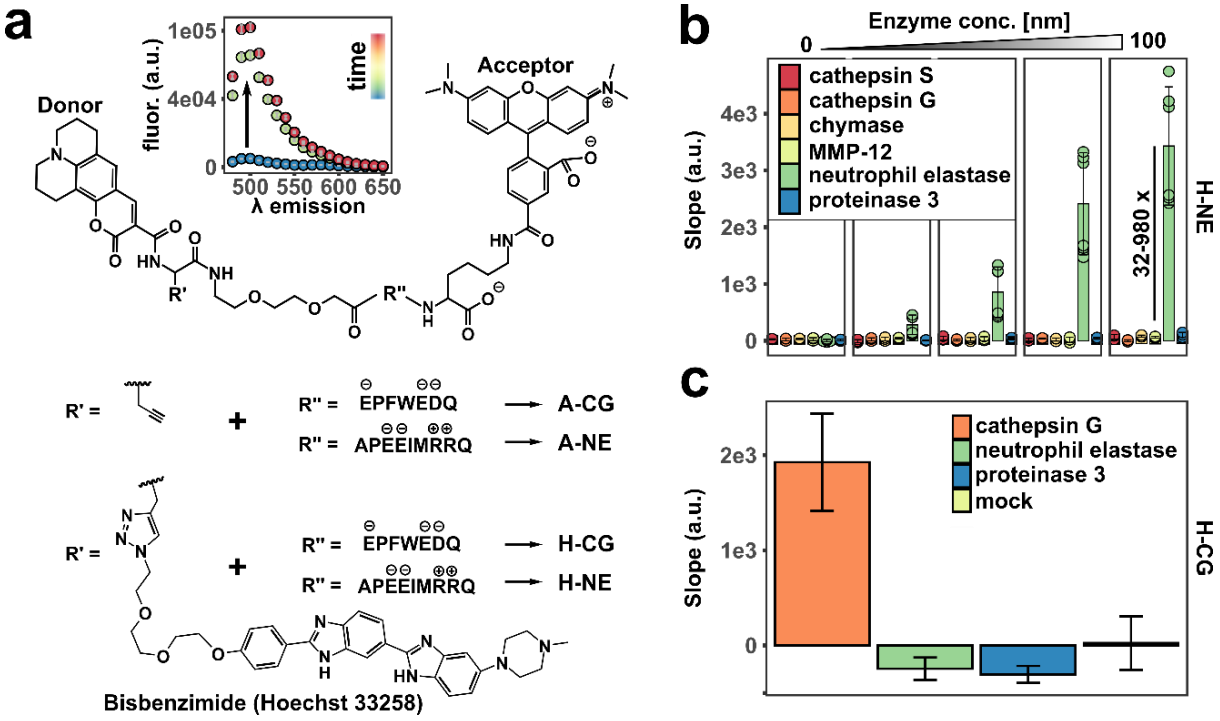

Figure 26 *Structure, cleavage and performance of DNA-bound reporters H-CG and H-NE. a) Scheme of probes with chemical structures of the control reporters A-CG/A-NE and the corresponding DNA minor groove binder probes H-CG and H-NE. Top: representative H-NE fluorescence signal increase at 1, 30 and 60 min after addition of neutrophil elastase (NE). Data are shown as mean ± standard deviation, n = 3 technical replicates. b) Bar graphs showing cleavage rates calculated from linear regression slopes of H-NE [2 µm] incubated with 5 different concentrations of different proteases for 60 min. Data are shown as mean ± standard deviation, n = 3-6 technical replicates. Enzyme concentrations: 0, 1.56, 6.25, 25, 100 µm. MMP-12: matrix metalloproteinase-12. c) Bar graphs showing cleavage rates calculated from linear regression slopes of H-CG [2 µm] incubated with [20nM] of CG, NE or PR3 for 20 min.*

3.3.6 H-NE DNA localization

To assess the property of H-NE as a DNA dye, we purified neutrophils from whole blood, which were then fixed and incubated with 2 µM of the reporter. A clear nuclear staining appeared only inside neutrophils which had been previously permeabilized (**Figure 27**, left side). This result indicated that H-NE did not penetrate live-cells. The permeabilized neutrophils resulted to be homogenously and brightly stained 30 min after addition of H-NE. Next, we compared H-NE DNA binding specificity with the probe A-NE. The latter compound served as a negative control due to the absence of the Hoechst moiety on the terminal amino acid. In fact, no specific nuclear signal was detected when blood neutrophils were incubated with 2 µM of A-NE. Only a diffused and dim signal was observed inside permeabilized neutrophils, possibly due to the non-specific binding of A-NE to organelles and other "sticky" cellular structures (**Figure 27**, right side).

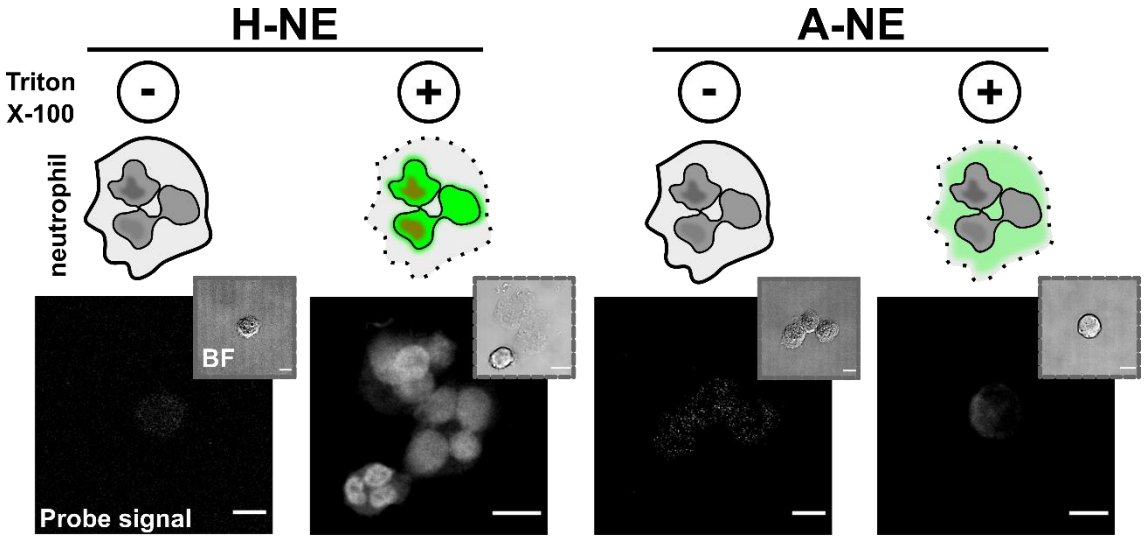

Figure 27 *H-NE does not enter live neutrophils and stains DNA via its Hoechst moiety. Purified blood neutrophils were fixed with PFA 4% and permeabilized (0.1% Triton X-100 for 10 min) or left untreated. Then cells were incubated with either H-NE and A-NE. (bottom) representative confocal microscopy images. Experiments were performed in duplicate and cells derived from two healthy blood donors. Scale bars: 5 µm.*

The goal of our set of probes was to light up protease activity on extracellular DNA such as the one secreted by neutrophils in response to inflammation in the form of neutrophil extracellular traps. Therefore, the DNA binding properties of H-NE were assessed on extracellular DNA secreted by blood neutrophils. NETs formation was recently described to be a novel cellular death pathway, molecularly distinct from apoptosis and necrosis[67]. Phorbol myristate acetate (PMA) is a plant derived tumorigenic compound[121]. PMA is a strong activator of protein kinase

C which induces ROS- and NADPH- dependent pathways culminating in NETosis[122]. Therefore, PMA-induced blood neutrophils are a widely used model to study extracellular DNA properties and biology. We purified blood neutrophils (purity > 95 %) from two healthy donors and stimulated cells with PMA. H-NE painted the nuclear DNA which is released after nucleus and plasma membrane rupture following NETosis (**Figure 28 a**). Once again, we observed that H-NE did not penetrate intact cells (white arrows in **Figure 28 a**). Thin DNA filaments less than 1 µm in diameter were also clearly distinguishable in the reporter channel (**Figure 28 a**, magnified images). A further proof of the DNA localization of H-NE came from the fluorescence line profile analysis of NETs incubated with the commercial DNA stain agent Draq5 in the presence of H-NE (**Figure 28 b**). The profiles showed almost complete overlap between the two channels indicating high colocalization (**Figure 28 c**). Accordingly, we calculated Pearson correlation coefficient (0.76 ± 0.17) and area overlap (0.94 ± 0.07) between Draq5 and H-NE channels on 199 NETs. When incubated with the control probe A-NE which does not possess any DNA-affine part, only aspecific signal was detected (Pearson: - 0.008 ± 0.21, Overlap: 0.51 ± 0.20, n = 176) (**Figure 28 d**). The probe was also successfully employed in live cell imaging to stain neutrophils nuclei over the course of NETosis. During live cell imaging, we observed the appearance of reporter signal in the nucleus only right after plasma membrane rupture was observed (**Figure 28 e**).

As a proof of concept of H-NE ability to reveal NET-associated enzymatic activity, we incubated blood neutrophil NETs with increasing concentrations of NE (**Figure 28 f**). After carefully washing the unbound protease, H-NE was added for 30 minutes and the signal was recorded via confocal microscopy. A concentration-dependent increase in donor/acceptor ratio was observed (**Figure 28 g**). Importantly, the measured ratio increase was due to a fluorescence increase in the donor and a simultaneous decrease in the acceptor channel (**Figure 28 h**).

We concluded that the attachment of bisbenzimide derivatives to substrate-based FRET probes successfully targeted ligands to DNA and permitted the generation of probes for the visualization of proteases in their DNA-bound form.

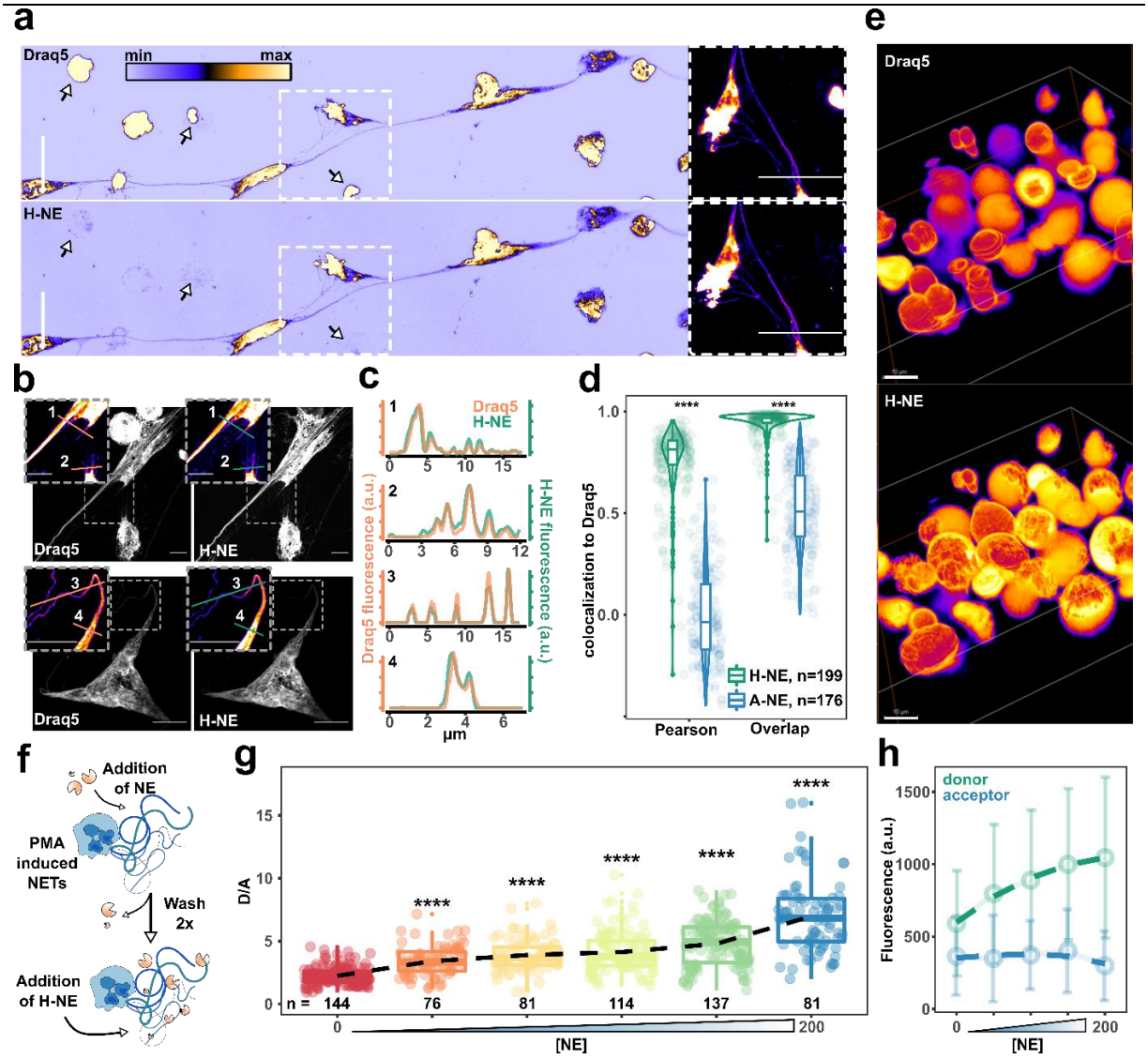

Figure 28 *H-NE paints neutrophil extracellular traps DNA and detects NE activity in its DNA-bound state. a) (Left panel) Representative maximum intensity Z-projection of a confocal tilescan of fixed neutrophils after PMA stimulation ([2 µM] for 2.5 hours) and incubated with the commercial DNA stain (Draq5) and H-NE [2 µm] for 30 min. Arrows point to cells not having undergone NETosis and stained by Draq5 only. Scale bars: 30 µm, LUT: ICA. (Right panel) Magnification and 90° rotation of the selected area showing staining of decompacted DNA filaments by Draq5 (top) and H-NE (lower). Scale bars: 30 µm, LUT: fire. b) Representative confocal images of fixed PMA-stimulated neutrophils incubated with Draq5 and H-NE. The magnified area shows lines used to generate the data analyzed in (c). Scale bars: 10 µm. LUT: grays and fire (magnified area). c) Line profile analysis of the four selections shown in (b, magnified areas) for Draq5 (orange) and H-NE (green) channels. d) Violin and boxplot showing Pearson correlation coefficient and area overlap between Draq5 and H-NE (Pearson: 0.76 ± 0.17, overlap: 0.94 ± 0.07, n = 199) or Draq5 and the control probe A-NE (Pearson: - 0.008 ± 0.21, Overlap: 0.51 ± 0.20, n = 176). NETs were generated from blood of two healthy donors and technical duplicates were imaged. Statistics are calculated via Wilcoxon rank-sum test. ****: p<0.0001. e) Confocal Z-stack showing PMA-stimulated live neutrophils undergoing NETosis and incubated with Draq5 (top panel) and H-NE [2 µm] (lower panel). Scale bars: 10 µm. LUT: fire. f) Schematic of experiments performed in g) and h). g) Boxplots showing measured donor/acceptor ratio on extracellular DNA after incubation for 30 min of 5 NE concentrations [1,10,20,100,200 nM]. The "0" indicates NETs incubated with Sivelestat [100 µM] for 30 min as a negative control. h) Line plots of donor increase and acceptor decrease measured in g.*

3.3.7 NE but not CG is proteolytically active in its DNA-bound form

The general opinion regarding NETs bound proteases is that they serve as a reservoir of active proteases which are kept inactive as a consequence of nucleic acid binding[123]. However, these observations originated from experiments carried out via a fluorimetric readout on purified DNA and suffered from lack of a direct measurement and spatial localization.

Therefore, we challenged this view by applying H-NE and H-CG to NETs derived from four and two different healthy donor blood samples, respectively. Surprisingly, we could detect a time-dependent and inhibitor-sensitive signal increase on such DNA web-like structures incubated with H-NE over the course of 120 min (**Figure 29 a** and **b**). This suggests that DNA-bound NE

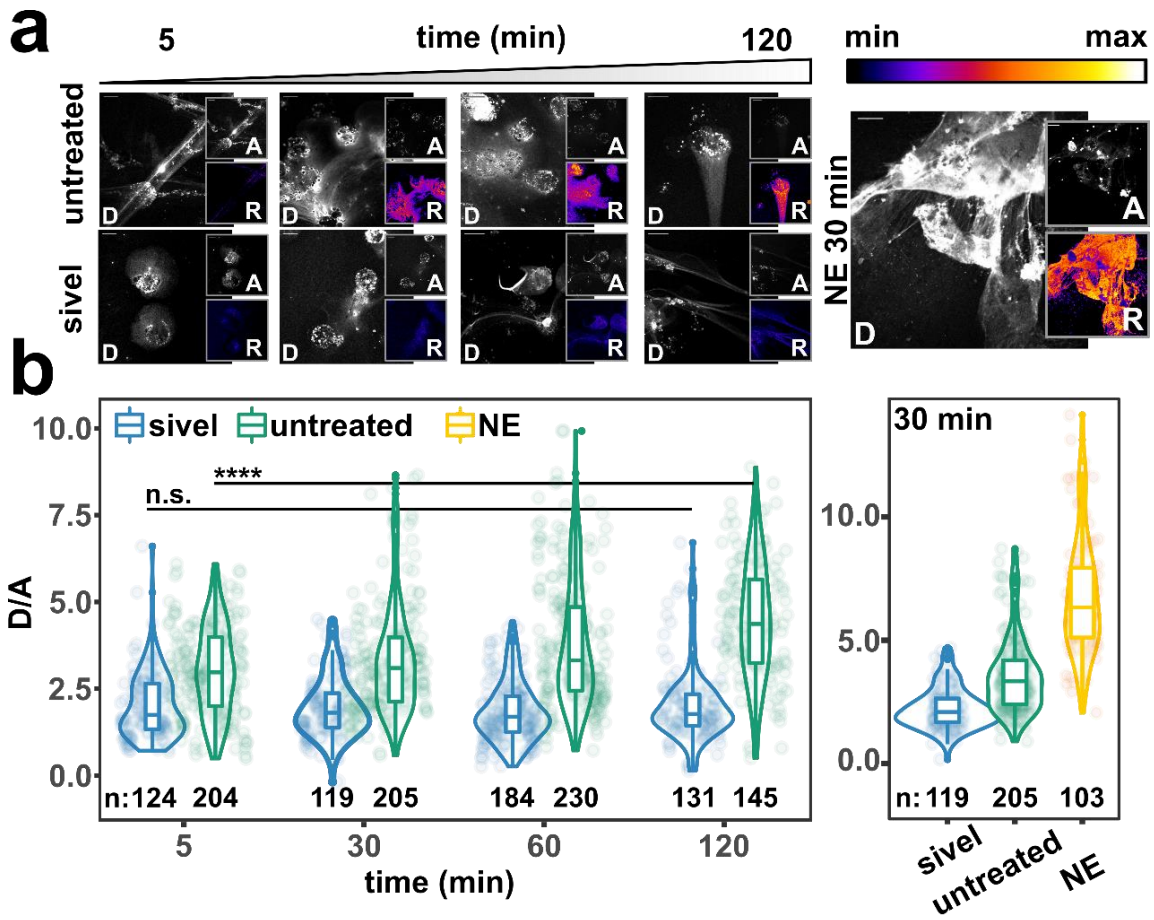

Figure 29 *DNA-bound NE retains its hydrolytic ability. a) Representative confocal images of blood NETs incubated with H-NE for different time periods (5, 30, 60 ,120 min). D: donor channel, A: acceptor channel, R: donor/acceptor ratio channel. Right panel: confocal image showing blood NETs incubated with H-NE after addition of [200 nm] of active NE as a positive control. Scale bars: 10µm, LUT: grays and fire (ratio images). b) Violin and boxplots showing the quantification of NE activity on NETs derived from blood neutrophils isolated from 4 healthy donors. Sivel: cells were preincubated with Sivelestat [100 µm] for 10 min prior of H-NE addition. NE: NETs were preincubated with active NE [200 nm] for 10 min prior of H-NE addition (shown in the right panel). Statistics are calculated via Wilcoxon rank-sum test. ****: p<0.0001.*

retains its activity to cleave substrates in close proximity and has functional implications regarding the roles of the protease in the DNA bound form. Conversely, H-CG did not reveal any signal increase due to cathepsin G activity after incubation with blood neutrophils NETs (**Figure 30**, left panel). The lack of donor/acceptor ratio increase was not due to lack of reporter sensitivity, since the incubation of blood NETs with exogenous CG prior to H-CG addition could generate a strong signal increase (**Figure 30**, right panel). Therefore, in contrast to its membrane-bound form, DNA-bound CG seems to be differently regulated or inhibited. Taken together, these results highlight the importance to finely dissect protease activity in all their forms and subcellular locations since the understanding of context dependence will allow for more tailored anti-inflammatory treatments.

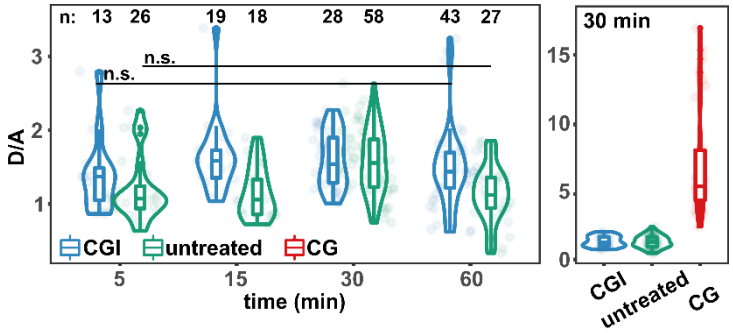

Figure 30 *DNA-bound CG does not retain its hydrolytic ability. The figure shows violin and boxplots showing the quantification of CG activity on NETs derived from blood neutrophils isolated from healthy donors. CGI: cells were preincubated with cathepsin G inhibitor I [100 µm] for 10 min prior of H-CG addition. CG: NETs were preincubated with active CG [200 nm] for 10 min prior of H-CG addition (shown in the right panel). Statistics are calculated via Wilcoxon rank-sum test.*

3.3.8 Application of H-NE to human sputum

The value of H-NE as a translational tool highly depends on its ability to monitor DNA-bound NE on extracellular DNA derived from CF and COPD airways. The presence of high amounts of free nucleic acid coming from necrotic and apoptotic cells as well as NETotic neutrophils is well documented[25,69] and can be observed in **Figure 31 a**.

H-NE successfully stained large DNA condensates filling up the CF sputum (**Figure 31 b**). In addition, we could quantify NE activity on sputum DNA, which could be inhibited by pretreatment with a specific inhibitor, the small molecule Sivelestat (**Figure 31 c** and **d**). In **Figure 31 c**, left side, the semi-decondensed DNA of a neutrophil nucleus in the process of NETosis can be observed. The NE activity seemed to be localized in the condensed nuclear region.

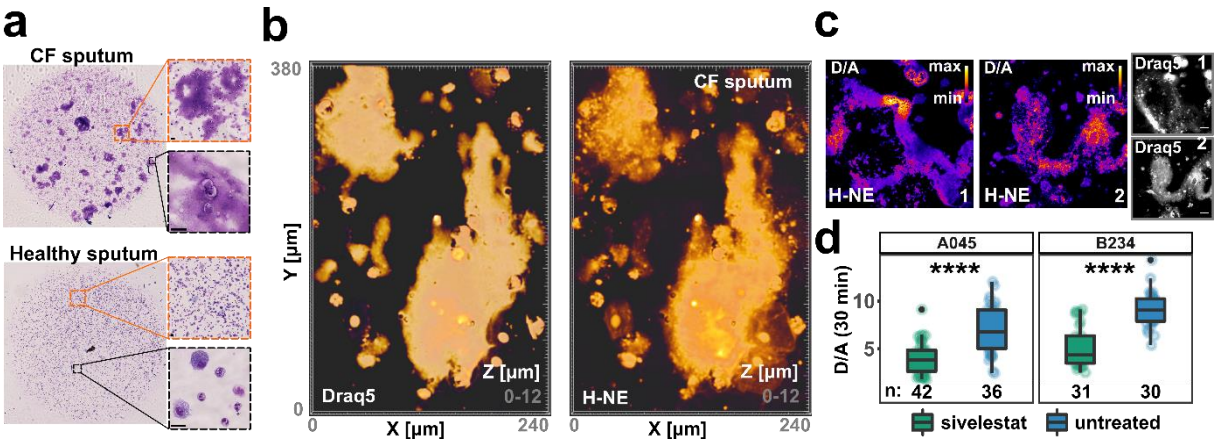

Figure 31 *H-NE stains large DNA condensates and reveals high NE activity on CF derived extracellular DNA. a) H&E cytospins of healthy (left) and CF (right) sputum depicting different amount of extracellular DNA content. Magnified area: segmented nuclei of healthy neutrophils (left) and decondensed and potentially netting nuclei of CF neutrophils(right). b) Confocal Z-stack of CF sputum stained with Draq5 (left) and H-NE (right). Area of the larger orange region: ~ 7000 µm^2 LUT: fire. c) Representative confocal images showing measured NE activity on extracellular DNA present in CF sputum. LUT: fire and grays (Draq5 images). Scale bars: 10 µm. d) Boxplots showing quantification of NE activity on CF sputum extracellular DNA 30 min after addition of H-NE, incubated with or without Sivelestat [100 µm] prior to H-NE addition for 10 min. Patient A045: Sivelestat treated (D/A= 4.00 ± 1.61), untreated (6.87 ± 2.46). Patient B234: Sivelestat treated (D/A= 5.16 ± 2.08), untreated (9.09 ± 1.85). Data are shown as single DNA structure derived from 2 CF patients. Statistics were calculated via Wilcoxon rank sum test. ****: p < 0.0001*

3.3.9 DNA-bound NE activity in complex systems

Finally, the simultaneous monitoring of DNA spatial information and enzymatic activity bears the potential to generate a comprehensive picture of extracellular DNA mediated inflammatory processes in the context of large anatomical structures such as liver, lungs and veins. We chose β-ENaC-Tg (also indicated as Scnnb1-Tg) mice as a model, because its airways are often clogged by mucus plugs[25,47]. Trapped inside the mucin webs, immune cells and large quantities of extracellular DNA can be found.

We fixed, embedded and cut mice lungs into 5 µm serial transversal lung slices (**Figure 32 a**). H-NE stained clearly the DNA contained in the mouse airways at more than satisfactory resolution, making it possible to quantify NE activity at the single-cell level (**Figure 32 b** and **c**). Specifically, we could assess NE activity inside the nuclei of neutrophils, monocytes, epithelium and on mucus-embedded free DNA of lung slices incubated solely with the probe or in combination with the negative control Sivelestat (**Figure 32 d**). We observed higher NE activity in neutrophils and on free DNA compared to the Sivelestat control. As expected, no activity was found inside the nucleus of monocytes and epithelial cells (**Figure 32 d**).

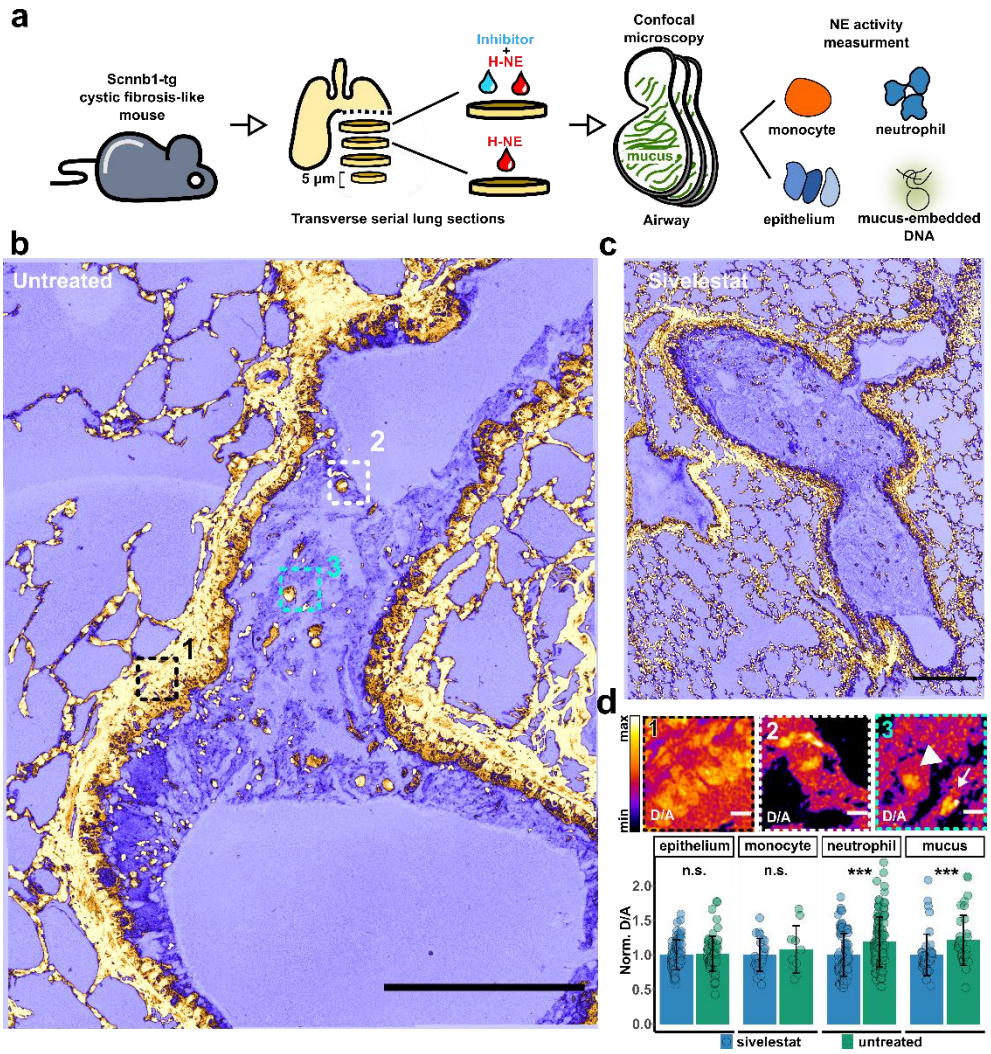

Figure 32 *H-NE application in* ex vivo *mouse lung slices. a) 5 µm transverse serial lung sections of CF-like Scnnb1-tg mice were incubated for 3 hours with either H-NE alone or H-NE and Sivelestat [1mM]. Three dimensional tilescans of entire airways were then acquired via confocal microscopy and NE activity inside the nuclei and on free floating extracellular DNA was calculated. b, c) Maximal projections of confocal tilescan images of PFA-fixed and paraffin-embedded 5 µm thick lung slices of Scnn1b-Tg mice stained with H-NE [2 µM] (b) and treated with Sivelestat [1mM] for 30min prior to HNE staining for 3 hours (c). d) Representative confocal images showing donor/acceptor ratio of epithelial cells (1), mucus-embedded DNA (2), neutrophil (arrow) and monocyte (arrowhead) (3) and respective NE activity quantification (lower panel in d). Scale bars: 200 µm (b, c), 10 µm (d). Statistics were calculated using Wilcoxon rank sum test. ***: p<0.001.*

4. Discussion

Function and dysfunction of the innate immune system is central for the disease progression in chronic airway inflammation as during CF and COPD lung diseases. Neutrophils are recognized as primary actors in such context and they exert their functionalities via the secretion of eclectic effectors such as proteases, myeloperoxidase and cytokines. The past decade has seen a renewed interest in the study of proteases since they are valuable biomarkers, their involvement in many pro- and anti-inflammatory pathways makes them attractive drug targets, and they are handles for creative scientific exploration from a chemical biology standpoint. The ultimate goal of this research project was to equip the biomedical research with new assays and tools to explore uncharted NSPs activity and relationships.

4.1 Part I

4.1.1 CG activity is elevated in airway inflammation

Neutrophil elastase is widely considered to be a leading player in the onset and progression of CF and COPD lung diseases[56,124]. Recently, the use of this enzyme has considerably risen as disease-status predictor[43]. Moreover, several imaging approaches were established to measure and localize elastase activity, from simple chromogenic substrates to MRI suitable probes[95]. Despite NE utility as a diagnostic and prognostic tool, clinical candidate NE inhibitors such as Sivelestat and AZD9668 always resulted in poor therapeutic outcome and unaltered tissue disruption[42,48]. On one hand, such discrepancies could be resolved with a more appropriate patient cohorts' design: NE inhibitors were administered to adult CF patients, which feature prominent and non-resolving inflammation. In contrast, the administration of anti-inflammatory agents to CF children and adolescents may drown inflammation in its earliest stages and reach the desired clinical endpoints (i.e. reduced neutrophilia, IL-8 secretion, lung function). On the other hand, an improved understanding of protease biology in airway inflammation seems to be central to designing novel inhibitors. In fact, new evidence suggests that the concerted action of the three NSPs cause more severe lung damage than NE alone. In mice, the simultaneous knock-out of the NSPs has the effect to reduce the concentration of active proteases such as MMP-9 and MMP-12 which in turn activate pro-inflammatory cytokines[125]. Moreover, NSP interplay causes higher ECM destruction and remodeling, measured as increased wall-to-wall distances of alveoli (L_m) compared to NE deficient mice[125].

Importantly, although NE and CG double knockout mice are more protected from smoke-derived lung damage, they also feature more susceptibility to *Streptococcus pneumoniae* and mycobacterial infections[126]. Such duality highlights that i) NSPs play multi-faceted roles in innate immunity, ii) the bottleneck to unravel such complexity lays in the availability of tools and assays to study mediators of inflammation in patients and animal models.

The first attempts to develop CG specific substrates date back to the early eighties[127]. Since then, several groups focused on developing more and more specific chromogenic reporters. Recently, Attucci et al. designed and optimized the substrate sequence EPFWEDQ, (N- to C-terminal). The peptide showed high specificity over NE and PR3 and we employed it for the CG reporters showed in this work (**Figure 4 a** and **Figure 26 a**).
So far, all the substrate-based reporters to monitor CG activity could not provide any spatial localization and information. To fill this gap, we synthetized and characterized the SAM series of FRET reporters. We employed the general design optimized and validated by Gehrig and Cobos-Correa[45,63]. LaRee-1, NEmo-2 and mSAM reporters feature a palmitic acid derived lipid anchor, the energy donor (Coumarin 343) at the amino terminus of the peptide and the energy acceptor (5-(6)-TAMRA) at the carboxyl terminus. After protease cleavage, such arrangement permits signal retention at the plasma membrane of the fluorescent donor moiety and the diffusion of the acceptor one. Importantly, the two-fluorophore design permits for a ratiometric readout of the enzyme activity. The outcome is a spatially localized, self-normalizing signal which is less affected by environmental and experimental conditions (pH, polarity, laser power, reporter concentration) than single-fluorophore based and/or nonratiometric probes. Such advantage is crucial to study activity in complex samples like sputum, which commonly features within-patient variability, is usually filled with sticky mucus, includes 10 to 40% percent dying cells, and is therefore susceptible to many interfering external factors.

Even though Coumarin 343 and 5-(6)-TAMRA turned out to be a successful FRET pair, it needs to be highlighted that the Coumarin 343 excitation maximum (around 430 nm) limits *in vivo* imaging applications for LaRee, NEmo and SAM probes due to poor tissue penetration and elevated phototoxicity of blue lasers. However, membrane-bound NE activity on neutrophils loaded with NEmo-2 was exemplarily monitored via two-photon intravital real-time confocal microscopy in the ear dermis of a mouse model of epidermolysis bullosa acquisita[128]. Therefore, such potential application should be considered for future physiological and *in vivo* studies.

When characterized both *in vitro* and *in cellulo,* sSAM and mSAM showed adequate sensitivity. CG activity could be easily discriminated at low nanomolar concentration and the dynamic

range turned out to be ~7 for both reporters (**Figure 4 b** and **c**). Moreover, thanks to its palmitic acid tag, mSAM showed stable and satisfactory plasma membrane retention on HEK293, HL-60 (**Figure 5 c** and **d**) and 16HBE14o- cells.

When validating our novel set of probes and investigating the presence and activity of cathepsin G in CF and COPD airways, it was essential to carefully determine the reporters' specificity. The existence of proteases with minimal cleavage site requirements renders the design and synthesis of a perfectly specific protease substrate a daunting task. However, the physiological context in which the probe will be employed comes to help. Therefore, to test the *in vitro* specificity of SAM reporters we selected an array of enzymes whose presence and relevance in airway inflammation is well documented (**Figure 4 d**, **e** and **f**). None of the control proteases tested (neutrophil elastase, proteinase 3, matrix-metalloproteinase 12 and cathepsin S) cleaved the reporters. Only mast cell chymase could recognize and significantly cleave sSAM. However, chymase featured a 2.5 to 8-fold smaller turnover rate than CG (**Figure 6 h**). Also, we excluded its presence from patient samples (**Figure 6 i-k**). Moreover, the *in vivo* specificity of SAM reporters was thoroughly validated in human samples as well: the incubation of human sputum neutrophils and sputum supernatants or BL with specific cathepsin G inhibitors led to the abolishment of any significant increase in D/A (**Figure 6 d-g**). A limitation of this characterization is the lack of evidence about mouse NSP: it is known that homology between human and mouse neutrophil serine proteases is rather high[37], but if SAM reporters retain the same specificity towards mouse NSPs needs to be carefully assessed.

We then applied the newly characterized reporters to human samples. Free CG activity was studied via sSAM in healthy and cystic fibrosis sputum supernatants and COPD bronchial lavage fluids (**Figure 6 c**). Soluble elevated enzyme activity could be detected only in disease-derived samples. This result suggests that, in adult patients, CG overwhelms the antiprotease shield (that for CG is composed mainly of alpha-1-antichymotrypsin) and its activity becomes detectable in airway fluids. The plasma membrane localization of mSAM permitted the visualization and quantification of cell-surface bound CG activity (**Figure 6 a** and **b**), which turned out to be elevated on CF neutrophils. Importantly, the pool of CG which is membrane-bound may be useful for neutrophil translocation into the airways and to direct a precise ECM remodeling. In fact, it has been recently demonstrated that upon neutrophil adhesion a protected microenvironment is created between the cell and its target structure[128]. Such "closed compartments" ensure locally elevated protease concentration and protect the enzyme from inhibitors action. Therefore, the close contact of the triad neutrophil-enzyme-tissue seems to be indispensable for the damage to happen, and only tailored tools and drugs permit to unveil and prevent the phenomenon, respectively.

Unfortunately, we were not able to evaluate CG activity on COPD neutrophils due to lack of sample availability. It will be important to compare the differential levels of CG and other proteases (PR3 and NSP4, for which very little is known) in CF and COPD lung diseases.

In the future, the degree of activity and inhibition of free and membrane-bound CG activity should also be tested in β-ENaC mice and CF children, conditions characterized by milder airway inflammation.

4.1.2 Small molecule FRET flow cytometry enables the rapid evaluation of inflammatory biomarkers at the single-cell level

We sought to expand the way to monitor protease activity on cells and to overcome some key problems encountered with other technologies: plate reader measurements collect and average the signal originated from a whole cellular population, and do not allow for any cell-to-cell discrimination. Instead, confocal microcopy permits such spatial resolution. However, live cells cannot be discriminated from dying ones and mucus plugs produce a special environment. Sample preparation artifacts are common as well. Moreover, apart from the enzyme membrane-bound activity, no additional layer of information can be gathered. In contrast, other than measuring localized protease activity, flow cytometry analysis permits for a precise characterization of almost any cell type in biosamples, improves the quality of the measurement by excluding debris and dead cells via its microfluidics nature, and studying cell populations variability becomes possible.

To set up a versatile and informative flow cytometry assay, we designed and validated proper antibody panels (**Table 1**, **2** and **Figure 7**). Several optimization experiments where performed to improve the sensitivity and dynamic range of the assay (**Figure 8**). Then, cleavage of reporters was monitored over time in a ratiometric manner on human sputum. The technology was finally validated by correlating samples measured both via flow cytometry and microscopy (**Figure 7 f** and **Figure 9 d**). Moreover, we showed that the flow assay can be combined with clinical parameters (FEV1% predicted) and become a powerful tool to rapidly assess lung disease severity in hospital settings (**Figure 9 e**). We also envision that clinical studies will greatly benefit from the automation of such assay, which could be easily scaled to auto-sampling machines and 96 to 384-well plates and used to assess anti-inflammatory treatments at a large scale.

Recently, small molecule FRET probes that allow for the quantification of intracellular and phagolysosomal NE activity were developed[86].

The simultaneous measurement of intracellular and surface-associated NE activity via the combination of NEmo-2 and the aforementioned intracellular FRET probe has the potential to quantify and correlate enzymatic activities in distinct sub-cellular compartments. Interestingly, such advanced multiplexed assay might provide novel insights into how neutrophils secrete, regulate and localize proteases in the context of the airway microenvironment. In addition, the measurement of intracellular NE could add information regarding the amount of enzyme which is not secreted by the neutrophil even in the presence of strong proinflammatory stimuli.

4.2 Part II

4.2.1 CF and COPD airways feature similar membrane-bound NE activity but diverse inflammatory landscapes

Membrane-bound NE represents a fraction of the enzyme which is biologically active, inaccessible to antiproteases and fully retains its proteolytic activity[33]. Recently, it was shown in β-ENaC mice that NE activity appears at the neutrophil surface even before the free NE overwhelms the antiprotease shield in BAL fluids[47]. Therefore, the main focus of this project was to assess such spatially localized activity in CF and COPD adult patient sputum to unveil its diagnostic and therapeutic potential. Small molecule FRET flow cytometry assay fueled the analysis of a vast number of sputum samples (36 CF, 10 COPD, 8 healthy, at time of writing) in a significantly reduced amount of time. Interestingly, elevated and almost identical NE activity on CF and COPD neutrophils was observed (**Figure 11 b**). Such result does not reflect the comparison of NE content and activity in sputum supernatants, where CF supernatants show considerably higher values than COPD samples (**Figure 11 a** and **Figure 12**). To understand where this discrepancy comes from, we tried to depict the inflammatory environment in the healthy, CF and COPD airways.

In general, CF airways seemed to be characterized by a higher number of infiltrating neutrophils, higher pro-inflammatory factor levels (IL-8, IL-1β, TGF-β1, TNFα and soluble NE activity) and lower levels of the anti-inflammatory cytokine IL-10 (**Figure 13** and **Figure 14**). PCA and heatmap analysis confirmed the separation of the CF and COPD groups for the expression of unique patterns of inflammatory factors, while membrane-bound NE was elevated in both disease types (**Figure 15 a** and **b**).

These results depict a preliminary comparison of CF and COPD airway inflammatory factors. However, the study needs to be completed with the analysis of at least 15 to 20 further COPD sputum samples. Also, a more comprehensive picture will be obtained with the inclusion of

additional cytokines into the analysis, such as LTB4, IL5 and IL-1α. Importantly, LTB4 quantification in the bloodstream and in the airways of CF and COPD patients may provide a mechanistic explanation of the increased neutrophil number in the CF airways. Moreover, some COPD patients featured a prominent eosinophilic infiltration (**Figure 13**). The airways of such patients need to be deeply characterized; particularly, the correlation of eosinophil number with neutrophil subsets, cytokine content and NE activity may be useful to subclassify patient groups, and, as a result, to rethink tailored anti-inflammatory treatments. Finally, the access and analysis of membrane-bound and soluble NE activity in early stage COPD patient samples remain critical for the benchmark of the protein activity as excellent early inflammation biomarkers.

4.2.2 Neutrophil plasticity in sputum and blood of CF patients

The latest advancements in single-cell RNA-Seq and computational flow cytometry are providing the unprecedented opportunity to molecularly describe immune cell subsets, which often result in precious biomarkers[129–131]. The identification of neutrophil subpopulations in CF and COPD airways might result in tailored and more efficient therapeutic interventions and improve our understanding of neutrophil plasticity.

Therefore, we employed and validated a 12 color antibody panel (**Table 3**). Such array of antibodies allows for the study of different neutrophil phenotypes: CD63 is an indicator of neutrophil activation and primary granules secretion[112], Arginase 1 is secreted by neutrophils and induces T cells hyporesponsiveness[132], ICAM1 is expressed in combination with CXCR1 on neutrophils that reversely translocated from the site of inflammation to the bloodstream[133], CD66b is present at the surface of activated neutrophils which released their secondary and tertiary granules[112], CXCR4 is abundant on aged neutrophils[21], TLR4 is the receptor for PAMPs and CD16 is the Fc gamma receptor III which recognizes antibody-antigen complexes and induces neutrophils to phagocyte such aggregates. Importantly, CD16 is recognized and cleaved by two proteases (ADAM17 and NE), therefore its surface expression and the neutrophil phagocytosis ability is reduced when NE secretion is uncontrolled[134].

The analysis of sputum neutrophils via flow cytometry followed by FlowSOM revealed that healthy neutrophils consist of a more homogeneous population, all centered around a non-activated stage (**Figure 16 b**). Instead, CF neutrophils branch out and show a more intricate variety of markers expression (**Figure 16 b**). For example, the central and lower part of the CF graph (**Figure 16 b** and **c**) is composed of neutrophils which express CD16, indicating

phagocytic competence, while the top part features neutrophils which lost expression of such receptor. The expression of CD16 seems to be mutually exclusive to the expression of TLR4 (**Figure 16 c**). An explanation for this duality might be that neutrophils which are tailored to do phagocytosis do not sense bacteria and therefore do not secrete their granules and instead exploit the granular content to digest pathogens intracellularly[134]. Another functional consequence of the loss of CD16 at the neutrophil surface is an increased propensity to react via NETs production. In addition to support the hypothesis that phagocytosis and NETosis could be opposing neutrophil behaviors[135], a therapeutic shift towards an increase in the CD16 positive neutrophil population might be beneficial by reducing inflammation, maintaining neutrophil phagocytic ability and avoiding the secretion of large amounts of the pro-inflammatory NETs into the airways. Another interesting feature emerged from the FlowSOM analysis, namely that live neutrophils retain 70 to 90 % active NE in the primary granules, despite the cytokine storm that these cells face into the inflamed airways (**Figure 16 c**).

Once again, this study is limited by sample availability. Also, a more proper characterization will greatly benefit from an expanded antibody color panel. New technologies as spectral flow cytometry and mass cytometry will allow for more cellular populations and phenotypes to be analyzed together and different diseases could be compared.

Next, we investigated if the CF blood neutrophil response to inflammatory stimuli is different from the healthy cell behavior. The rationale of this investigation is that neutrophil remodeling and reprogramming may happen in the bloodstream before the neutrophils reach the target site in conditions characterized by intense or chronic inflammation such as bronchiectasis or CF. Bronchiectasis features extensive neutrophil inflammation and recurrent chest infections. Recently, it was shown that blood neutrophils in bronchiectasis patients are characterized by prolonged lifespan, reduced rate of apoptosis, increased release of myeloperoxidase, as well as defective bacterial phagocytosis and killing of PAO1[30]. Also, Pohl and coworkers showed that CF blood neutrophils feature impaired secretion of secondary and tertiary granules compared to healthy controls. This dysfunction was traced back to the lack of CFTR function in CF cells which impacted on cellular ion homeostasis. In fact, the treatment of CF blood neutrophils with a CFTR potentiator (Ivacaftor) rescued the defective phenotype[136].

To investigate neutrophil functionality in CF blood, we first counted the number of neutrophil per mL of blood in CF and healthy donors (**Figure 17**). CF blood count turned out to be elevated, pointing to potential changes in neutrophil behavior which might happen before translocation, when neutrophils circulate in the blood. At baseline, healthy blood neutrophils secreted more soluble NE (**Figure 18 a**). However, CF blood neutrophils responded by

secreting more active NE when challenged with proinflammatory stimuli (**Figure 18 a**, left panel). A similar scenario was observed when membrane-bound NE activity was measured (**Figure 18 b**) via small molecule FRET flow cytometry. In conclusion, CF blood neutrophils seemed to not be highly preactivated and did not show signs of dramatic reprogramming in terms of NE secretion, unless strongly stimulated. Immunofluorescence experiments carried out on unstimulated CF and healthy neutrophils showed that CF neutrophils contain in average more primary granules than healthy ones (**Figure 19 a** and **b**). Also, the volume of such granules turned out to be larger for CF cells (**Figure 19 c**). However, these results were not confirmed by immunostaining of intracellular NE and analysis via flow cytometry. Such discrepancy might be due to the different antibodies used for the assays or could reflect a different activation status due to the different preparation procedures for the two assays.

4.3 Part III

4.3.1 Analysis of protease activity on blood and airway exosomes

Extracellular vesicles populate the supernatant fraction of sputum and BAL fluids[116]. So far, the contribution and role of exosomes to the pathogenesis of lung diseases has been unexplored. Importantly, the measurement of NE activity in airway fluids might have been flawed by the lack of consideration towards the pool of enzyme in its exosome-bound form. In fact, no efforts were put into the separation of nano- and micro- sized vesicles from sputum and BAL supernatants. Our goal was to purify airway and blood nanovesicles and to dissect their exosome-bound NE activity.

Therefore, we first successfully isolated and characterized exosomes from healthy and CF sputum (**Figure 20 a** and **b**). Western bot analysis confirmed that CF but not healthy $CD63^+$ particles carried NE. Then, we set up an assay to study their NE associated activity and we could show that blood exosomes do not acquire any NE at their surface, highlighting how the vesicles become decorated with the enzyme only once in the inflamed airway (**Figure 20 c** and **d**). However, the absence of NE activity in blood exosomes could also be explained by the very high concentration of antiproteases such as A1AT which is commonly found in human plasma.

Exosome purification is a non-trivial and time-consuming process. The most used techniques are ultracentrifugation, commercial kits and size exclusion chromatography[137]. Often two or more methods need to be combined to achieve the desired vesicle purity. However, such long

procedures might affect exosomes integrity and drastically reduce protease activity. Also, the requirement of specialized equipment and personnel impairs the study of exosomes in a clinical setting. Therefore, we developed and validated an assay which takes advantage of a finely calibrated flow cytometer to measure activity on single nanoparticles, which offers drastic reduction in time required for sample preparation (**Figure 21** and **Figure 22**). A clear ratiometric signal was measured on exosomes stained with the specific exosomal markers CD63 and incubated with the reporter NEmo-2. This method will benefit further from the inclusion of additional surface markers for the discrimination of the cellular origin of airways exosomes. For example, CD63 and CD66b positive vesicles are known to be exclusively secreted by granulocytes[116]. Therefore, the inclusion of CD66b into the assay will permit to identify and quantify the proportion of neutrophil derived exosomes over the total vesicle population.

In addition, we employed the flow cytometric assay to rapidly screen patient samples for high exosomal NE activity. These samples were then used to visualize the export of active NE from the exosome to the surface of human bronchial cells (16HBE14o-) (**Figure 23**). However, if the export is facilitated by the contact of exosomes with the surface of epithelial cells or if the process will happen with the same efficiency when only free NE is tested, remains to be clarified. An interesting step forward will be the investigation of the inflammatory pathways at the molecular level which are activated by the action of exosomal NE and the degree of tissue disruption operated by the enzyme bound to such membrane systems where they are masked from endogenous antiproteases.

4.3.2 DNA binding probes to monitor extracellular DNA-bound NE and CG activities

To date, little information is available on the role, action and regulation of proteases bound to extracellular DNA. To fill this gap, we aimed at developing a tool to monitor protease activity in on DNA with high spatio-temporal resolution. To target a peptide to DNA, we initially employed an acridine derivative. Such molecules are known intercalating agents and have the advantage of bearing a carboxylic acid on the central pyridine ring for the direct coupling to the resin-bound peptide. However, the resulting probes failed to paint extracellular DNA properly. Next, we tested the hypothesis if bisbenzimide derivatives could serve as better DNA anchors. Such molecules are known DNA minor groove binders and represent the precursors of the widely used Hoechst stains. However, these molecules do not bear any functional group which can be employed for SPPS. Therefore, Hoechst 33258 needed first to be modified to present an

azide moiety which serves as orthogonal handle and can be coupled to an alkyne containing resin-bound peptide via click chemistry (**Figure 25**). This design allowed us to synthetize the DNA-binding H-CG and H-NE (**Figure 26**). The DNA-binding Hoechst localized the two FRET probes perfectly to DNA (**Figure 27** and **Figure 28**). However, the K_d of DNA binding remains to be calculated for both the probes. Also, at time of writing, the H-CG reporter has been only partially characterized in terms of specificity and sensitivity. Therefore, the results produced with H-NE are more emphasized through the text. The central peptides we selected for H-NE and H-CG were known to be highly specific towards their target proteases, thanks to the intensive optimization and careful design carried out by Korkmaz and colleagues over the past years[87,108,138]. In fact, H-NE and H-CG possess great specificity and were cleaved only by NE and CG, respectively. Importantly, extracellular DNA traps and contains an high number of bacteria[65,139]. This aspect, which was not considered for membrane-bound or soluble probes characterization, highlights the importance to evaluate H-NE and H-CG specificity over bacterial elastases. These experiments are currently work in progress and the FRET probes are being challenged against *S. aureus* and *P. aeruginosa* elastases as well as whole bacterial lysates.

H-NE and H-CG showed that NE but not CG is active in its extracellular DNA bound form (**Figure 29** and **Figure 30**). This result represents the first evidence that DNA has not a complete inhibitory effect on NE and therefore does not act only as a mere “protease reservoir”. Instead, DNA-bound NE may directly model the inflammatory environment. Interestingly, Albrengues and colleagues observed that the inhibition of NE but not CG in NETs-containing extracellular matrix prevents the awakening of dormant breast cancer cells in a model of inflammation[72]. Our results support such observations with a functional explanation and strengthen the concept that each protease activity has to be assesses in a context- and disease-dependent fashion.

When applied to human sputum, we could quantify elevated NE activity in large mucus-embedded DNA structures filling up the CF airways (**Figure 31**). This type of analysis and quantification will open the doors to new intriguing translational projects.

Finally, we also demonstrated that H-NE can be used to stain entire mouse lung slices (**Figure 32**). However, the way the mouse slices were prepared could be improved. In fact, we employed and sectioned paraffin-embedded lungs which were already present “in house”, while a paraformaldehyde perfusion fixation followed by cryosectioning would likely preserve enzymatic activity better[140]. However, since clear results in terms of NE activity inside neutrophils and on mucus-embedded DNA were observed, we decided to not sacrifice further animals for this purpose.

5. Conclusion

In the first part of this project, we describe the synthesis and characterization of specific FRET probes to monitor cathepsin G activity with spatial resolution. The probes proved to be sensitive and specific, therefore suitable for biomedical and clinical applications. In fact, the reporters showed elevated and potentially detrimental cathepsin G activity in CF and, for the first time COPD airways. Next, we implemented the use of NEmo-2, mSAM and LaRee-1 into flow cytometry. The assays showed great rapidity, simplicity of use and cross applicability, promising to aid in the study and assessment of inflammation in a plethora of conditions.

In the second part, we investigated NE activity in the context of COPD disease and compared it to the CF scenario. Interestingly, membrane-bound NE activity resulted to be elevated in all COPD patients independently of other bio-inflammatory markers or eosinophilic infiltration. We quantified that CF airways contained higher levels of IL-8, TNFα and IL1β, while COPD have more anti-inflammatory cytokine IL-10. The two main antiprotease A1AT and TIMP-1 seemed to be present at the same levels, with the exception of SLPI, a NE substrate. In light of this comparison, NE activity in COPD was confined at the neutrophil surface, while in the soluble fraction the antiprotease content might have been elevated enough to shield soluble NE. The identification of differences in blood neutrophils responsiveness in disease conditions could in principle constitute an important diagnostic parameter. However, only minor differences in NE secretion or neutrophil response were observed in CF compared to healthy blood cells.

In the last part of the project, we studied exosome-bound NE activity in CF airways and showed that exosomes carried active enzyme at their surface and potentially exported it to the surrounding cells. Finally, we synthetized and characterized FRET probes which associated to extracellular DNA and reported on NE and CG activity. They showed optimal localization, great sensitivity and their biomedical applicability was demonstrated. In addition, H-NE revealed elastase activity on blood NETs where it is presumably shielded from inhibitors under physiological conditions and contributes to inflammation. Finally, H-NE successfully stained cells in entire mouse lung slices, allowing for single-cell quantification of NE activity inside the nucleus of any cell-type. High activity was found in the nucleus of activated neutrophils and on mucus-embedded DNA.

Overall, this work highlights proteases as promising airway inflammation biomarkers and provides the tools to finely dissect their roles in diverse conditions.

6. Outlook

In the near future, we will focus our efforts on continuing the study of proteases at poorly characterized locations, such as exosomes and DNA webs. In particular, it will be interesting to unveil which protease-activated receptors (PARs) are activated by neutrophil elastase upon transfer from exosomes to epithelial cells. Furthermore, it will be important to characterize and quantify the diverse cellular origins of sputum exosomes by means of the single nanoparticle cytometric assay we developed. As far as DNA-bound proteases are concerned, our newly developed tools should reveal useful for the investigation of *in vivo* NE and CG activity in other complex systems, such as gallstones and tumors.

Our main long term ambition is the broad application of the tools developed in this thesis and from previous work in the clinical routine. We envision that in the future specific neutrophil phenotypes will be linked to distinct disease statuses and improve treatments in a patient tailored fashion.

Furthermore, small molecule FRET flow cytometry has the concrete potential of turning membrane-bound protease activity into a useful clinical endpoint. For example, cathepsin C inhibitors are currently under development and attract attention and funding[37]. Since cathepsin C is fundamental for the processing of the protease proforms, their potential relies on the simultaneous effect on all NSPs. We believe that small molecule FRET flow cytometry is the perfect fit for testing the efficacy of such drugs on a large scale.

Indeed, the assessment of membrane-bound NE activity by small molecule FRET flow cytometry was included as secondary endpoint into the ANAKINRA clinical trial earlier this year, which is evaluating the effect of IL-1 receptor antagonists to dampen inflammation in human cystic fibrosis.

The relevance of research at the intersection of inflammation and chemical biology, the importance of developing fast and easy-to-use diagnostic tools and their implementation in hospitals have been exposed to the general public by the difficulties faced to counteract rapidly spreading diseases, such as COVID-19.

7. Methods

7.1 Chemicals and reagents

Standard solvents for chemical synthesis were bought from Fluka, Sigma-Aldrich (Steinheim, Germany) and Novabiochem (Darmstadt, Germany) and used without further purification. Coumarin 343 was purchased from Sigma Aldrich (Darmstadt, Germany). 5,6-Carboxytetramethylrhodamine-N-Hydroxysuccinimide (5,6-TAMRA-NHS ester) was purchased from Anaspec. COMU was from Sigma Aldrich, SPPS resins and Fmoc-protected aminoacids were from Novabiochem, Fmoc-O2Oc-OH (PEG-linker) was from Iris Biotech, Fmoc-Lys(palmitoyl)-OH was from Sigma Aldrich. Hoechst (bisBenzimide H 33258) was purchased from Sigma. Fmoc-propargyl-Gly-OH was purchased from Sigma Aldrich, Br-PEG-azide was purchased from BroadPharm (SanDiego, USA). Cell culture media and supplements for the HEK293, HL-60 and 16HBE14o-cell lines were ordered from Gibco/Thermo Fisher Scientific.

7.2 Enzymes, substrates and antibodies

Neutrophil elastase, proteinase 3 and cathepsin G were purchased from Elastin Products Company Inc. (Owensville, Missouri). MMP-12 (catalytic domain, human, recombinant) was from Enzo Life Sciences. Chymase and cathepsin S were purchased from Sigma Aldrich.
Chymase substrate, activity kit and ELISA assay was from Sigma-Aldrich. Cytometric Array Beads (CBA) kits were purchased from BD Biosciences (Heidelberg, Germany). Cytokine and antiprotease ELISA kits were purchased from R&D Systems (Minneapolis MN). Phorbol 12-myristate 13-acetate (PMA) was purchased from Sigma Aldrich. Antibodies used for flow cytometry were purchased as follow:

antibody	company	catalog	clone
BV421 Mouse Anti-Human CD181	BD	73419	5A12
BV711 Mouse Anti-Human TLR4 (CD284)	BD	564404	TF901
BD Horizon™ V500 Mouse Anti-Human CD45	BD	560779	HI30
BD Pharmingen™ Alexa Fluor® 700 Mouse anti-Human CD16	BD	557920	3G8
BD Pharmingen™ APC-Cy™7 Mouse Anti-Human CD45	BD	557833	2D1
BD Pharmingen™ PE-Cy™7 Mouse Anti-Human CD14	BD	557742	M5E2
FITC anti-human CD63 Antibody	BioLegend	353005	H5C6
PE/Dazzle™ 594 anti-human CD54 Antibody	BioLegend	353117	HA58
PerCP/Cyanine5.5 anti-human CD66b Antibody	BioLegend	305107	G10F5
Brilliant Violet 605™ anti-human CD184 (CXCR4) Antibody	BioLegend	306521	12G5
PE anti-human Arginase I Antibody	BioLegend	369703	14D2C43
Alexa Fluor® 647 anti-human CD63 Antibody	BioLegend	353016	H5C6
PE/Dazzle™ 594 anti-human CD66b Antibody	BioLegend	305122	G10F5
Human Neutrophil Elastase/ELA2 Alexa Fluor® 647-conjugated Antibody	R&D	IC91671R	950317
Alexa Fluor® 647 anti-human CD169 Antibody	BioLegend	346006	7-239

7.3 Solid phase peptide synthesis of SAM, A-NE/A-CG and H-NE/H-CG reporters

All peptides were synthesized via standard solid phase peptide synthesis (SPPS) on a Wang resin preloaded with Fmoc-Lys(Mtt)-OH. The resin was swelled in DMF for 30 min and Fmoc-deprotected by treatment with 20% piperidine/DMF. After three deprotection steps, complete removal of Fmoc was monitored via loss of Fmoc absorbance. All amino acids and the PEG linker were coupled using 3 equivalents of the respective amino acid, 3 equivalents of COMU, 4 equivalents DIPEA in DMF two times for 45 min at RT. The resin was washed three times with DMF in-between all reactions. To protect unreacted free amino groups, the peptides were treated two times for 5 min with acetic anhydride/pyridine (1:9). Dyes (3 equivalents of coumarin 343 carboxylic acid, 2 equivalents of 5(6)-TAMRA NHS ester) were coupled with COMU/DIPEA (3:4 equivalents) for coumarin and 6 equivalents of DIPEA for 5,6-TAMRA-NHS ester, two times for 45 min at RT.
Once the central peptide and the PEG linker were completed, individual probes were synthetized as follow:

- sSAM was obtained by first deprotection of the methyltrityl group of the C-terminal lysine (TFA/TIS/DCM 1:2:97, 4 min, seven times), followed by 5,6-TAMRA-NHS ester coupling. Finally, the N-terminal Fmoc group was deprotected, and coumarin 343 was coupled.
- mSAM was obtained by first coupling 5,6-TAMRA-NHS ester to the C-terminal lysine. Then, the N-terminal lysine (palmitic acid) was Fmoc-deprotected and coumarin-343-coupled.
- For A-NE and A-CG, the Mtt group was cleaved. Then, 5,6-TAMRA-NHS ester was coupled. For coumarin coupling the peptide was deprotected and coumarin 343 was coupled.
- For H-NE and H-CG, the alkyne containing reporters (A-NE and A-CG) were incubated with 5 equivalents of Hoechst-azide over night at RT with Copper(I) and TBTA in a 1:1 water/DMSO solution.

Eventually, the final products were cleaved off the resin using a 96% TFA solution, precipitated in diethylether (-20°C) and centrifuged. The precipitated reporter was resuspended in methanol and purified by a semipreperative HPLC using appropriate water acetonitrile gradient. The concentration of the all the probes was measured via UV/VIS spectroscopy using the absorbance of Coumarin343 (extinction coefficient ε=44140 L*mol-1*cm-1) in ethanol.

Reporters analytical HPLC, purity, high resolution mass spectrometry and NMR of Hoechst-azide can be found in the appendix section.

7.4 Synthesis of Hoechst-azide

Br-PEG-azide was employed for the alkylation of the free base of the Hoechst 33258 dye to obtain the Hoechst-azide (Compound 3 in **Figure 25**). The free base of Hoechst 33258 was prepared by dissolving Hoechst 33258 hydrochloride in H_2O (0.1 M) and adding a solution of 3.1 equivalents of 7 M K_2CO_3. The precipitate thus formed was isolated by centrifugation, washed with H_2O and freeze dried. Hoechst 33258 base 2 (1 eq) was then resuspended in dry DMF (0.2 M) and K_2CO_3 (0.15 mM). Eventually, Br-PEG-azide (3 equivalents) was added. The reaction was heated at 60 °C and stirred under vacuum for 18 h. Once the mixture was cooled to RT, it was purified via semipreperative HPLC.

7.5 Analysis of reporters' performance *in vitro*

Neutrophil elastase, proteinase 3, cathepsin G, matrix metalloproteinase 12, chymase and cathepsin S activities were measured in activity assay buffer (100 mM TRIS, 500 mM NaCl, pH 7.5) at RT. For assays of the lipidated reporters like mSAM, 1 mM liposome solution was prepared of phosphatidylcholine/phosphatidylserine (PC/PS) (9:1) (Avanti Polar Lipids, Inc., Alabaster, AL) in activity assay buffer by extrusion following standard protocols. Briefly, lipids were dissolved in chloroform. Afterwards, the solution was evaporated under slow argon flow. Finally, the lipids were rehydrated in activity assay buffer at 62°C, and shaken for 1 h at 62°C. Afterwards, the liposomes were extruded by means of an extruder. The homogeneity and size of the liposomes was assessed by dynamic light scattering (DLS).

Assays of H-CG and H-NE were carried out in activity assay buffer supplemented with 20µM of the hairpin-forming oligonucleotide 5′-CGCGAATTCGCGTTTTCGCGAATTCGCG-3′ (28 bp) purchased from Microsynth[120]. mSAM assays were performed in black cuvettes and measured by the FP-8500 JASCO spectrofluorometer at RT. The assays for sSAM and HNE and HCG and ANE and ACG were performed in polystyrene 96 well half area assay plates (Corning Inc., Acton, MA) with a fluorescence plate reader (Safire II Tecan, Crailsheim, Germany) at RT. Unless otherwise specified the reporter concentration for *in vitro* experiments was 2 µM. For mSAM measurements, enzymes were added, and reporter cleavage was followed by recording emission spectra every 5 min over a period of 20−70 min with the settings: λexc = 430 nm, λem = 450−650 nm, all measurements were performed in technical triplicates. For sSAM, H-NE, H-CG, A-NE and A-CG measurements, enzymes were added,

and the emission maxima of donor (485 nm) and acceptor (580 nm) fluorophores after 405 nm excitation were recorded every 90 s over a period of 60 min and plotted as donor/acceptor ratio. All measurements were performed at least two times. The dynamic range of the reporters was defined as complete cleavage of the probe calculated as maximal ratio change (RC_{max}).

7.6 Cell culture

HL-60 cells were passaged and maintained in Iscove's Modified Dulbecco's Medium with 20 % FBS in T-75 culture flasks. Cell density was kept between 1 x 10^5 and 1 x 10^6 viable cells/mL. Medium change and cell splitting was performed every 2-3 days. HEK cells were cultured in high glucose Dulbecco's modified Eagle's Medium containing 10% FBS and 1 % penicillin/streptomycin in T-75 culture flasks. Medium change and cell splitting was performed every 2-3 days and cell confluence was kept below 95%. 16HBE14o- cells were obtained from Dr. Catherine M Greene (Royal College of Surgeons in Ireland). Cells between 47 and 63 passage number were used. Cells were seeded on plastics coated with LHC-8 medium (Gibco, #12678-017) with 2.9 mg/mL collagen type I (Corning, #354231), 1 mg/mL fibronectin (Calbiochem, #341635) and 1 mg/mL BSA (Sigma-Aldrich, #A9647) and grown at 37 °C and 5 % CO2 in minimal essential medium (MEM) (Gibco, #21090-022) containing 2 mM glutamine (Gibco, #25030- 024), 10 % FBS (Gibco, #10270-106) and 0.1 mg/mL Primocin™ (InvivoGen, #ant-pm-1) with medium change every 2/3 days.

7.7 Human sputum processing and cell isolation

All human samples were collected upon signed written informed consent, which was approved by the Ethics Committee of the University Hospital Heidelberg. To induce sputum in healthy donors, the mouth cavity was rinsed with water first, then an aerosol of 6% sodium chloride solution was inhaled for 15-20 minutes. The bronchodilator Salbutamol was used to widen the bronchi and avoid adverse autoimmune effects. The induced sputum was then collected in a petri dish. 4 volumes of 10% Sputolysin solution (Calbiochem, Darmstadt, Germany) were added to sputum to dissolve mucins and the mixture was mildly shaken for 15 min at room temperature. The mixture was then diluted by adding the same volume of cold PBS and filtered twice through 100 and 40 µm cell strainers. Finally, the solution was centrifuged at 300g and 4°C for 10 min. Cell pellets were resuspended in PBS and counted whereas sputum supernatants were frozen at - 80° for further analysis.

7.8 Sputum samples preparation for plate reader and microscopy assays

Healthy, CF and COPD sputum supernatant was diluted in 100 mM TrisHCl pH 7.5, 500 Mm NaCl. All kinetic assays were performed at 25 °C. Supernatants were preincubated with 25 µM cathepsin G inhibitor I (CAS 429676-93-7, Merck, Darmstadt, Germany) for 15 min at room temperature as negative control. For quantification of CG activity with sSAM, 40 µL of supernatant was added in polystyrene 96-well half area assay plates (Corning Inc., Acton, MA). Finally, sSAM was added to a final concentration of 2 µM. For CG concentration quantification, a standard curve made by defined enzyme concentrations were included in each plate. All measurements were performed in technical duplicates. Then, the active enzyme concentration was calculated via interpolation of the measured slopes via linear fitting.
For microscopy experiments, 30 000 human CF or healthy donor sputum cells were incubated in 50 µL of PBS with mSAM [2 µM] and Draq5 DNA stain (BioStatus Limited, Shepshed, U.K.) (1:1000 dilution), for 1 or 20 min at room temperature. For H-NE experiments, only 2 µM of the probe were incubated with sputum cells. α1-antichymotrypsin (ACT) (Merck KGaA, Darmstadt, Germany), cathepsin G inhibitor I (CGI) (CAS 429676-93-7, Merck, Darmstadt, Germany), cOmplete Protease Inhibitor Cocktail with EDTA (Merck, Darmstadt, Germany), or Sivelestat (S7198, Merck, Darmstadt, Germany) were used as inhibitor controls. Eventually, the reaction mixture was quenched at different time points by adding 100 µL of ice cold PBS, and cells were quickly cytospun on microscopy slides, fixed for 10 min in ice cold methanol, and mounted with Roti-Histokitt (Carl Roth, Karlsruhe, Germany).

7.9 Human whole blood collection, neutrophil purification and stimulation

Peripheral venous blood was collected in Vacutainer tubes (BectonDickinson) with citric acid as anticoagulant and processed rapidly after collection (within 15 min). Blood neutrophils were purified by means of the MACSxpress Whole Blood Neutrophil Isolation Kit (Miltenyi Biotec, #130-104-434) according to manufacturer's protocol. To eliminate erythrocytes, the protocol was modified by adding 4.5 mL red blood cell lysis buffer (Invitrogen™, #00-4300-54) before the last centrifugation step and cell counting.

For blood neutrophil stimulation experiments, after cell counting, neutrophils were seeded in HBSS medium (with Calcium and Magnesium) at a concentration varying from 75000 to 125000 cells in 8-wells chamber slides for 30 min at 37°C 5% CO_2. Then, cells were stimulated with priming agents (TNFα) or Cytochalasin B for 5 minutes and followed by 30 min stimulation of FMLP. Once stimulation was complete, cells were scraped with a pipette tip and supernatant

was separated via centrifugation at 300g for 10 min at 4°C. Neutrophils were then analyzed by flow cytometry whereas supernatant measured at the plate reader.

For blood neutrophil NETs production experiments, after cell counting, neutrophils were seeded in HL-60 medium at a concentration varying from 75000 to 125000 cells in 8-wells chamber slides for 30 min at 37°C 5% CO_2. Then, cells were stimulated with PMA [2µM] for 2.5 hours. When H-NE and Draq5 colocalization experiments were assessed, H-NE [2µM] was incubated with 1:30000 Draq5 for 30 min on PMA-stimulated blood neutrophils. Then, cells were washed 1x with PBS, fixed with PFA 4% in PBS for 20 min at 37°C 5%, washed 1x with PBS and 2x with distilled water, dried and mounted. For H-NE and H-CG experiments with NE and CG addition (both for positive controls in **Figure 29** and **30** and to prove the suitability of the reporter to detect DNA-bound enzymatic activity in **Figure 28 f-h**), PMA-stimulated NETs were washed 1x with PBS, then incubated with enzyme for 30 min. After enzyme incubation, NETs were carefully washed 2x with PBS to remove enzyme unbound excess. Then 2µM of reporter was incubated for 30 min. Finally, NETs were washed 1x with PBS, fixed with PFA 4% in PBS for 20 min at 37°C 5%, washed 1x with PBS and 2x with distilled water, dried and mounted. For permeabilization experiments showed in **Figure 27**, neutrophils were seeded for 30 min and then fixed with PFA as aforementioned. Next, cells were permeabilized with 0.1% Triton X100, then washed 2x with PBS. Finally, reporter was added for 30 min and cells washed 1x with PBS and 2x with distilled water, dried and mounted.

7.10 Cytokine and antiprotease measurements

Sputum supernatants were thawed on ice and cytokines were measured via cytometric array beads (CBA) assay (BD Bioscience, Heidelberg, Germany). IL-1α, IL-1β and IL-8 were measured via standard measurement, while IL-6, IL-10, TNF-α, INF-γ and TGF-β1 via enhanced sensitivity kit. All measurements were carried out according to manufacturer's protocol. A1AT, TIMP, and SLP were measured via ELISA assays according to manufacturer's protocol.

7.11 Mouse lung slices

Mouse handling and lung sectioning were performed by Dr. Matthias Hagner and Jolanthe Schatterny. Briefly, mice sacrificed by intraperitoneal injection with ketamine (120 mg/kg) and xylazine (16 mg/kg) followed by exsanguination. Then, the lungs were inflated with fixative of

4 % buffered formalin to 25 cm of fixative pressure, stored in 4 % buffered formalin. For cutting, the apical part of the fixed lungs was cropped transversally and lungs were placed in embedding cassettes (Steinbrenner Laborsysteme, Wiesenbach, Germany) and dehydrated 2 times for 30 minutes in 96 % ethanol, 2 times for 45 minutes in 100 % ethanol, and overnight in xylene. Samples were then submerged in paraffin and vacuum was applied for 2 hours followed by 1 hour at atmospheric pressure. Afterwards, lungs were placed in embedding molds. Paraffin blocks were kept overnight at 4°C for complete solidification. Then, lungs were sectioned with a microtome (Leica Microsystems, Nussloch, Germany). Section height was kept to 5 µm and lungs were sectioned transversally at the level of the proximal intra-pulmonary main axial airway. For microscopy experiments and H-NE staining, lung sections were deparaffined in xylene and rehydrated 2 times for 10 minutes in 100 % ethanol, 2 times for 2 minutes in 96 % ethanol, 2 times for 2 minutes in 70 % ethanol and finally rinsed in distilled H2O. Then, lung sections were incubated with 200 µL of a PBS solution of [1mM] Sivelestat or active NE for 30 min. Afterwards, the slices were washed in PBS and incubated with a solution of 200 µL of a PBS solution with [2µM] H-NE for 3 hours in dark at RT. Finally, lungs were washed in PBS, dried and mounted with RotiHisto Kit.

7.12 Exosome purification and assays

Exosomes from whole blood were isolated using Total Exosome Isolation Kit (from plasma) (Invitrogen™, #4484450) according to manufacturer's protocol and the retrieved exosomes pellet was resuspended in PBS and stored at -80 °C. As far as exosome isolation from sputum sample is concerned the Total Exosome Isolation Kit (from cell culture) was employed according to manufacturer's protocol. The exosomes pellet was resuspended in PBS and either stored at -80 °C or used directly for flow cytometry staining and measurements. Total exosome protein content was then measured via Pierce™ BCA Protein Assay Kit (Thermo Scientific™, #23225). Transmission electron microscopy of purified sputum exosomes was performed with the help Christian Zimmerli. Exosomes were visualized with uranyl acetate negative staining. Briefly, samples were deposited on glow discharged TEM grids and, after PFA 4% fixation for 5 min at RT, 2% uranyl acetate was added for 1 min. After 2x washing with distilled water, grids were left to dry. A Morgagni microscope equipped with a side-mounted 1K CCD Camera (SIS) was used to image grids.

Western blots were performed by loading 10 µg of total protein on polyacrylamide gel and run at 50V for 5 min and then 45 min at 150V. Then, the gel was blotted on a PVDF membrane for 30 minutes at 1.0 A and up to 25 V. After washing three times in TBTS buffer, the membrane

was blocked in TBTS buffer containing 5% milk powder. The primary anti neutrophil elastase antibody was diluted 1:5000 and the anti CD63 1:250 in blocking buffer and incubated with the membrane overnight at RT and mildly shaking. Afterwards, the membrane was washed with blocking buffer and the secondary antibody incubated for one hour at RT. After washing, chemiluminescent signal was read with the CCDcamera-based ChemiDoc™ XRS+ system.

To isolate and use for NE activity measurements $CD63^+$ exosomes the Exosome–Human CD63 Isolation/Detection (from cell culture medium) kit (Invitrogen, #10606D) was employed in combination with the Dynabeads® magnetic separation technology. For the simultaneous purification of CD63, CD9 and CD81 positive sputum exosomes, the Tetraspanin Exo-Flow Combo Capture Kit (System Biosciences, #EXOFLOW150A-1) was used. For plate reader experiments showed in **Figure 20 c**, the same amount (measured via BCA assay) of exosomes bound to CD63 Dynabeads® were either washed with isolation buffer (0.1% BSA in PBS filtered through 0.2 µm filter) or incubated with 0.1% Triton X-100 for 10 minutes. The NE activity on exosomes bound to beads was measured via plate reader assay using NEmo-1 reporter. Furthermore, CD63-antibody coupled beads were incubated with NE to examine whether the protease unspecifically finds to the purification beads.

7.13 Confocal microscopy

All microscopy images were acquired using a confocal Leica SP8 microscope (Leica Microsystems, Wetzlar, Germany) equipped with either a PL APO 40x or 63X oil objective. Hoechst 33258 was excited with the 405 UV laser line. Coumarin 343 was excited with the 458 nm Argon laser and its emission sampled between 470 and 500 nm. 5,6-TAMRA direct excitation was carried out with the 561nm diode pumped solid state (DPSS) laser and sampled between 590 and 630 nm. Sensitized acceptor emission was recorded, upon coumarin 343 excitation, between 590 and 630 nm. The nuclear stain Draq5 and the secondary antibodies of immunofluorescence experiments which were coupled with the Alexa Fluor 647 dye were excited with a helium-neon-laser line at 633 nm. The pinhole was set variably. For live cell imaging, an environment chamber (EMBL, Heidelberg) set at 37°C and 5 % CO_2 was used. Images and movies were analyzed by Fiji and the ImageJ macro “FluoQ” (version 3-97)[141]. The macro operates a background subtraction by ImageJ’s built-in rolling ball function, then, it allows the operator to set manually a channel threshold. Finally, images are smoothed via a median filter. Region of interest (ROIs) are selected manually by drawing their border with the pencil tool. When z stacks were processed, the Z-projection of the average intensity of the

donor channel was used as channel for cell segmentation. The change in donor/acceptor ratio was then calculated as mean pixel intensity of each ROI (over time in case of time series) from both channels and the ratio between the donor and acceptor was obtained. The same macro was used for colocalization analysis and Pearson correlation coefficient and Area overlap calculation. Plots and analysis were carried out with R version 3.6.1.

As far as imaging of exosomes stimulated 16HBE14o- cells is concerned, the cells were let to grow for 2-4 days in 8-wells chambered cover glasses, seeding the day 1 from 20 to 50000 cells per well. Right before imaging, cells were washed with MEM 1x two times and Draq5 and NEmo-2 [2 µM] were added. After circa 10 minutes of imaging, CF or healthy exosomes (0.3ug/µL final concentration) were added to cells and movies were recorded for 50 min more.

For immunofluorescence experiments, purified blood neutrophils were seeded for 30 min in 8-well Nunc™ Lab-Tek™ Chambered Coverglass with removable wells at 37°C, 5% CO_2. Cells were then fixed with a solution of 4% PFA in PBS for 20 min at RT, then washed 1x with PBS. Cells were permeabilized with Triton X-100 0.1% for 10 min at RT, then washed 3x PBS. After, blocking solution (Block Aid, thermo fisher) was added to each well at RT for 30 min. Then the primary antibody Anti-ELA2 (10 µg/mL final concentration, diluted in blocking buffer) was added and incubated for 1 hour at RT. Cells were then washed 3 times with PBS and the secondary antibody was added for 1 hour in dart at RT. Finally, cells were washed 3x with PBS, Hoechst 33258 was incubated for 5 min and wells washed one last time 2x with PBS and 2x with distilled water before drying, and mounting.

7.14 Flow cytometry

Flow cytometry was performed on a LSR Fortessa flow cytometer (BD Biosciences, Heidelberg, Germany) equipped with 3 lasers at wavelengths of 405, 488, and 633 nm. For the measurement of enzymatic activity, the probe was excited with the 405 nm laser and the donor and acceptor emission intensities were recorded with a 450/50nm and a 585/42 nm filter, respectively. The acceptor filter had an upstream long-pass filter in front to reflect light below 550 nm. For FRET flow cytometry, cells were isolated from healthy, CF and COPD sputum, and 1 million cells were resuspended in 100 µL of PBS, followed by incubation with 2 µL of FcBlock (BD Biosciences, Heidelberg, Germany) for 5 min. Afterwards, cells were stained with surface specific monoclonal fluorochrome-conjugated antibodies or the respective isotype antibodies serving as negative control. Staining was performed for 30 min at 4°C. Then cells were resuspended in 200 µL PBS and incubated with the 7AAD (Biolegend, San Diego, USA)

viability stain for 10 min at 4°C. Then, the appropriate reporter was added to cells and flow cytometry was performed immediately after. At least 1000 neutrophils were always recorded. Data were analyzed with FACS Diva software v8.0.1 (BD Biosciences, Heidelberg, Germany) or Flow Jo software v10 (Treestar, Ashland, OR).

For the optimization experiments showed in **Figure 8,** HL-60 cells were used. Different cell numbers were incubated with different concentrations of mSAM or NEmo-2 and analyzed by flow cytometry (LSRFortessa, Becton Dickinson, Heidelberg). Such cells were stained only with the 7AAD viability marker and were gated with the forward and side scatter that allow to exclude doublets in addition to 7AAD negativity. To compensate for bleed-through the mSAM donor fragment was added at different concentrations and its MFI in the donor and acceptor channels measured.

For the analysis of sputum neutrophil phenotypes shown in **Figure 16**, the antibody panel contained 9 surface markers, 2 intracellular ones and the 7AAD viability stain (**Table 3**). First, a master mix (32 µL x n samples) containing the surface antibodies was prepared:

- FITC CD63 5 µL
- PEDAZZLE CD54 5 µL
- Percpcy55 CD66b 3 µL
- BV605 CD184 5 µL
- BV421 CD181 2 µL
- BV711 TLR4 5 µL
- V500 CD45 3 µL
- PECY7 CD14 2 µL
- AF700 CD16 2 µL

The, 32 µL of the master mix were incubated per tube for 30 min at RT. Then, staining with surface markers was followed by fixation and permeabilization with FIX & PERM Cell Fixation & Cell Permeabilization Kit (Thermo Fisher) according to manufacturer's instructions and subsequently incubated with NE-AF647 and Arginase1-PE antibodies. Briefly, after incubation for 30 min with the surface marker panel, cells were resuspended in 2 mL cold PBS, then centrifuged 1400 rpm 5min 4°C and resuspended 1 mL PBS. 0,75 µL live/dead marker was added to each tube and incubated 20 min dark on ice. After, cells are washed in 2 mL FACS buffer and centrifuged 1400 rpm 5min 4°C and 3 mL cold PBS are added followed by centrifugation 1400 rpm 5min 4°C. Cells were resuspended in 100 µL cold PBS and 150 µL of Fixation Buffer added and incubated 40 min dark RT. After, 2 mL cold PBS were added followed by centrifugation 1400 rpm 5min 4°C. Cells were resuspended in 200 µL PBS and left

overnight at 4°C. The day after 2 mL of 1x Permeabilization buffer were added and incubated 10 min at 4°C. Cells were centrifuged 1400 rpm 5 min 4°C and resuspended in 100 µL Perm buffer 1x. Then a master mix containing the intracellular antibodies was prepared as follow (5 µL x n samples):

- AF647 ELA2 2 µL
- PE Arg1 3 µL

5 µL of master mix were added per tube and incubated for 30 min on ice in dark. Finally, 2 mL of 1x Perm buffer were added, followed by centrifugation and 2 mL PBS addition, one last step of centrifugation and cells were resuspended in 200 µL of PBS and ready for analysis. Flow cytometry was performed on a BD LSRFortessa cell analyzer (BD Biosciences, Heidelberg, Germany) and data were analyzed with FACSDiva software or Flow Jo software.

Antibodies were titrated and IgG controls were performed as follow:

Fluorophore	Antibody	Stock concentration	µL to add
FITC	CD63	0,2 (mg/ml)	2,3,5
PE	Arg1	0,05 (mg/ml)	1,2,3,5,
PEDazzle594	CD54	0,1 (mg/ml)	1,2,3,5,
PerCPcy5.5	CD66b	0,05 (mg/ml)	2,3,5
BV605	CD184 (CXCR4)	0,1 (mg/ml)	1,2,3,5
unstained			

IgG Isotype	Stock concentration	Dilution factor	µL to add
FITC	0,2 (mg/ml)	1x	2,3,5
PE	0,2 (mg/ml)	4x	1,2,3,5,
PEDazzle594	0,2 (mg/ml)	2x	1,2,3,5,
PerCPcy5.5	0,1 (mg/ml)	2x	2,3,5
BV605	0,1 (mg/ml)	1x	1,2,3,5

Table 4 List of antibodies and concentration employed for the validation of the antibody panel. Data refers to staining of one million cells.

7.15 Statistics

All statistical tests and FlowSOM analysis were performed using R software (R version 3.6.1) and GraphPad version 6.01. Two-tailed Wilcoxon rank sum test (U Test), Pearson or Spearman's rank correlation coefficient tests, and linear or 4PL fitting to standard curves were applied when appropriate.

8. References

1. Zepp, J. A. & Morrisey, E. E. Cellular crosstalk in the development and regeneration of the respiratory system. *Nat. Rev. Mol. Cell Biol.* **20**, 551–566 (2019).
2. The lungs at the frontlines of immunity. *Nat. Immunol.* **16**, 17 (2015).
3. McMillan, S. J. *et al.* Matrix Metalloproteinase-9 Deficiency Results in Enhanced Allergen-Induced Airway Inflammation. *J. Immunol.* **172**, 2586–2594 (2004).
4. Lloyd, C. M. & Marsland, B. J. Lung Homeostasis: Influence of Age, Microbes, and the Immune System. *Immunity* **46**, 549–561 (2017).
5. Fahy, J. V. & Dickey, B. F. Airway Mucus Function and Dysfunction. *N. Engl. J. Med.* **363**, 2233–2247 (2010).
6. Mostowy, S. *et al.* Entrapment of intracytosolic bacteria by septin cage-like structures. *Cell Host Microbe* **8**, 433–444 (2010).
7. Leiva-Juárez, M. M., Kolls, J. K. & Evans, S. E. Lung epithelial cells: Therapeutically inducible effectors of antimicrobial defense. *Mucosal Immunol.* **11**, 21–34 (2018).
8. Montgomery, S. T., Mall, M. A., Kicic, A. & Stick, S. M. Hypoxia and sterile inflammation in cystic fibrosis airways: Mechanisms and potential therapies. *Eur. Respir. J.* **49**, 1–13 (2017).
9. Elborn, J. S. Cystic fibrosis. *Lancet* **388**, 2519–2531 (2016).
10. Decramer, M., Janssens, W. & Miravitlles, M. Chronic obstructive pulmonary disease. 1341–1351 (2012). doi:10.1016/S0140-6736(11)60968-9
11. De Rose, V., Molloy, K., Gohy, S., Pilette, C. & Greene, C. M. Airway epithelium dysfunction in cystic fibrosis and COPD. *Mediators Inflamm.* **2018**, (2018).
12. Hartl, D. *et al.* Innate immunity in cystic fibrosis lung disease. *J. Cyst. Fibros.* **11**, 363–382 (2012).
13. Montoro, D. T. *et al.* A revised airway epithelial hierarchy includes CFTR-expressing ionocytes. *Nature* **560**, 319–324 (2018).
14. Plasschaert, L. W. *et al.* A single-cell atlas of the airway epithelium reveals the CFTR-rich pulmonary ionocyte. *Nature* **560**, 377–381 (2018).
15. Bell, S. C. *et al.* The future of cystic fibrosis care: a global perspective. *Lancet Respir. Med.* **8**, 65–124 (2020).
16. Mall, M., Grubb, B. R., Harkema, J. R., O'Neal, W. K. & Boucher, R. C. Increased airway epithelial Na+ absorption produces cystic fibrosis-like lung disease in mice. *Nat. Med.* **10**, 487–493 (2004).
17. Fritzsching, B. *et al.* Hypoxic epithelial necrosis triggers neutrophilic inflammation via IL-1 receptor signaling in cystic fibrosis lung disease. *Am. J. Respir. Crit. Care Med.* **191**, 902–913 (2015).
18. Montgomery, S. T., Mall, M. A., Kicic, A. & Stick, S. M. Hypoxia and sterile inflammation in cystic fibrosis airways : mechanisms and potential therapies. 1–13 doi:10.1183/13993003.00903-2016

19. Wang, H. *et al.* Global, regional, and national life expectancy, all-cause mortality, and cause-specific mortality for 249 causes of death, 1980–2015: a systematic analysis for the Global Burden of Disease Study 2015. *Lancet* **388**, 1459–1544 (2016).

20. Dey, T., Kalita, J., Weldon, S. & Taggart, C. Proteases and Their Inhibitors in Chronic Obstructive Pulmonary Disease. *J. Clin. Med.* **7**, 244 (2018).

21. Hidalgo, A., Chilvers, E. R., Summers, C. & Koenderman, L. The Neutrophil Life Cycle. *Trends Immunol.* **40**, 584–597 (2019).

22. Pham, C. T. N. Neutrophil serine proteases: Specific regulators of inflammation. *Nat. Rev. Immunol.* **6**, 541–550 (2006).

23. Afonso, P. V. *et al.* LTB4 Is a Signal-Relay Molecule during Neutrophil Chemotaxis. *Dev. Cell* **22**, 1079–1091 (2012).

24. Zhang, D. & Frenette, P. S. Cross talk between neutrophils and the microbiota. *Blood* **133**, 2168–2177 (2019).

25. Marcos, V. *et al.* Free DNA in Cystic Fibrosis Airway Fluids Correlates with Airflow Obstruction. *Mediators Inflamm.* **2015**, 408935 (2015).

26. Gifford, A. M. & Chalmers, J. D. The role of neutrophils in cystic fibrosis. *Curr. Opin. Hematol.* **21**, (2014).

27. Khan, M. A., Ali, Z. S., Sweezey, N., Grasemann, H. & Palaniyar, N. Progression of Cystic Fibrosis Lung Disease from Childhood to Adulthood: Neutrophils, Neutrophil Extracellular Trap (NET) Formation, and NET Degradation. *Genes (Basel).* **10**, 183 (2019).

28. Makam, M. *et al.* Activation of critical , host-induced , metabolic and stress pathways marks neutrophil entry into cystic fibrosis lungs. **106**, (2009).

29. Tirouvanziam, R. *et al.* Profound functional and signaling changes in viable inflammatory neutrophils homing to cystic fibrosis airways. **105**, 4335–4339 (2008).

30. Bedi, P., Davidson, D. J., McHugh, B. J., Rossi, A. G. & Hill, A. T. Blood Neutrophils are Reprogrammed in Bronchiectasis. *Am. J. Respir. Crit. Care Med.* (2018). doi:10.1164/rccm.201712-2423OC

31. Mollinedo, F. Neutrophil Degranulation, Plasticity, and Cancer Metastasis. *Trends Immunol.* **40**, 228–242 (2019).

32. Silvestre-Roig, C., Hidalgo, A. & Soehnlein, O. Neutrophil heterogeneity: Implications for homeostasis and pathogenesis. *Blood* **127**, 2173–2181 (2016).

33. Korkmaz, B., Horwitz, M., Jenne, D. & Gauthier, F. Neutrophil elastase, proteinase 3, and cathepsin G as therapeutic targets in human diseases. *Pharmacol. Rev.* **62**, 726–759 (2010).

34. López-Otín, C. & Bond, J. S. Proteases: Multifunctional enzymes in life and disease. *J. Biol. Chem.* **283**, 30433–30437 (2008).

35. Ekici, O. D., Paetzel, M. & Dalbey, R. E. Unconventional serine proteases: variations on the catalytic Ser/His/Asp triad configuration. *Protein Sci.* **17**, 2023–2037 (2008).

36. Korkmaz, B., Moreau, T. & Gauthier, F. Neutrophil elastase, proteinase 3 and cathepsin G: Physicochemical properties, activity and physiopathological functions. *Biochimie* **90**, 227–242 (2008).

37. Korkmaz, B. *et al.* Therapeutic targeting of cathepsin C: from pathophysiology to treatment. *Pharmacol. Ther.* **190**, 202–236 (2018).

38. Owen, C. A., Campbell, M. A., Sannes, P. L., Boukedes, S. S. & Campbell, E. J. Cell surface-bound elastase and cathepsin G on human neutrophils: A novel, non-oxidative mechanism by which neutrophils focus and preserve catalytic activity of serine proteinases. *J. Cell Biol.* **131**, 775–789 (1995).

39. Campbell, E. J., Campbell, M. A. & Owen, C. A. Bioactive Proteinase 3 on the Cell Surface of Human Neutrophils: Quantification, Catalytic Activity, and Susceptibility to Inhibition. *J. Immunol.* **165**, 3366–3374 (2000).

40. Kasperkiewicz, P., Altman, Y., D'Angelo, M., Salvesen, G. S. & Drag, M. Toolbox of Fluorescent Probes for Parallel Imaging Reveals Uneven Location of Serine Proteases in Neutrophils. *J. Am. Chem. Soc.* **139**, 10115–10125 (2017).

41. Clancy, D. M. *et al.* Extracellular Neutrophil Proteases Are Efficient Regulators of IL-1, IL-33, and IL-36 Cytokine Activity but Poor Effectors of Microbial Killing. *Cell Rep.* **22**, 2937–2950 (2018).

42. McKelvey, M. C., Weldon, S., McAuley, D. F., Mall, M. A. & Taggart, C. C. Targeting proteases in cystic fibrosis lung disease paradigms, progress, and potential. *Am. J. Respir. Crit. Care Med.* **201**, 141–147 (2020).

43. Sly, P. D. *et al.* Risk Factors for Bronchiectasis in Children with Cystic Fibrosis. *N. Engl. J. Med.* **368**, 1963–1970 (2013).

44. Dittrich, A. S. *et al.* Elastase activity on sputum neutrophils correlates with severity of lung disease in cystic fibrosis. *Eur. Respir. J.* 1701910 (2018). doi:10.1183/13993003.01910-2017

45. Gehrig, S., Mall, M. A. & Schultz, C. Spatially resolved monitoring of neutrophil elastase activity with ratiometric fluorescent reporters. *Angew. Chemie - Int. Ed.* **51**, 6258–6261 (2012).

46. Zhou, Z. *et al.* The ENaC-overexpressing mouse as a model of cystic fibrosis lung disease. *J. Cyst. Fibros.* **10**, S172–S182 (2011).

47. Gehrig, S. *et al.* Lack of neutrophil elastase reduces inflammation, mucus hypersecretion, and emphysema, but not mucus obstruction, in mice with cystic fibrosislike lung disease. *Am. J. Respir. Crit. Care Med.* **189**, 1082–1092 (2014).

48. Polverino, E., Rosales-mayor, E., Dale, G. E. & Dembowsky, K. The Role of Neutrophil Elastase Inhibitors in Lung Diseases. *Chest* **152**, 249–262 (2017).

49. Wright, J. L., Cosio, M. & Churg, A. Animal models of chronic obstructive pulmonary disease. *Am. J. Physiol. Cell. Mol. Physiol.* **295**, L1–L15 (2008).

50. Pham, C. T. N. Neutrophil serine proteases fine-tune the inflammatory response. *Int. J. Biochem. Cell Biol.* **40**, 1317–1333 (2008).

51. Raptis, S. Z., Shapiro, S. D., Simmons, P. M., Cheng, A. M. & Pham, C. T. N. Serine protease cathepsin G regulates adhesion-dependent neutrophil effector functions by modulating integrin clustering. *Immunity* **22**, 679–691 (2005).

52. Vizovišek, M. *et al.* Protease Specificity: Towards In Vivo Imaging Applications and Biomarker Discovery. *Trends Biochem. Sci.* **43**, 829–844 (2018).

53. Clancy, D. M. *et al.* Extracellular Neutrophil Proteases Are Efficient Regulators of IL-1,

IL-33, and IL-36 Cytokine Activity but Poor Effectors of Microbial Killing. *Cell Rep.* **22**, 2937–2950 (2018).

54. Bauer, S. *et al.* Proteinase 3 and CD177 are expressed on the plasma membrane of the same subset of neutrophils. *J. Leukoc. Biol.* **81**, 458–464 (2007).

55. Jerke, U., Marino, S. F., Daumke, O. & Kettritz, R. Characterization of the CD177 interaction with the ANCA antigen proteinase 3. *Sci. Rep.* **7**, 43328 (2017).

56. Wagner, C. J., Schultz, C. & Mall, M. A. Neutrophil elastase and matrix metalloproteinase 12 in cystic fibrosis lung disease. *Mol. Cell. Pediatr.* **3**, 25 (2016).

57. Trojanek, J. B. *et al.* Airway mucus obstruction triggers macrophage activation and matrix metalloproteinase 12-dependent emphysema. *Am. J. Respir. Cell Mol. Biol.* **51**, 709–720 (2014).

58. Cobos-Correa, A., Trojanek, J. B., Diemer, S., Mall, M. A. & Schultz, C. Membrane-bound FRET probe visualizes MMP12 activity in pulmonary inflammation. *Nat. Chem. Biol.* **5**, 628–630 (2009).

59. Hu, H. Y. *et al.* In vivo imaging of mouse tumors by a lipidated cathepsin S substrate. *Angew. Chemie - Int. Ed.* **53**, 7669–7673 (2014).

60. Garland, M., Yim, J. J. & Bogyo, M. A Bright Future for Precision Medicine: Advances in Fluorescent Chemical Probe Design and Their Clinical Application. *Cell Chem. Biol.* **23**, 122–136 (2016).

61. Small, D. M. *et al.* Targeting of Cathepsin S Reduces Cystic Fibrosis-like Lung Disease. *Eur. Respir. J.* 1801523 (2019). doi:10.1183/13993003.01523-2018

62. Gaggar, A. *et al.* The role of matrix metalloproteinases in cystic fibrosis lung disease. *Eur. Respir. J.* **38**, 721–727 (2011).

63. Cobos-Correa, A., Trojanek, J. B., Diemer, S., Mall, M. a & Schultz, C. Membrane-bound FRET probe visualizes MMP12 activity in pulmonary inflammation. *Nat. Chem. Biol.* **5**, 628–30 (2009).

64. Kridel, S. J. *et al.* Substrate Hydrolysis by Matrix Metalloproteinase-9. *J. Biol. Chem.* **276**, 20572–20578 (2001).

65. Brinkmann, V. *et al.* Neutrophil Extracellular Traps Kill Bacteria. *Science (80-.).* **303**, 1532–1535 (2004).

66. Galluzzi, L. *et al.* Molecular mechanisms of cell death: recommendations of the Nomenclature Committee on Cell Death 2018. *Cell Death Differ.* **25**, 486–541 (2018).

67. Fuchs, T. A. *et al.* Novel cell death program leads to neutrophil extracellular traps. *J. Cell Biol.* **176**, 231–241 (2007).

68. Wang, Y. *et al.* Histone hypercitrullination mediates chromatin decondensation and neutrophil extracellular trap formation. *J. Cell Biol.* **184**, 205–213 (2009).

69. Porto, B. N. & Stein, R. T. Neutrophil Extracellular Traps in Pulmonary Diseases: Too Much of a Good Thing? *Front. Immunol.* **7**, 1–13 (2016).

70. Warnatsch, A., Ioannou, M., Wang, Q. & Papayannopoulos, V. Inflammation. Neutrophil extracellular traps license macrophages for cytokine production in atherosclerosis. *Science* **349**, 316–320 (2015).

71. Pierce, B. L. *et al.* Elevated biomarkers of inflammation are associated with reduced

survival among breast cancer patients. *J. Clin. Oncol.* **27**, 3437–3444 (2009).

72. Albrengues, J. *et al.* Neutrophil extracellular traps produced during inflammation awaken dormant cancer cells in mice. *Science* **361**, eaao4227 (2018).

73. Muñoz, L. E. *et al.* Neutrophil Extracellular Traps Initiate Gallstone Formation. *Immunity* **51**, 443-450.e4 (2019).

74. Mall, M. A., Mayer-hamblett, N. & Rowe, S. M. Cystic Fibrosis: Emergence of Highly Effective Targeted Therapeutics and Potential Clinical Implications. 1–64 (2019). doi:10.1164/rccm.201910-1943SO

75. Petretto, A. *et al.* Neutrophil extracellular traps (NET) induced by different stimuli: A comparative proteomic analysis. *PLoS One* **14**, e0218946–e0218946 (2019).

76. Chapman, E. A. *et al.* Caught in a Trap? Proteomic Analysis of Neutrophil Extracellular Traps in Rheumatoid Arthritis and Systemic Lupus Erythematosus . *Frontiers in Immunology* **10**, 423 (2019).

77. Genschmer, K. R. *et al.* Activated PMN Exosomes : Pathogenic Entities Causing Matrix Destruction and Disease in the Lung Article Activated PMN Exosomes : Pathogenic Entities Causing Matrix Destruction and Disease in the Lung. *Cell* **176**, 113-126.e15 (2019).

78. Valadi, H. *et al.* Exosome-mediated transfer of mRNAs and microRNAs is a novel mechanism of genetic exchange between cells. *Nat. Cell Biol.* **9**, 654–659 (2007).

79. Maas, S. L. N., Breakefield, X. O. & Weaver, A. M. Extracellular Vesicles: Unique Intercellular Delivery Vehicles. *Trends Cell Biol.* **27**, 172–188 (2017).

80. van den Boorn, J. G., Daßler, J., Coch, C., Schlee, M. & Hartmann, G. Exosomes as nucleic acid nanocarriers. *Adv. Drug Deliv. Rev.* **65**, 331–335 (2013).

81. Andreu, Z. & Yáñez-Mó, M. Tetraspanins in Extracellular Vesicle Formation and Function . *Frontiers in Immunology* **5**, 442 (2014).

82. Vargas, A., Roux-Dalvai, F., Droit, A. & Lavoie, J.-P. Neutrophil-Derived Exosomes: A New Mechanism Contributing to Airway Smooth Muscle Remodeling. *Am. J. Respir. Cell Mol. Biol.* **55**, 450–461 (2016).

83. Szul, T. *et al.* Toll-Like Receptor 4 Engagement Mediates Prolyl Endopeptidase Release from Airway Epithelia via Exosomes. *Am. J. Respir. Cell Mol. Biol.* **54**, 359–369 (2016).

84. Parolini, I. *et al.* Microenvironmental pH is a key factor for exosome traffic in tumor cells. *J. Biol. Chem.* **284**, 34211–34222 (2009).

85. Wielpütz, M. O. *et al.* In vivo monitoring of cystic fibrosis-like lung disease in mice by volumetric computed tomography. *Eur. Respir. J.* **38**, 1060–1070 (2011).

86. Craven, T. H. *et al.* Super-silent FRET Sensor Enables Live Cell Imaging and Flow Cytometric Stratification of Intracellular Serine Protease Activity in Neutrophils. *Sci. Rep.* **8**, 13490 (2018).

87. Korkmaz, B. *et al.* Measuring elastase, proteinase 3 and cathepsin G activities at the surface of human neutrophils with fluorescence resonance energy transfer substrates. *Nat Protoc* **3**, 991–1000 (2008).

88. Castillo, M. J., Nakajima, K., Zimmerman, M. & Powers, J. C. Sensitive substrates for human leukocyte and porcine pancreatic elastase: A study of the merits of various

chromophoric and fluorogenic leaving groups in assays for serine proteases. *Anal. Biochem.* **99**, 53–64 (1979).

89. Hu, H.-Y. *et al.* FRET-based and other fluorescent proteinase probes. *Biotechnol. J.* **9**, 266–281 (2014).

90. Blum, G., von Degenfeld, G., Merchant, M. J., Blau, H. M. & Bogyo, M. Noninvasive optical imaging of cysteine protease activity using fluorescently quenched activity-based probes. *Nat. Chem. Biol.* **3**, 668–677 (2007).

91. Blum, G. *et al.* Dynamic imaging of protease activity with fluorescently quenched activity-based probes. *Nat. Chem. Biol.* **1**, 203–209 (2005).

92. Vasiljeva, O. *et al.* Tumor Cell–Derived and Macrophage-Derived Cathepsin B Promotes Progression and Lung Metastasis of Mammary Cancer. *Cancer Res.* **66**, 5242 LP – 5250 (2006).

93. Joyce, J. A. *et al.* Cathepsin cysteine proteases are effectors of invasive growth and angiogenesis during multistage tumorigenesis. *Cancer Cell* **5**, 443–453 (2004).

94. Chuang, C.-H. *et al.* In Vivo Positron Emission Tomography Imaging of Protease Activity by Generation of a Hydrophobic Product from a Noninhibitory Protease Substrate. *Clin. Cancer Res.* **18**, 238 LP – 247 (2012).

95. Jugniot, N., Voisin, P., Bentaher, A. & Mellet, P. Neutrophil Elastase Activity Imaging: Recent Approaches in the Design and Applications of Activity-Based Probes and Substrate-Based Probes. *Contrast Media & Mol. Imaging* **2019**, 7417192 (2019).

96. Middleton, P. G. *et al.* Elexacaftor–Tezacaftor–Ivacaftor for Cystic Fibrosis with a Single Phe508del Allele. *N. Engl. J. Med.* **381**, 1809–1819 (2019).

97. Heijerman, H. G. M. *et al.* Efficacy and safety of the elexacaftor plus tezacaftor plus ivacaftor combination regimen in people with cystic fibrosis homozygous for the F508del mutation: a double-blind, randomised, phase 3 trial. *Lancet* **394**, 1940–1948 (2019).

98. Fermont, J. M. *et al.* Biomarkers and clinical outcomes in COPD : a systematic review and meta-analysis. 439–446 (2019). doi:10.1136/thoraxjnl-2018-211855

99. Anderson, G. P. Advances in understanding COPD [version 1 ; referees : 3 approved] Referee Status : **5**, (2016).

100. Lange, P. *et al.* Lung-Function Trajectories Leading to Chronic Obstructive Pulmonary Disease. *N. Engl. J. Med.* **373**, 111–122 (2015).

101. Mannino, D. M. Biomarkers in COPD : the search continues ! 872–874 (2015). doi:10.1183/09031936.00236314

102. Hilgenfeld, R. From SARS to MERS: crystallographic studies on coronaviral proteases enable antiviral drug design. *FEBS J.* **281**, 4085–4096 (2014).

103. Zhang, L. *et al.* Crystal structure of SARS-CoV-2 main protease provides a basis for design of improved α-ketoamide inhibitors. *Science (80-.).* eabb3405 (2020). doi:10.1126/science.abb3405

104. Cascella M, Rajnik M, C. A. Features, Evaluation and Treatment Coronavirus (COVID-19) [Updated 2020 Mar 20]. (2020). Available at: https://www.ncbi.nlm.nih.gov/books/NBK554776/.

105. Cao, X. COVID-19: immunopathology and its implications for therapy. *Nat. Rev.*

Immunol. **2019**, (2019).

106. Shi, Y. *et al.* COVID-19 infection: the perspectives on immune responses. *Cell Death Differ.* (2020). doi:10.1038/s41418-020-0530-3

107. Genentech Initiates Phase III Clinical Trial Of Actemra In Hospitalized Patients With Severe COVID-19 Pneumonia. Available at: https://www.gene.com/media/press-releases/14841/2020-03-18/genentech-initiates-phase-iii-clinical-t.

108. Attucci, S. *et al.* Measurement of free and membrane-bound cathepsin G in human neutrophils using new sensitive fluorogenic substrates. *Biochem. J.* **366**, 965–70 (2002).

109. Korkmaz, B. *et al.* Discriminating between the activities of human cathepsin G and chymase using fluorogenic substrates. *FEBS J.* **278**, 2635–2646 (2011).

110. Korkmaz, B. *et al.* Discriminating between the activities of human neutrophil elastase and proteinase 3 using serpin-derived fluorogenic substrates. *J. Biol. Chem.* **277**, 39074–39081 (2002).

111. Fahy, J. V, Liu, J., Boushey, H. A. & Francisco, S. Respiratory pathophysiologic responses Prominent neutrophilic inflammation in sputum from subjects with asthma exacerbation. 843–852

112. Margaroli, C. *et al.* Elastase Exocytosis by Airway Neutrophils Associates with Early Lung Damage in Cystic Fibrosis Children. *Am. J. Respir. Crit. Care Med.* (2018). doi:10.1164/rccm.201803-0442OC

113. Twigg, M. S. *et al.* The Role of Serine Proteases and Antiproteases in the Cystic Fibrosis Lung. *Mediators Inflamm.* **2015**, 1–10 (2015).

114. Weldon, S. *et al.* Decreased levels of secretory leucoprotease inhibitor in the Pseudomonas-infected cystic fibrosis lung are due to neutrophil elastase degradation. *J. Immunol.* **183**, 8148–8156 (2009).

115. Van Gassen, S. *et al.* FlowSOM: Using self-organizing maps for visualization and interpretation of cytometry data. *Cytom. Part A* **87**, 636–645 (2015).

116. Genschmer, K. R. *et al.* Activated PMN Exosomes: Pathogenic Entities Causing Matrix Destruction and Disease in the Lung. *Cell* **176**, 113-126.e15 (2019).

117. Osteikoetxea, X. *et al.* Differential detergent sensitivity of extracellular vesicle subpopulations. *Org. Biomol. Chem.* **13**, 9775–9782 (2015).

118. Lozano-Andrés, E. *et al.* Tetraspanin-decorated extracellular vesicle-mimetics as a novel adaptable reference material. *J. Extracell. Vesicles* **8**, (2019).

119. Gieseler, F., Ungefroren, H., Settmacher, U., Hollenberg, M. D. & Kaufmann, R. Proteinase-activated receptors (PARs) - Focus on receptor-receptor- interactions and their physiological and pathophysiological impact. *Cell Commun. Signal.* **11**, 1 (2013).

120. Lukinavičius, G. *et al.* SiR-Hoechst is a far-red DNA stain for live-cell nanoscopy. *Nat. Commun.* **6**, 1–7 (2015).

121. Chen, M.-S., Lin, W.-C., Yeh, H.-T., Hu, C.-L. & Sheu, S.-M. Propofol specifically reduces PMA-induced neutrophil extracellular trap formation through inhibition of p-ERK and HOCl. *Life Sci.* **221**, 178–186 (2019).

122. Yang, H. *et al.* New insights into neutrophil extracellular traps: Mechanisms of formation and role in inflammation. *Front. Immunol.* **7**, 1–8 (2016).

123. Dubois, A. V. *et al.* Influence of DNA on the activities and inhibition of neutrophil serine proteases in cystic fibrosis sputum. *Am. J. Respir. Cell Mol. Biol.* **47**, 80–86 (2012).

124. Gehrig, S. *et al. Lack of neutrophil elastase reduces inflammation, mucus hypersecretion, and emphysema, but not mucus obstruction, in mice with cystic fibrosislike lung disease*. *American Journal of Respiratory and Critical Care Medicine* **189**, (2014).

125. Guyot, N. *et al.* Unopposed cathepsin G, neutrophil elastase, and proteinase 3 cause severe lung damage and emphysema. *Am. J. Pathol.* **184**, 2197–2210 (2014).

126. Steinwede, K. *et al.* Cathepsin G and Neutrophil Elastase Contribute to Lung-Protective Immunity against Mycobacterial Infections in Mice. *J. Immunol.* **188**, 4476 LP – 4487 (2012).

127. Levy, H. & Feinstein, G. The digestion of the oxidized B chain of insulin by human neutrophile proteases: Elastase and chymotrypsin-like protease. *Biochim. Biophys. Acta - Enzymol.* **567**, 35–42 (1979).

128. Yu, X. *et al.* Neutrophil Adhesion Is a Prerequisite for Antibody-Mediated Proteolytic Tissue Damage in Experimental Models of Epidermolysis Bullosa Acquisita. *J. Invest. Dermatol.* **138**, 1990–1998 (2018).

129. Saeys, Y., Gassen, S. Van & Lambrecht, B. N. Computational flow cytometry : helping to make sense of high-dimensional immunology data. (2016). doi:10.1038/nri.2016.56

130. Tibbitt, C. A. *et al.* Single-Cell RNA Sequencing of the T Helper Cell Response to House Dust Mites Defines a Distinct Gene Expression Signature in Airway Th2 Cells Resource Single-Cell RNA Sequencing of the T Helper Cell Response to House Dust Mites Defines a Distinct Gene Exp. 169–184 (2019). doi:10.1016/j.immuni.2019.05.014

131. Barcenilla, H., Åkerman, L., Pihl, M. & Ludvigsson, J. Mass Cytometry Identifies Distinct Subsets of Regulatory T Cells and Natural Killer Cells Associated With High Risk for Type 1 Diabetes. **10**, (2019).

132. Kropf, P. *et al.* Arginase activity mediates reversible T cell hyporesponsiveness in human pregnancy. *Eur. J. Immunol.* **37**, 935–945 (2007).

133. de Oliveira, S., Rosowski, E. E. & Huttenlocher, A. Neutrophil migration in infection and wound repair: going forward in reverse. *Nat. Rev. Immunol.* **16**, 378–391 (2016).

134. Wang, Y. & Jönsson, F. Expression, Role, and Regulation of Neutrophil Fcγ Receptors . *Frontiers in Immunology* **10**, 1958 (2019).

135. Branzk, N. *et al.* Neutrophils sense microbe size and selectively release neutrophil extracellular traps in response to large pathogens. *Nat. Immunol.* **15**, 1017–1025 (2014).

136. Pohl, K. *et al.* A neutrophil intrinsic impairment affecting Rab27a and degranulation in cystic fibrosis is corrected by CFTR potentiator therapy. *Blood* **124**, 999–1009 (2014).

137. Li, P., Kaslan, M., Lee, S. H., Yao, J. & Gao, Z. Progress in Exosome Isolation Techniques. *Theranostics* **7**, 789–804 (2017).

138. Korkmaz, B. *et al.* Design and use of highly specific substrates of neutrophil elastase and proteinase 3. *Am. J. Respir. Cell Mol. Biol.* **30**, 801–807 (2004).

139. Young, R. L. *et al.* Neutrophil extracellular trap (NET)-mediated killing of pseudomonas aeruginosa: Evidence of acquired resistance within the CF airway, independent of CFTR. *PLoS One* **6**, (2011).

140. Higuchi, S., Suga, M., Dannenberg, A. M. & Schofield, B. H. Histochemical demonstration of enzyme activities in plastic and paraffin embedded tissue sections. *Biotech. Histochem.* **54**, 5–12 (1979).

141. Stein, F. *et al.* FluoQ - a tool for rapid analysis of multiparameter fluorescence imaging data applied to oscillatory events Supplementary Figures and Tables. *ACS Chem. Biol.* **14**, 1–23 (2013).

Appendix

Structures and analytical data of synthetized compounds

High resolution mass spectra (ESI negative mode) found for the compounds presented throughout the thesis:

- **sSAM**:
  $[M+1]^+$ exp. 1902.74, found 1901.77
- **mSAM:**
  $[M+1]^+$ exp. 2268.11, found 2268.08
- **Hoechst-azide:**
  $[M+1]^+$ exp. 581.29, found 582.29
- **A-NE:**
  $[M+1]^+$ exp. 2177.02, found 2178.02
- **A-CG:**
  $[M+1]^+$ exp. 1997.02, not found, $[M+2]^{2+}$ exp. 998.51, found 1010.91
- **H-NE:**
  $[M+1]^+$ exp. 2758.30, found 2757.06, $[M+2]^{2+}$ 1379.15, found 1380.15
- **H-CG:**
- $[M+1]^+$ exp. 2579.11, not found, $[M+2]^{2+}$ 1289.55, found 1290.56

sSAM

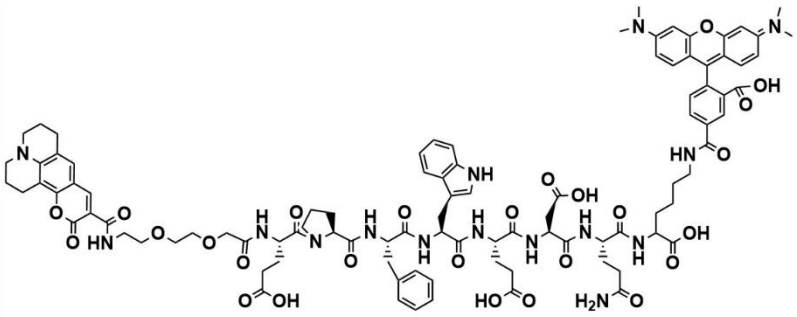

Chemical Formula: $C_{97}H_{112}N_{15}O_{26}$
Exact Mass: 1902,79
Molecular Weight: 1904,04

Semipreparative HPLC:

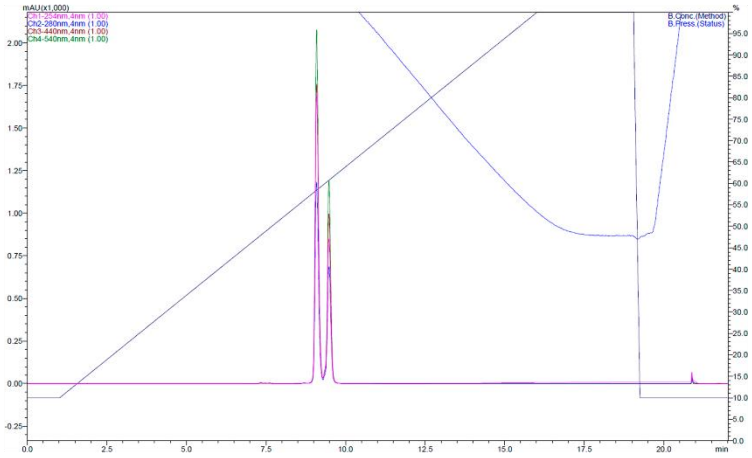

High res. mass spectrometry:

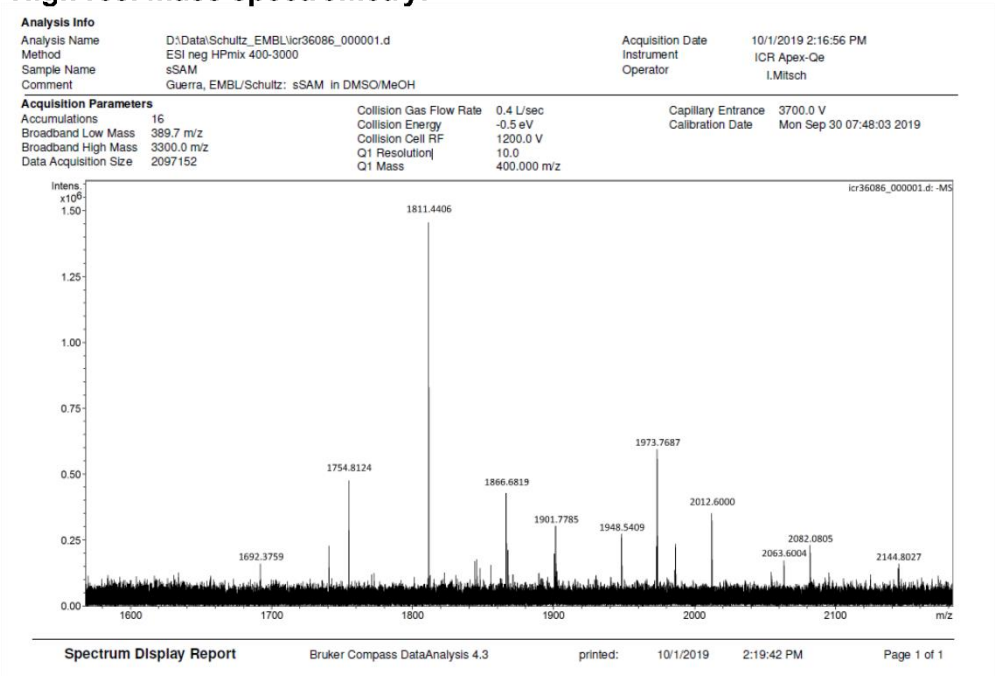

mSAM

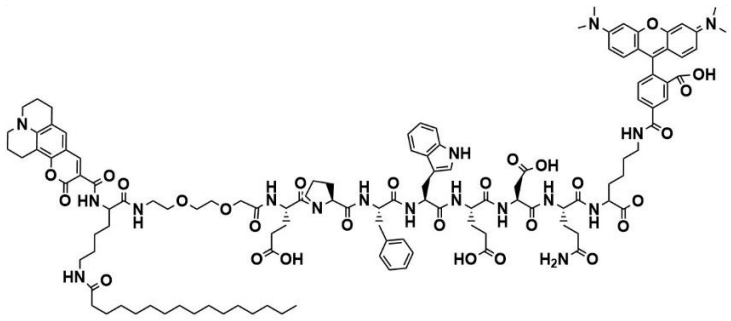

Chemical Formula: $C_{119}H_{153}N_{17}O_{28}^-$
Exact Mass: 2268,11
Molecular Weight: 2269,62

Semipreparative HPLC:

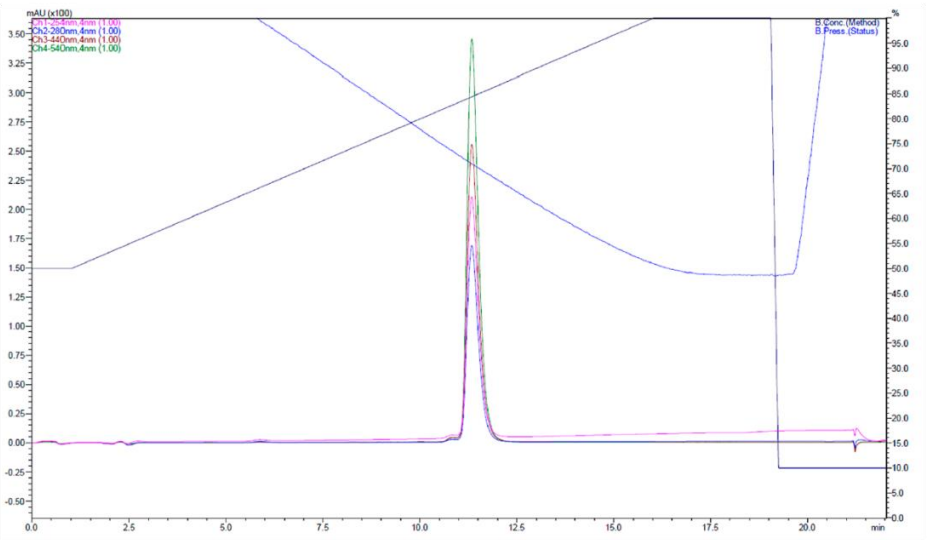

High res. mass spectrometry:

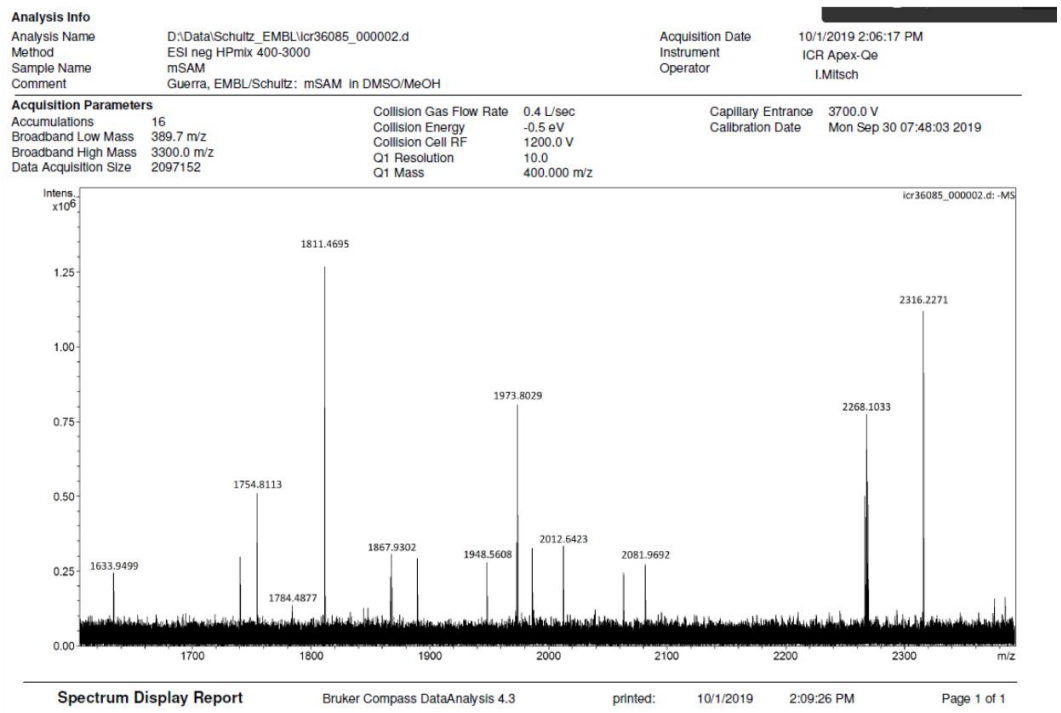

Analysis Info

Analysis Name	D:\Data\Schultz_EMBL\icr36085_000002.d	Acquisition Date	10/1/2019 2:06:17 PM
Method	ESI neg HPmix 400-3000	Instrument	ICR Apex-Qe
Sample Name	mSAM	Operator	I.Mitsch
Comment	Guerra, EMBL/Schultz: mSAM in DMSO/MeOH		

Acquisition Parameters

Accumulations	16	Collision Gas Flow Rate	0.4 L/sec	Capillary Entrance	3700.0 V
Broadband Low Mass	389.7 m/z	Collision Energy	-0.5 eV	Calibration Date	Mon Sep 30 07:48:03 2019
Broadband High Mass	3300.0 m/z	Collision Cell RF	1200.0 V		
Data Acquisition Size	2097152	Q1 Resolution	10.0		
		Q1 Mass	400.000 m/z		

Spectrum Display Report | Bruker Compass DataAnalysis 4.3 | printed: 10/1/2019 2:09:26 PM | Page 1 of 1

hoechst-azide

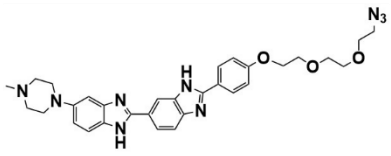

Chemical Formula: $C_{31}H_{35}N_9O_3$
Exact Mass: 581,29
Molecular Weight: 581,68

Semipreparative HPLC:

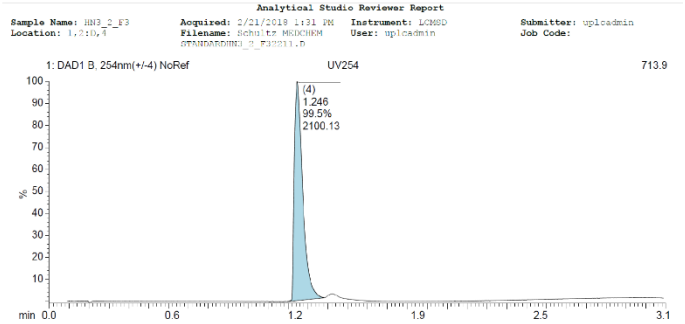

High res. mass spectrometry:

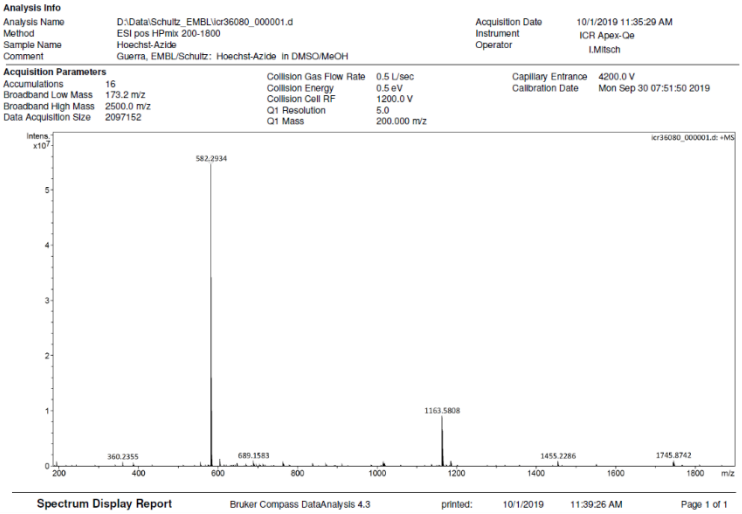

NMR:

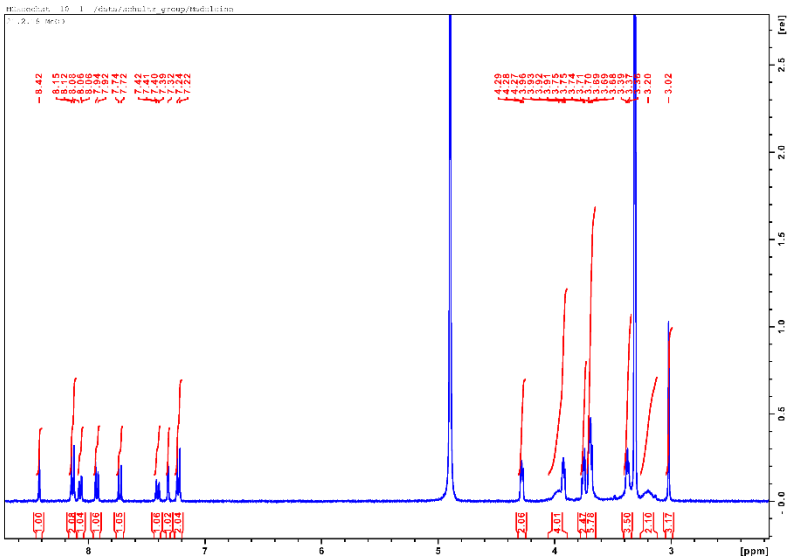

A-NE

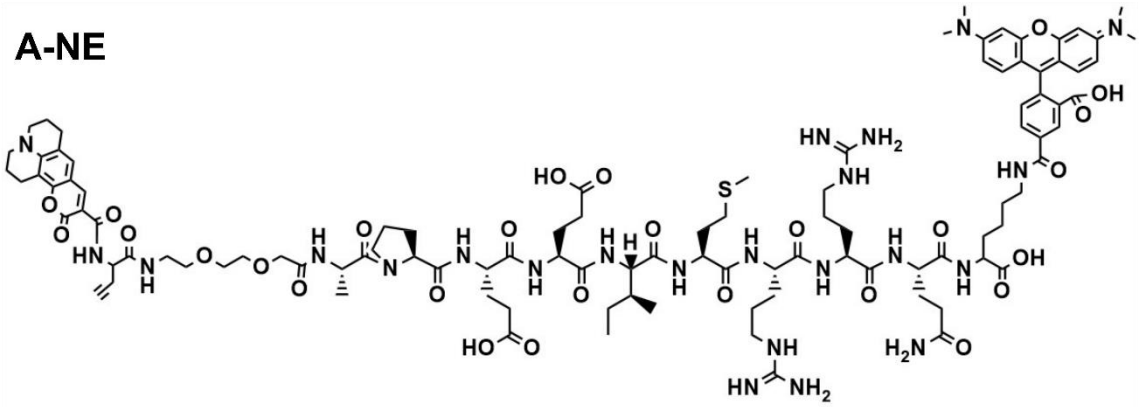

Chemical Formula: $C_{104}H_{142}N_{23}O_{27}S$
Exact Mass: 2177,02
Molecular Weight: 2178,47

High res. mass spectrometry:

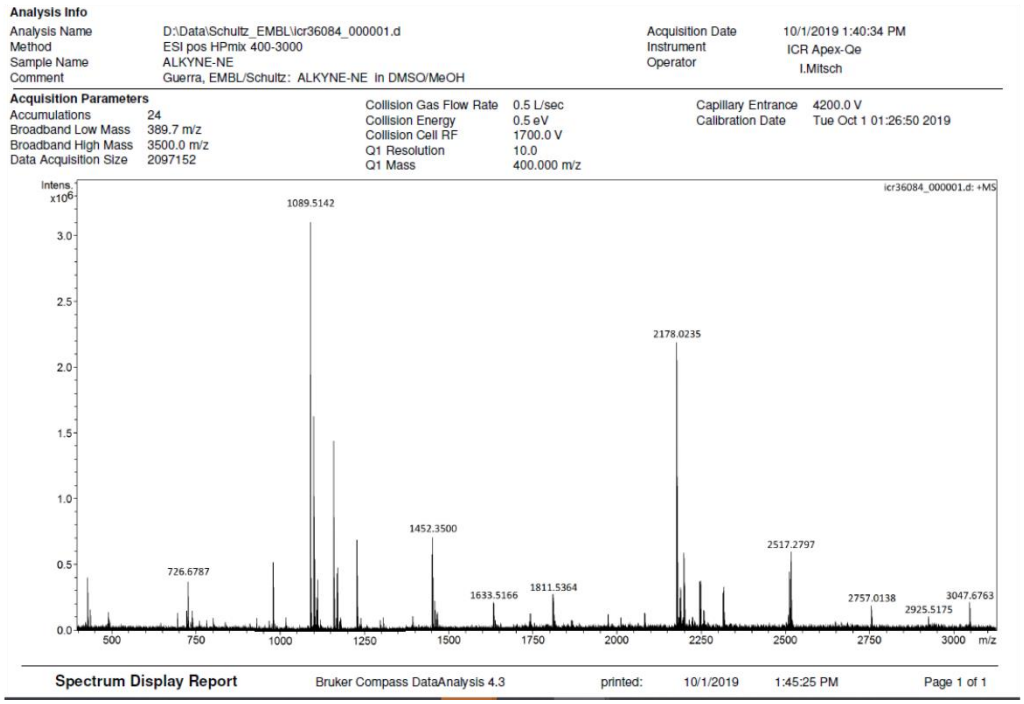

A-CG

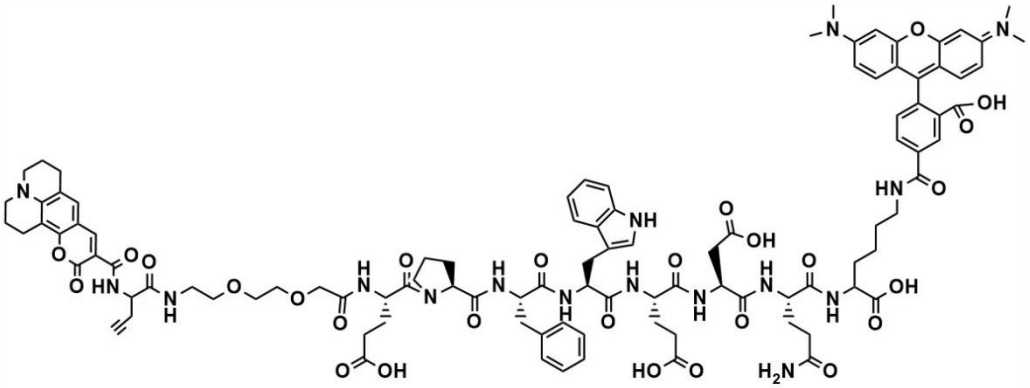

Chemical Formula: $C_{102}H_{117}N_{16}O_{27}$
Exact Mass: 1997,83
Molecular Weight: 1999,14

High res. mass spectrometry:

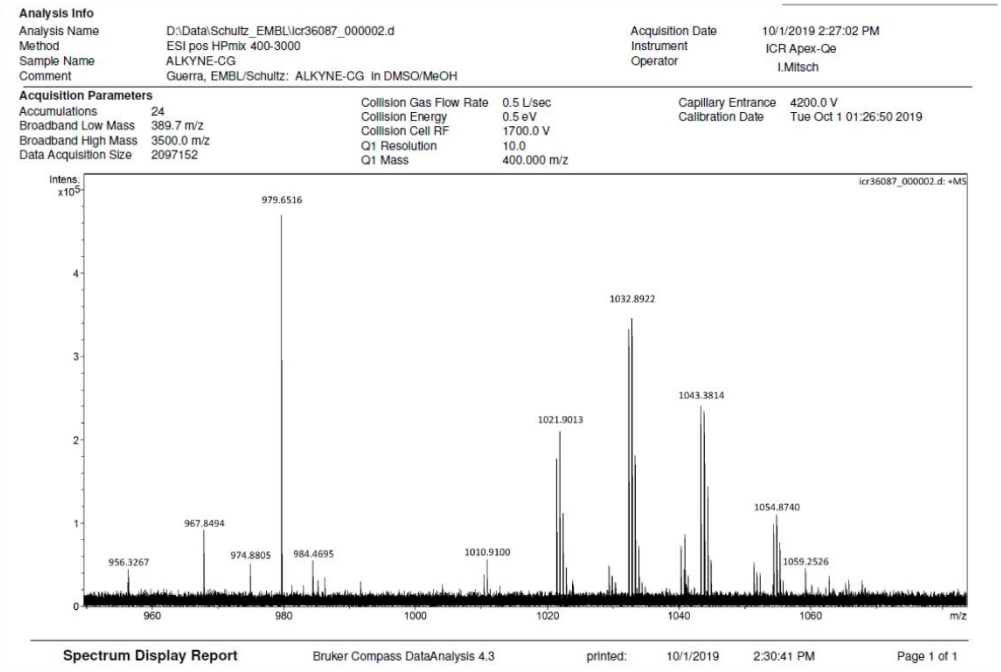

H-NE

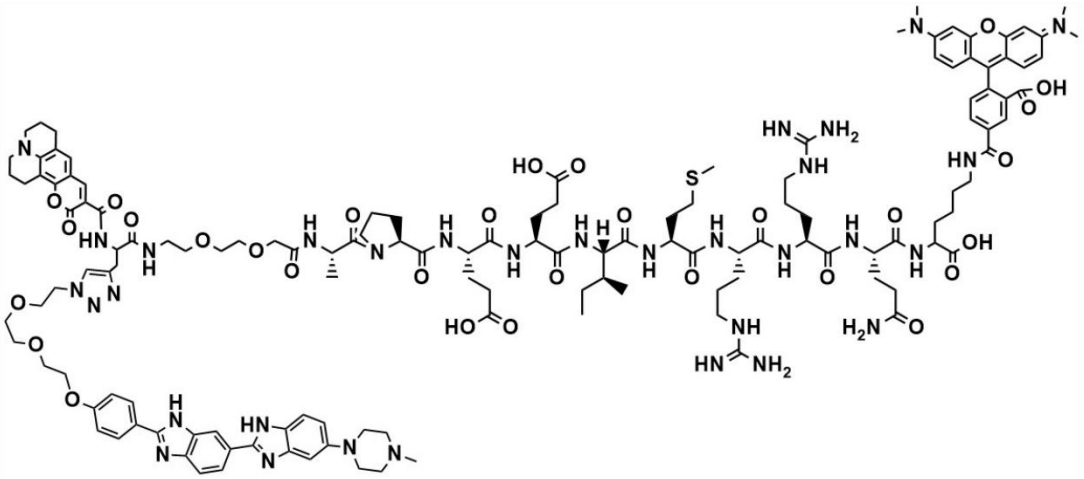

Chemical Formula: $C_{135}H_{177}N_{32}O_{30}S$
Exact Mass: 2758,30
Molecular Weight: 2760,16

Semipreparative HPLC:

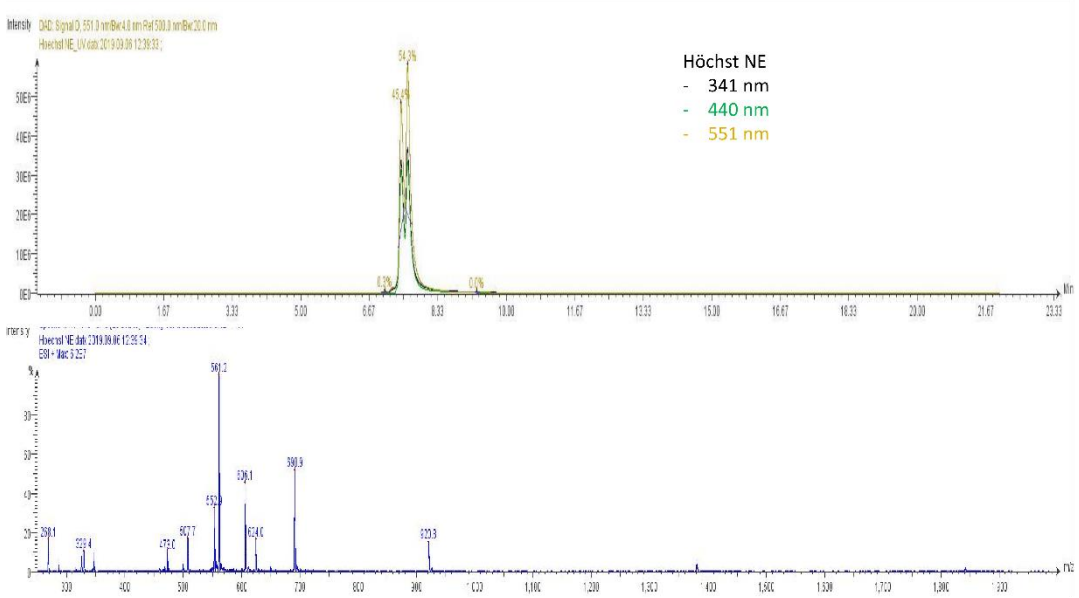

High res. mass spectrometry:

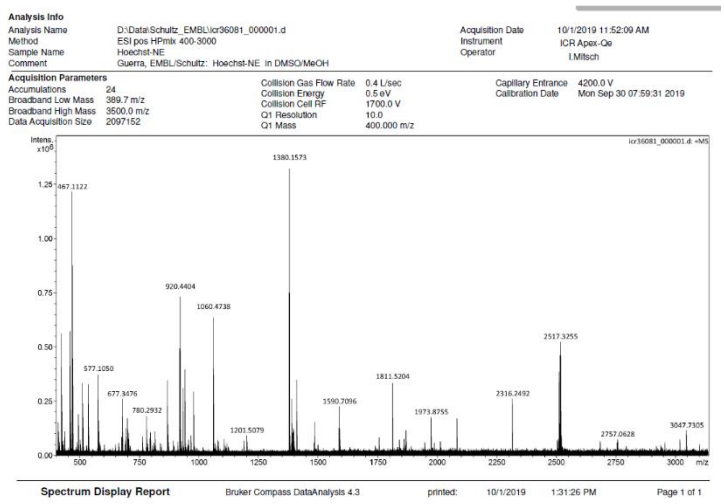

H-CG

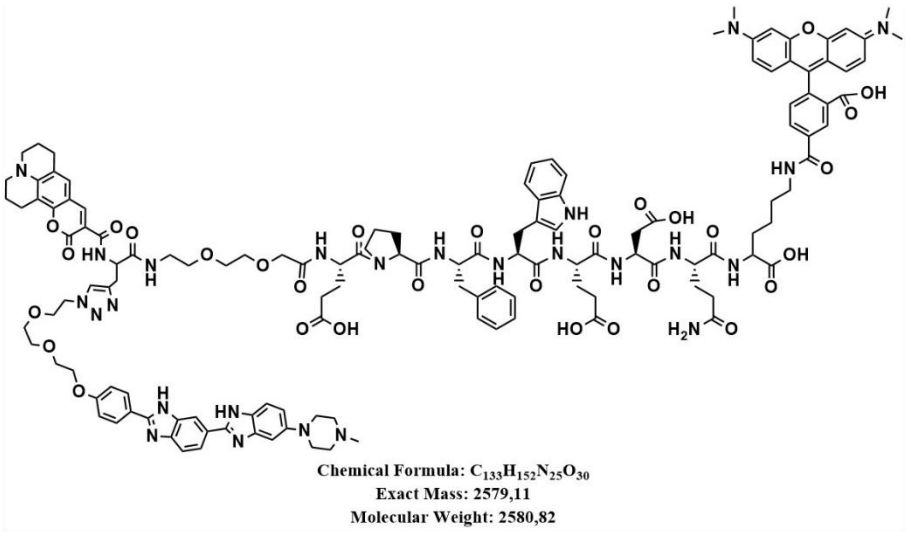

Chemical Formula: $C_{133}H_{152}N_{25}O_{30}$
Exact Mass: 2579,11
Molecular Weight: 2580,82

Semipreparative HPLC:

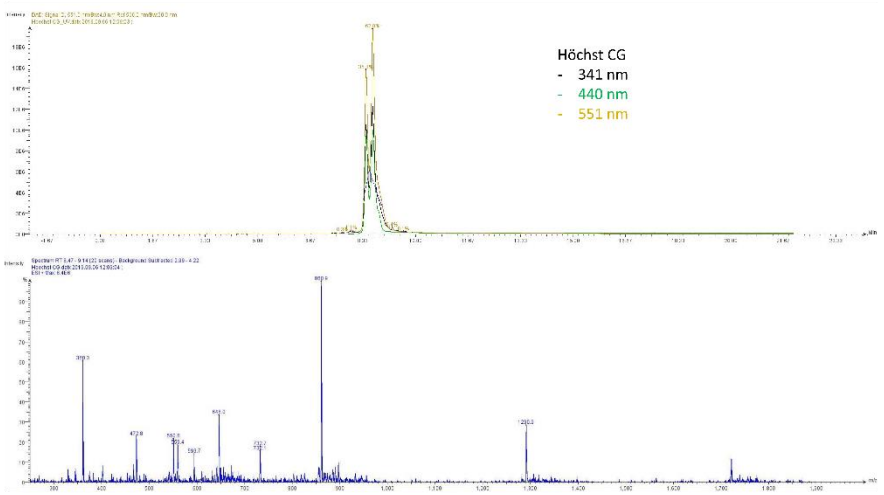

High res. mass spectrometry:

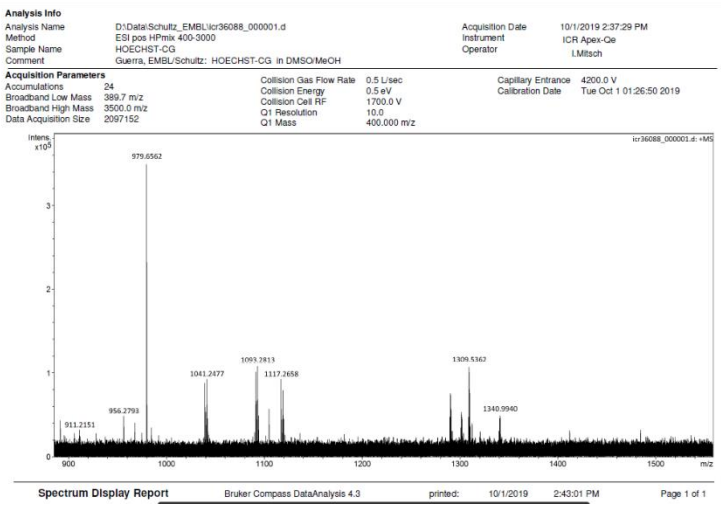

mSAM cleavage site demonstration

mSAM [1mM] was dissolved in 0.1 M Tris-HCl, pH 7.5 and 200 nM human cathepsin G were added and incubated for 1 h at room temperature. The fragments originated by the enzymatic cleavage were analyzed by HPLC-MS. HPLC chromatograms of CG treated (**a** and **b**) and untreated (**c** and **d**) mSAM. **a**) Peak 1 in showed the characteristic TAMRA absorption and the mass corresponding to the acceptor fragment shown in **e**. The Peak 2 and 1' in **a** and **c** corresponded to the uncleaved reporter (coumarin 343 and TAMRA absorption and the mass shown in **g**. Due to the impossibility to separate such a hydrophobic compound in only one HPLC run, peak 3, corresponding to the donor fragment possessing exclusively coumarin343 absorption shown in **b** and **d** and mass shown in **f**, was eluted in the subsequent HPLC run. Figure from Guerra M. et al., DOI: 10.1021/acscentsci.8b00933

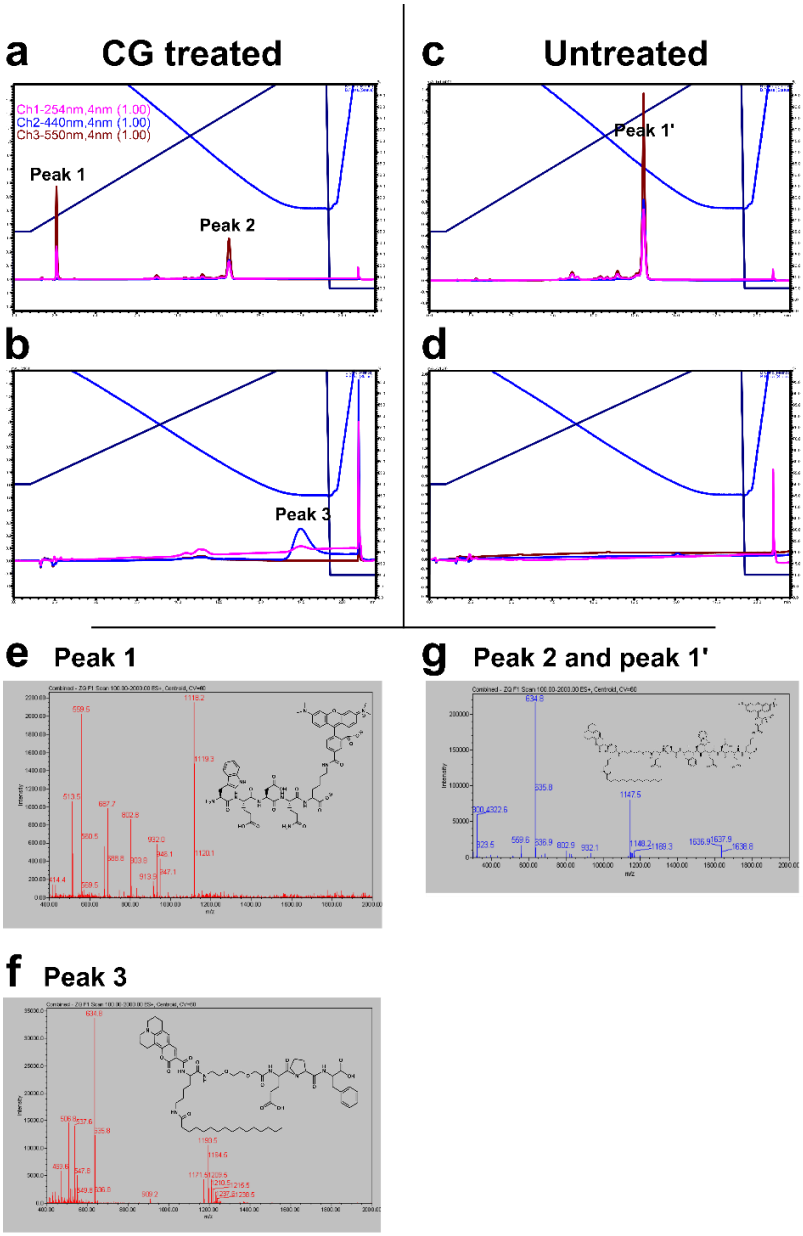

Patients demographics

The first data table refers to data shown in **Figure 6** and **7**. The second table refers to the data shown in **Figure 9** and the last table refers to **Figures 10**, **11** and **16**.

CF		**COPD**		**Healthy**	
Number of subjects	34	Number of subjects	12	Number of subjects	11
Age (years) Median	28	Age (years) Median	68	Age (years) Median	27
Range	16-73	Range	50-83	Range	23-49
Males	23	Males	5	Males	7
Females	11	Females	7	Females	4
CFTR genotype					
F508del/F508del	18				
F508del/other	11				
other/other	5				

CF		**Healthy**	
Number of subjects	12	Number of subjects	5
Age (years) Median	30	Age (years) Median	36
Range	22-58	Range	27-49
Males	missing	Males	missing
Females	missing	Females	missing
CFTR genotype			
F508del/F508del	6		
F508del/other	1		
other/other	5		

CF		**COPD**	
Number of subjects	26	Number of subjects	13
Age (years) Median	29	Age (years) Median	66
Range	4_73	Range	50-75
Males	18	Males	8
Females	8	Females	5
CFTR genotype			
F508del/F508del	3		
F508del/other	19		
other/other	4		

Publications

- **Matteo Guerra**, Dario Frey, Matthias Hagner, Susanne Dittrich, Michelle Paulsen, Marcus A Mall**, Carsten Schultz** (2019). **Cathepsin G Activity as a New Marker for Detecting Airway Inflammation by Microscopy and Flow Cytometry**, *ACS Central Science*, DOI: 10.1021/acscentsci.8b00933

- Matthias Hagner*, Dario Frey*, **Matteo Guerra***, Susanne Dittrich, Victoria S Halls, Sabine Wege, Felix JF Herth, Carsten Schultz**, Marcus A Mall** (2020). **New method for rapid and dynamic quantification of elastase activity on sputum neutrophils from patients with cystic fibrosis using flow cytometry**, *European Respiratory Journal*, DOI: 10.1183/13993003.02355-2019

- Sara Sartini, Elisabetta Levati, Martina Maccesi, **Matteo Guerra**, Gilberto Spadoni, Stéphane Bach, Monica Benincasa, Marco Scocchi, Simone Ottonello, Silvia Rivara, Barbara Montanini (2019). **New antimicrobials targeting bacterial RNA polymerase holoenzyme assembly identified with an *in vivo* BRET-based discovery platform**, *ACS Chemical Biology*, DOI: 10.1021/acschembio.9b00178

Under revision and resubmission:

- Matthias Hagner*, Melanie Albrecht*, **Matteo Guerra**, Peter Braubach, Olga Halle, Zhe Zhou-Suckow, Simone Butz, Danny Jonigk, Gesine Hansen, Carsten Schultz, Anna-Maria Dittrich**, Marcus A. Mall** (2020). **IL-17A from innate and adaptive lymphocytes contributes to inflammation and damage in cystic fibrosis lung disease**, *European Respiratory Journal*

In preparation:

- **Matteo Guerra***, Victoria Halls*, Jolanthe Schatterney, Matthias Hagner, Marcus Mall**, Carsten Schultz**, **DNA-bound reporters light up protease activity on extracellular DNA and neutrophil extracellular traps**

*** contributed equally as first authors**

**** contributed equally as senior authors**

Acknowledgments

First, I would like to thank my two supervisors, Prof. Carsten Schultz and Prof. Marcus Mall for giving me the opportunity to join their labs, for the knowledge they shared, for their patience and the fruitful scientific discussion. Also, they gave me a unique chance: to let me pursue my ideas and make my mistakes, I will be always grateful for that. I really hope that we can keep collaborating and make exciting science together also after the end of my PhD.

Also, I would like to thank my TAC members: Britta Brügger, Edward Lemke and Yannick Schwab for their interest in my work, their helpful suggestions and for being always available and friendly.

Thanks to Jolanthe Schatterney, Susanne Dittrich, Victoria Halls and Michelle Paulsen for training, their help to perform experiments and for sample collection. Many thanks to all lab members at EMBL and at the TLRC at Heidelberg University for the nice working environment, for their assistance and discussion of scientific questions.

A special thanks to Dario Frey and Matthias Hagner, our scientific discussion and the time we spent together were worth way more than a couple of publications.

Thank you Matilde, for making this journey lighter and funnier.

Grazie mamma, grazie papà.